NANOTHAILAND 2023

The 8th Thailand International Nanotechnology Conference

"Nanotechnology for Sustainable World"

e-Proceeding

November 29- December 1, 2023
Dusit Thani Pattaya Hotel,
Chon Buri,Thailand

Sponsor

e-Proceeding

NANOTHAILAND2023

The 8th Thailand International Nanotechnology Conference

November 29 – December 1, 2023

Dusit Thani Pattaya, Chonburi,Thailand

CONTENT

Welcome Message

From the Nanotechnology Association of Thailand and National Nanotechnology Center (NANOTEC)

Dr. Wannee Chinsirikul
Executive Director of the National Nanotechnology Center (NANOTEC) and President of the Nanotechnology Association of Thailand

On behalf of the Nanotechnology Association of Thailand, it is my great pleasure and privilege to extend a warm invitation to you all for participating the 8th Thailand International Nanotechnology Conference (NanoThailand 2023), which will be held during 29 November – 1 December 2023 at Pattaya, Chonburi, Thailand. I would like to take this opportunity to express my sincere appreciation to Vidyasirimedhi Institute of Science and Technology (VISTEC), National Nanotechnology Center (NANOTEC) and the Nanotechnology Association of Thailand to organize this conference.

The theme of the conference is "Nanotechnology for Sustainable World". The objectives are to apply nanoscience and nanotechnology for a better life and well-being to create a platform for knowledge exchange to further advance technological areas, and to exhibit the latest innovations to the industries. At present, we are collaborating in areas such as e-science, renewable energy and the development of novel drugs to combat a range of infectious diseases. Therefore, Science, Technology, Innovation and technology know-how cooperation among peers are very important. NanoThailand 2023 will provide a platform for experienced researchers in nanotechnology and practitioners from both academics, as well as industry to meet and share cutting-edge development in the field. In order to meet the objectives of the conference, the world renowned speakers, and researchers are invited to present the advancement of nanoscience and to update trend of the World's nanotechnology of their expertise.

I would like to welcome all participants, and to our overseas friends, please enjoy the breath and depth of Science and Technology at the upcoming NanoThailand 2023 (29 November – 1 December 2023) in the vibrant east coastal city of Thailand where you could take times to also absorb many attractive sites there is to offer in Pattaya.

Welcome Message

Form Vidyasirimedhi Institute of Science and Technology (VISTEC)

Professor Dr. Pimchai Chaiyen
President of Vidyasirimedhi Institute of Science and Technology (VISTEC)

On behalf of Vidyasirimedhi Institute of Science and Technology (VISTEC), it is my great pleasure to welcome you all to the 8th Thailand International Nanotechnology Conference (NanoThailand 2023), being held between 29 November – 1 December 2023 at Dusit Thani Hotel, Pattaya, Thailand. VISTEC is proud to be a co-host of this conference.

The conference's theme is "Nanotechnology for Sustainable World" and its objectives are to apply nanotechnology in various fields to contribute to sustainable development. The conference will create a platform for technological knowledge exchange, and to share the latest progress in research and innovations towards a sustainable world. We are expecting around 350 participants from more than 20 countries to attend NanoThailand 2023. The conference features 13 sessions with 2 plenary lectures, 97 keynote and invited talks, 97 oral presentations and 82 posters covering all fields of nanotechnology.

On the scientific side, VISTEC members are contributing extensively to this conference by hosting, chairing, co-chairing, and presenting in all the sessions. Together with our co-host NANOTEC, we aim to showcase advanced and innovative nanoscience and nanotechnology research conducted in Thailand. Our members are hosting and presenting in the following sessions:

- **Session 4**: Nanomaterials and Nanotechnology for Electronic/Optoelectronic Devices and Sensors,
- **Session 5**: Nanomedicine, Nanosensor and Nano-biotechnology,
- **Session 6**: Nanotechnology for Energy Storage and Management,
- **Session 8**: Nanotechnology for Catalysis and Industrial Applications,
- **Session 9**: Nanotechnology for Startups and Industrial Enterprises, and
- **Special Session 1**: Advanced Nanostructured Materials for a Global Circular Economy.

We hope that these sessions will provide all participants insights into the current state of cutting-edge research work at VISTEC.

NanoThailand 2023 will provide all participants excellent opportunities to exchange ideas, network professionally, and broaden their knowledge. We hope that you all will have fruitful meetings and enjoy activities at Dusit Thani Hotel, the City of Pattaya, EECi and VISTEC during your excursion, as well as other places you visit in Thailand. Once again, on behalf of Vidyasirimedhi Institute of Science and Technology

NanoThailand 2023 Committee

Executive Advisory Committee

Dr. Wannee Chinsirikul
Assoc. Prof. Dr. Surin Laosooksathit
Mr. Por Punyaratabandhu
Mr. Phoosak Hiranyatrakul
Dr. Pavadee Aungkavattana
Dr.Premwit Jareewaruroj
Dr. Sirasak Teparkum
Dr.Winyoo Sangthong
Prof. Dr. Sanong Ekgasit
Mr.Ramjitti Indaraprasirt
Assoc. Prof. Khemarath Osathaphan
Asst. Prof. Dr. Nuankanya Sathirapongsasuti
Prof. Dr. Pimchai Chaiyen
Prof. Dr.Jumras Limtrakul
Asst. Prof. Dr. Tanakorn Osotchan
Prof. Dr. Santi Maensiri
Assoc.Prof.Dr.Werasak Surareungchai
Prof. Dr. Ekaphan Sawatsitang
Prof.Dr. Metta Chareonpanich
Prof.Dr.Paitoon Rashatasakhon
Prof. Dr. Tararaj Dharakul
Prof. Dr. Santi Maensiri
Assoc.Prof.Dr.Werasak Surareungchai

International Advisory Committee

Prof. Dr. Susumu Kitagawa
Prof. Dr. Alexander Kuhn
Prof. Dr. Mi-Jung Choi
Prof. Dr. Hiromi Nakai
Prof. Dr. Zhang Ruiqin
Prof. Dr. Natalie Stingelin
Prof. Dr. Thomas Anthopoulos
Prof. Dr. Damion Corrigan
Prof. Dr. Alberto Escarpa
Prof. Dr. Puangrat Kajitvichyanukul
Prof. Dr. George Shimizu
Prof. Dr. Deanna M. D'Alessandro
Prof. Dr. Cees Dekker
Prof. Dr. Emiel Hensen
Prof. Dr. Ming-Kang (Brad) Tsai
Prof. Dr. Navadol Laosiripojana
Prof. Dr. Giovanni Maglia
Prof. Dr. Haichen Wu
Prof. Dr. Mathias Winterhalter
Assoc. Prof. Dr. Neti Waranuch
Assoc. Prof. Dr. Nonglak Meethong
Dr. Jiaqian Qin
Dr.Jeng-Lung Chen

Scientific Committee

Prof. Dr. Vinich Promarak (Co-Chair)
Prof. Dr. Rattikorn Yimnirun
Prof. Dr. Martyn McLachlan
Prof. Dr. Martin Heeney
Dr. Nicola Gasparini
Prof. Dr. Guillaume Wantz
Prof. Dr. Hiroshi Yamamoto
Prof. Dr. Fabrice Goubard
Assoc. Prof. Dr. Pongsakorn Kanjanaboos
Dr. Watcharaphol Paritmongkol
Prof.Dr.Byoung Hun Lee
Prof.Dr.Jinho Ahn
Prof.Dr.Rino Choi
Prof. Dr. Albert Schulte
Assoc. Prof. Dr. Patiparn Punyapalakul
Dr. Chalita Ratanatawanat
Dr. Tomohiro Fukushima
Asst. Prof. Dr. Atthapon Srifa
Assoc. Prof. Dr. Valerio D'Elia
Assoc. Prof. Dr. Preeyanuch Sangtrirutnugul
Dr. Pongkarn Chakthranont
Prof. Dr. Guillaume Wantz
Dr. Chuchawin Changtong
Dr. Panachit Kittipanya-ngam
Dr. Pimpisut Worakajit
Dr. Suwussa Bamrungsap
Dr. Kantapat Chansaenpak
Assoc.Prof.Dr.Prapasiri Pongprayoon
Prof. Dr. Pierre-Henri Aubert
Dr. Pawin Iamprasertkun
Dr. Salatan Duangdangchote
Dr.Udom Asawapirom
Dr.Varol Intasanta
Dr.Nuttaporn Pimpha
Dr.Warayuth Sajomsang
Dr,Kittiwut Kasemwong
Dr.Kanokwan Sansanaphongpricha
Dr.Tanyakorn Muangnapoh
Dr.Anchalee Junkaew
Dr.Waluree Thongkam
Dr.Sasitorn Aueviriyavit
Dr.Pisist Kumnorkaew
Dr.Tanyakorn Muangnapoh
Dr.Kritapas Laohhasurayotin
Dr.Annop Klamchuen
Dr.Thitikorn Boonkoom
Dr. Bunyarat Rungtaweevoranit
Dr. Supawadee Namuangruk (Secretary)

Dr.Kajornsak Faungnawakij (Co-Chair)
Prof. Dr.Siriporn Jungsuttiwong
Prof. Dr. Richard E. Palmer
Dr.Prompong Pienpinijtham
Dr. Che Boyang
Prof. Dr. Ho-Hsiu Chou
Prof. Dr. Xiaolei Fan
Assoc. Prof. Dr. Alejandro Montoya
Prof. Dr. Neso Sojic
Prof. Dr. Kevin C.-W. Wu
Prof. Dr. Tetsu Yonezawa
Dr. Kaito Takahashi
Prof. Dr. Evgeny Pidko
Asst.Prof. Dr. Thidarat Imyen
Assoc. Prof. Dr. Satoshi Watanabe
Assoc. Prof. Dr. Serena Arnaboldi
Prof. Dr. Li-Hsien Yeh
Prof. Dr. Lin Zhang
Prof. Dr. Akira Nakayama
Dr. Jayeon Baek
Dr. Chotitath Sanpitakseree
Dr. Sanchai Kuboon
Prof. Dr. Noppadon Sathitsuksanoh
Dr. Thidathip Wongsurawat
Prof. Dr. Wipa Suginta
Dr. Nuankanya Sathirapongsasuti
Dr. Piroon Jenjaroenpun
Dr. Oraphan Sripichai
Dr. Pongpun Sawatwong
Dr. Kanokwan Sansanaphongpricha
Dr. Thongchai Koobkokkruad
Assoc. Prof. Dr. Supareak Praserthdam
Asst. Prof. Dr. Pichaya Pattanasattayavong
Assoc. Prof. Dr. Montree Sawangphruk
Asst. Prof. Dr. Sareeya Bureekaew
Assoc. Prof. Dr. Sarana Nutanong.
Dr.Watcharaphol Paritmongkol
Asst. Prof. Dr.Thanyaporn Wongnate
Assoc. Prof. Dr. Chularat Wattanakit
Assoc. Prof. Dr. Khamphee Phomphrai
Asst. Prof. Dr. Kanokwan Kongpatpanich
Dr.Chotitath Sanpitakseree
Dr.Teerapong Yata
Dr. Pinit Kidkhunthod
Dr.Orapan Sripichai
Dr.Thidathip Wongsurawat
Asst. Prof. Dr. Nuankanya Sathirapongsasuti
Miss Jirapat Santatiwongchai

Local Organizing Committee

Honorary Chairs of The Organizing Committee

Dr. Wannee Chinsirikul	Executive Director of the National Nanotechnology Center (NANOTEC)
Prof. Dr. Pimchai Chaiyen	President of Vidyasirimedhi Institute of Science and Technology (VISTEC)

Chairs of The Local Organizing Organizing Committee

Dr. Wiyong Kangwansupamonkon (NANOTEC)
Prof. Dr. Rattikorn Yimnirun (VISTEC)

Chairs of Scientific Committee

Dr. Kajornsak Faungnawakij (NANOTEC)
Prof. Dr. Vinich Promarak (VISTEC)

Sponsor Committee

Ms. Supinya Upalakalin
Dr. Panvika Pannopard

Registration Committee

Dr. Waluree Thongkam
Ms. Benyapa Suwan
Mr. Pongsit Ratanakonvit

Ceremony, Reception and Transportation Committee

Ms. Supornrat Raksuwan

Revenue Committee

Ms. Benyapa Suwan
Ms. Thasikan Popromsree

Finance Committee

Mr. Pongsit Rattanakonvit

Evaluation Committee

Mrs. Weeraya Khunkaew

Public Relations Registration Committee

Mr. Tortrakul Poolsopha

General Secretariat

Mr. Pongsit Rattanakonvit

Academic Sessions

Session 1: Nanoencapsulation and Functional Ingredients
Chair: Dr.Kanokwan Sansanaphongpricha
Co-chair: Dr.Teerapong Yata

Session 2: Theory and Simulation for Nanosystems
Chair: Prof.Siriporn Jungsuttiwong
Co-chairs: Dr.Anchalee Junkaew
Assoc. Prof.Sarana Nutanong

Session 3: Nanosafety and Standard
Chair: Dr.Waluree Thongkam
Co-chair: Dr.Sasitorn Aueviriyavit

Session 4: Nanomaterials and Nanotechnology for Electronic/Optoelectronic Devices and Sensors
Chair: Prof.Vinich Promarak
Co-chair: Dr.Pisist Kumnorkaew
Dr.Anusit Kaewprajak

Session 5: Nanomedicine, Nanosensor and Nano-biotechnology
Chair: Dr.Deanpen Japrung
Co-chairs: Prof.Albert Schulte
Dr.Weerakanya Maneeprakorn
Dr.Suwussa Bamrungsap

Session 6: Nanotechnology for Energy Storage and Management
Chair: Assoc. Prof.Montree Sawangphruk
Co-chair: Dr.Tanyakorn Muangnapoh

Session 7: Nanotechnology for Environment and Agriculture
Chair: Dr.Varol Intasanta
Co-chair: Dr.Warayuth Sajomsang

Session 8: Nanotechnology for Catalysis and Industrial Applications
Chair: Dr.Kajornsak Faungnawakij
Co-chair: Assist. Prof.Sareeya Bureekaew

Session 9: Nanotechnology for Startups and Industrial Enterprises
Chair: Dr.Paisan Khanchaitit
Co-chair: Dr.Pichaya Pattanasattayavong

Academic Sessions

Session 10: Nanocharacterization & Instrumentation

Chair: Dr.Annop Klamchuen

Co-chairs: Dr.Pinit kidkhunthod
Dr.Kitiphat Sinthiptharakoon
Dr.Narong Chanlek

Session 11: Special Session 1: Advanced Nanostructured Materials for a Global Circular Economy

Chair: Assoc. Prof.Chularat Wattanakit

Co-chair: Dr.Supawadee Namuangruk

Session 12: Special Session 2: Symposium on Bio-based Chemicals & Fuels from Lignocellulose 2023 (Hub of Knowledge)

Chair: Dr.Bunyarat Rungtaweevoranit

Co-chair: Dr.Chotitath Sanpitakseree

Session 13: Special session 3: The 2nd Thailand Symposium on Nanopore technology

Chair: Dr.Deanpen Japrung

Co-chairs: Dr.Orapan Sripichai
Dr.Thidathip Wongsurawat
Dr.Nuankanya Sathirapongsauti
Dr.Thitikorn Boonkoom

Minimally Invasive Glucose Monitoring with Molecularly Imprinted Polymer-Based Microneedle Biosensors

Harit Pitakjakpipop[1], Warittha Thongkham[2], Thitikorn Boonkoom[2], Paisan Khanchaitit[2,*], Pakorn Opaprakasit[1,*]
[1] *School of Integrated Science and Innovation, Sirindhorn International Institute of Technology (SIIT), Thammasat University, Pathum Thani 12121, Thailand*
[2] *National Nanotechnology Center (NANOTEC), National Science and Technology Development Agency (NSTDA), 111 Thailand Science Park, Pathum Thani 12120, Thailand*
E-mail: paisan@nanotec.or.th, pakorn@siit.tu.ac.th

Abstract:

Diabetes is typically diagnosed by monitoring blood glucose levels through invasive methods, offering critical health information. However, the accuracy of enzyme-based glucose sensors is constrained by variances in strip manufacturing, improper storage, and aging. To address these limitations, a molecularly imprinted polymer (MIP) sensor on microneedles (MN) has been developed for an electrochemical non-enzymatic approach to monitor glucose levels beneath the skin without the need for blood drawing. Employing a convenient photolithography method, a cross-shaped microneedle was fabricated using a non-cytotoxic bio-based resin derived from soybean oil and methyl methacrylic acid, demonstrating excellent mechanical properties. Electroless plating and sputtering methods were then utilized to coat the microneedle patch. Subsequently, the MIP membrane was deposited on gold microneedle electrodes using methacrylic acid (MAA) and ethylene glycol dimethacrylate (EGDMA) as matrix materials in the presence of a glucose template. The microneedle MIP sensor effectively detected glucose in the range of 50 to 800 mg/dL via differential pulse voltammetry (DPV). This work presents a simple and effective sensing platform that overcomes the limitations of microneedle electrode fabrication and enzyme-based strip sensors, making it a promising tool for accurate and reliable non-invasive diagnosis in the future.

1. Introduction

Presently, the growing number of diabetes cases has led to an increased demand for and utilization of test strips. However, enzyme-based strips require careful storage in cool and dry places, inside a closed container, and away from direct light to maintain the accuracy and reliability of results[1]. Moreover, pricking blood from fingertips using a lancet can cause significant pain and inflammation, posing a risk of infection.

Recently, the diagnostic utility of interstitial fluid (ISF) has increased to avoid the pain and limitations associated with withdrawing blood from fingers or using whole blood, as it contains biomarkers comparable to those found in blood[2]. MNs are among the most suitable devices for accessing ISF due to their optimal length, typically ranging from 200 to 1500 μm[3]. Therefore, the use of microneedles for transdermal glucose monitoring is highly feasible for conducting painless measurements[4].

Herein, a biocompatible copolymer with photo-crosslinking properties has been synthesized for microneedle fabrication. Additionally, a suitable gold coating technique[5] and deposition of molecularly imprinted polymers (MIPs) onto the microneedle electrode have been chosen due to their key features, making them excellent receptors in biosensors for sensitivity and selectivity, as shown in Scheme 1.

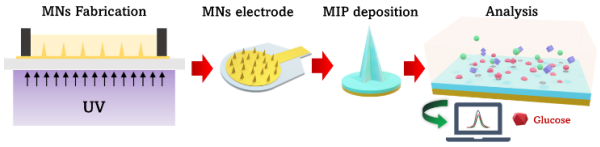

Scheme 1. Schematic diagram of the fabrication process of microneedle MIP glucose sensor.

2. Materials and Methods

2.1 Materials

Acrylic acid (AAc), methacrylic acid (MAA), acrylated epoxidized soybean oil (AESO), methyl methacrylate (MMA), 2,2-dimethoxy-2-phenylacetophenone (DMPA), stearyl trimethyl ammonium chloride (SC), dimethylformamide (DMF), chloroplatinic acid hexahydrate ($H_2PtCl_6 \cdot 6H_2O$), auric chloride ($HAuCl_4$), potassium hexacyanoferrate (III), and potassium hexacyanoferrate(II) trihydrate were obtained from Sigma-Aldrich (St. Louis, MO, USA). D-glucose and potassium chloride (KCl) were obtained from Kanto Chemicals (Chuo-ku, Tokyo, Japan).

2.2 Synthesis of AESO Resins

AESO-based resins were synthesized to create MN arrays and substrate sheets for the MN

patches. The resin for microneedle's substrate (B-resin) was formulated by dissolving 100 mg of DMPA in 2 mL of AAc until a homogeneous mixture formed, which was then poured into AESO (8 mL). The MN arrays resin (MN-resin) was prepared by dissolving 100 mg of DMPA in 3 mL of MMA and then poured into AESO (7 mL). All resins were stirred for 24 hours in a dark room at room temperature, covered with aluminum foil, and stored at room temperature before use.

2.3 Photomask Preparation

A photomask was employed to block UV radiation, preventing photopolymerization beyond the zones of the microneedle array. Initially, a glass slide was cleaned and sputtered with a 40 nm thick layer of aluminum on one side. Subsequently, cross-shaped micro-windows with a diameter of 400 µm were etched onto the aluminum film using a low-energy laser.

2.4 Preparation of Microneedle Patches

The microneedle's substrate was created by pouring 100 µL of B-resin over a photomask slide, covering it with a transparent plastic sheet with a 0.2 mm spacer, and exposing it to 10 seconds of UV irradiation. MN-resin was then filled into a PDMS frame and exposed to UV irradiation from beneath for 120 seconds, as depicted in Scheme 1. Subsequently, 3D MN arrays were formed and rinsed three times with ethanol and distilled water to eliminate non-polymerized monomers, before undergoing an additional 120 seconds of UV exposure to complete the curing reaction

2.5 Microneedle Electrode Coating Process

Electroless plating and sputtering methods were employed to deposit a gold layer onto the 3D structure of the microneedles (MNs), creating a working electrode for sensor devices. The MN patches were immersed in a 0.1% solution of stearyl trimethyl ammonium chloride (SC) for 10 seconds to deposit a positively charged surface. Next, the MN patches were immersed in a Pt colloid for 60 seconds, enabling Pt nanoparticles to spontaneously adhere to the surface through electrostatic contact between the cationic charge-modified substrate and the negatively charged Pt colloid particles. The remaining free Pt particles were gradually removed by rinsing them with distilled water. Subsequently, the MN patches were placed in a plating tube containing 10 mM $HAuCl_4$, and 20 mM H_2O_2 was added while shaking the plating tube for 5 minutes. The electrodes were then dried at 50 ºC for 2 h. Finally, a gold-sputtering process was performed at a current of 50 mA to achieve a film thickness of 100 nm. Once the desired thickness was reached, the MN electrodes underwent annealing at 70 ºC in an oven for 3 h to ensure a uniform coating.

2.6 Cytotoxic Assay

L929 cells (American Type Culture Collection, Manassas, VA, USA) were cultured in Dulbecco's modified Eagle's medium (Sigma-Aldrich, St. Louis, MO) supplemented with 10% heat-inactivated fetal bovine serum in a humidified atmosphere of 5% CO_2 at 37 °C. Before *in vitro* cytotoxicity testing, 100 mg of cured MN-resin was immersed in 1 mL of cell culture medium. The cytotoxicity assay was conducted using the MTT method in a 96-well plate. Subsequently, 1×10^3 cells in 0.1 mL of culture media were seeded in a 96-well plate. After 72 h of incubation, 0.1 mL of culture medium containing different concentrations of the extracted polymers was added to the 96-well plate. Following an additional 24 h of re-incubation, 0.1 mL of the MTT solution (300 µg/mL) was added to each well, and the cells were incubated for an extra 3 h. After discarding the medium, 0.1 mL of DMSO was added to dissolve the generated purple formazan crystals. The number of viable cells was determined at 540 nm.

2.7 Porcine Skin Insertion Tests

The penetration performance of MNs was evaluated using porcine skin as a model. Fresh porcine skin was obtained from the pig's back area, sliced into 3-4 mm thickness, and stored at -3 to -5 ºC. Prior to use, the frozen porcine skin was placed in a bag and thawed in water at room temperature. A skin slice was positioned on a flat surface, and the MN electrode was inserted using a thumb-pressing force for 20 seconds.

2.8 MIP Electropolymerization

The gold MN electrodes were initially cleansed with ethanol and PBS. For the second cleaning step of the gold surface, Cyclic voltammetry (CV) was performed with a scanning rate of 50 mV/s in PBS (pH 7.4), containing 0.1M KCl, 2.5 mM $K_3Fe(CN)_6$, and 2.5 mM $K_4Fe(CN)_6$. This process utilized a three-electrode system for 10 cycles or until a stable signal was obtained. Subsequently, 50 µL of 0.05 M allyl mercaptan in a 50% v/v ethanol/water solution was applied to the gold MNs electrodes within a closed container. The reaction proceeded for 30 min. The modified

substrate was washed with ethanol and then dried in an oven at 50 ºC to eliminate the solvent. MIP solution was prepared by mixing two solutions of glucose (40 mg) and KCl (0.1 M) with 1 ml PBS in 9 ml DMF. A functional monomer MAA (93µL), crosslinker EGDMA (335.27 µL), and AIBN (50 mg) and DMPA (50 mg) initiators were added to the solution. N_2 gas was bubbled in the mixed solution for 5 min, then stirred for 2 h. The MIP layer was deposited via electropolymerization by CV (10 cycles) with the three-electrode system in a potential range of −400 to +600 mV vs. Ag/AgCl at a scan rate of 50 mV/s. After completing the electropolymerization process, the resulting polymer was exposed to UV irradiation for 5 min to ensure full curing, followed by drying at 50 ºC for 30 min. The materials were rinsed with ethanol to remove the uncured monomer. Finally, the glucose template molecules were removed from the polymer matrix film by dripping it with acetic acid (20 mM) in acetonitrile (20% in water) for 30 min. A control polymer substrate (non-imprinting polymer, NIP) was prepared with the same procedure described above without glucose.

2.9 Electrochemical Measurements

CV was employed to evaluate the performance of the modified MN electrodes. The experiment was conducted using the three-electrode system consisting of Ag/AgCl (RE), Pt (CE), and the modified microneedle electrode (WE) at a scan rate of 10-200 mV/s. Differential pulse voltammetry (DPV) was explored with the same three-electrode system, ranging from −0.1 to 0.6 V, with a modulation amplitude of 0.025 V, modulation time of 0.005 seconds, step of 0.005 V, and interval time of 0.1 seconds. All electrochemical measurements were carried out in a solution containing 0.1M KCl, 2.5 mM $K_3Fe(CN)_6$, and 2.5 mM $K_4Fe(CN)_6$.

3. Results and Discussion

3.1 Microneedle Patch Fabrication Process

A thin sheet substrate, with a fixed thickness of approximately 200±20 µm, was fabricated from B-resin to control the intensity of UV light passing through micro-sized windows. This ensures uniform maintenance of microneedle length, height, and shape. The microneedle design, featuring a four-point star shape, aims to reduce the wound size at the insertion site compared to cones or pyramids. The four-points star shape, with a higher surface area than squares or circles based of the same dimensions and height, enhances sensor modification on this microneedle type, providing more reaction sites and generating a larger signal, as shown in Figure 1.

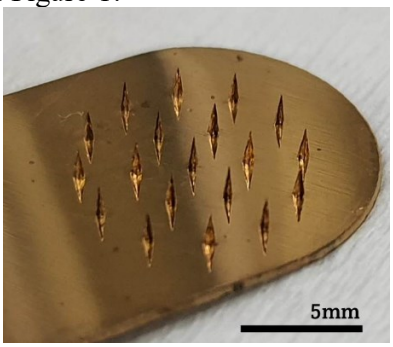

Figure 1. The appearance of the MN electrode.

3.2 Surface Coating of Microneedles

The electroless plating method resolves shadow issues encountered with the sputtering method. A continuous gold thin film is formed at room temperature due to the excellent catalytic properties of the Pt nanoparticles. Figure 2A displays the initial layer of gold deposited through electroless plating, with gold nanorods approximately 10–20 nm in diameter and 50–100 nm long. Subsequently, the electrode underwent gold nanoparticle sputtering, resulting in a 100 nm thick gold film deposition. Larger-sized gold particles were observed after the second layer of deposition, ranging from about 60–300 nm, as shown in Figure 2B. Figure 2C illustrates the two stages of the gold nanoparticle coating process, covering the entire area of the microneedle electrodes, particularly at the tip and base of the microneedles. Figure 2D shows the finished MN electrode with a resistance value lower than 3 Ohms, measured from the furthest MN tip on the left to the furthest connector on the right.

3.3 Microneedle Insertion study

The microneedle's in vitro skin insertion behavior was investigated on a slice of porcine skin. The microneedles penetrated to a depth of around 300-400 µm, as seen in Figure 3A, Given that porcine skin is harder, thicker, and fatter than human skin, the microneedle electrode has sufficient penetrating capability for use with human skin.

3.4 Cytotoxicity Tests

The IC_{50} (the concentration at which 50% of the cells are killed) was not observed for any concentration in the extract medium concentrations, as shown in Figure 3B. Therefore, the MN materials are highly biocompatible and can

be safely used in living organisms for transdermal applications.

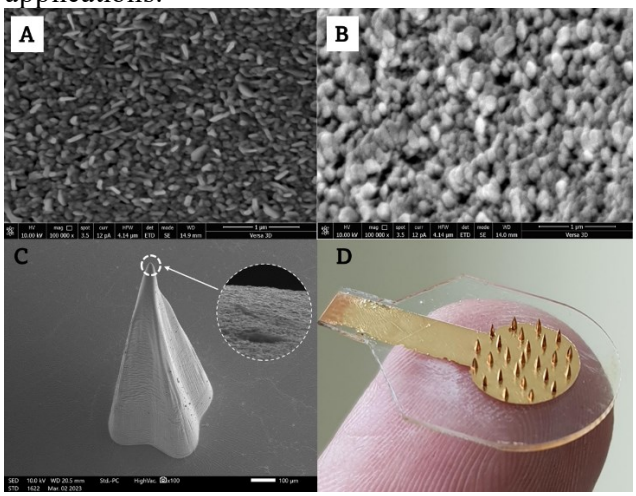

Figure 2. SEM images of gold layers on the MNs electrode by; (A) The first layer of the electroless plating, (B) the second layer of the sputtering method, (C) A full coverage of gold nanoparticles on the microneedle electrode, (D) appearance of the resulting microneedle electrode.

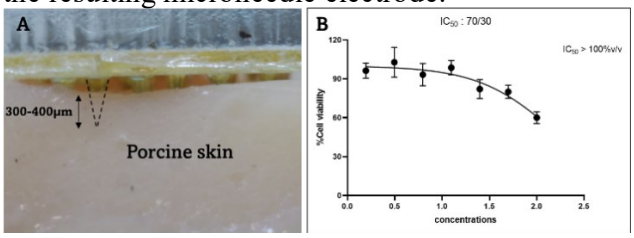

Figure 3 The insertion behavior of the microneedle electrode on porcine skin (A) cross-section view, (B) MTT assay to determine the IC_{50} value of microneedle material extracts at different concentrations.

3.5 MIP Microneedle Electrode Behavior

The performance of the MIP MN glucose sensors and electrode were evaluated. The allyl mercaptan-modified electrode (curve b) shows a lower oxidation peak compared to the bare electrode (a), attributed to the presence of a vinyl group layer, as depicted in Figure 4A. The lowest oxidation peak is observed in MIP (curve c) before the template is removed, indicating a thicker polymer block for electron transfer. After removing the template, curve d exhibits a distinct oxidation peak in MIP, suggesting an increase in the degree of electron transfer. The effects of scan rate on the electrochemical behavior of glucose at the glucose MIP MN sensors were investigated by CV. With increasing the scan rates in 50 mg/dL glucose, the anodic peak currents increased, and the peak potential moved slightly in a more positive direction. An anodic (I_{pA}) and cathodic (I_{pC}) peak currents are linearly proportional to the square root of the scan rate ($v^{1/2}$, V/s) over the range of 10 to 200 mV/s, as shown in Figure 4B. The linear regression equations are $I_{pA} = 1.0206v^{1/2} + 0.0455$, ($R^2 = 0.9989$) and $I_{pC} = -1.2531v^{1/2} - 0.0052$, ($R^2 = 0.9928$), respectively. Thus, anodic and cathodic currents are diffusion-controlled processes and reversible electron transfer kinetics at the MIP MNs sensor.

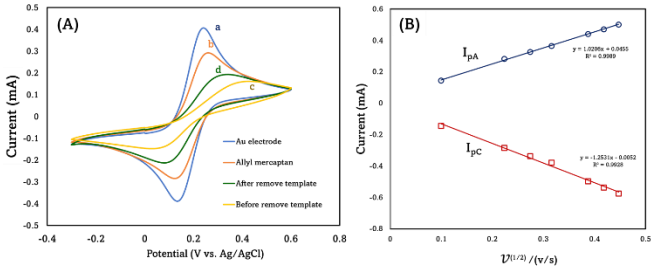

Figure 4 (A) CV plots of (a) gold electrode, (b) Allyl mercaptan modified electrode, (c) MIP before removing the template, and (d) MIP after removing the template, at a scan rate of 50 mV/s. CV plots of the MIP microneedle electrode, (B) A linear relationship plot of the anodic (I_{pA}) and cathodic peak current (I_{pC}) vs. the square root of the scan rate using 25 mg/dL glucose solution, all measurements were performed in PBS (pH 7.4) containing 0.1M KCl, 2.5 mM $K_3Fe(CN)_6$ and 2.5 mM $K_4Fe(CN)_6$.

3.6 Voltammetric Detection of MIP and NIP MNs Sensor

DPV measurements were conducted by scanning from −0.1 to 0.5 V. At each step, the template was removed for the next measurement by rinsing it with distilled water and immersing the electrode in 5 mL of acetic acid (20 mM) in acetonitrile (20% in water) for 5 min. Figures 5A and 5C illustrate the DPV and peak current plots of the MIP microneedle sensor at various glucose concentrations. The peak current shifts toward higher potentials (from 0.0192 V to 0.0237 V) as glucose molecules bind to the imprinted site and block electron transfer. With increasing glucose concentrations, the peak current of the MIP microneedle sensor decreases significantly. The electrochemical signal logarithmically reduces up to 800 mg/dL, represented by $y = -0.01\log(G) + 0.0019$, $R^2 = 0.9766$, as shown in Figure 5D. The linear range of the MIP microneedle glucose sensor is 50-800 mg/dL, suitable for applications in hyperglycemia and type 1 diabetes. The NIP sensor served as a standardized comparison with

the MIP sensor, both assembled from the same monomer and crosslinker to confirm that the NIP sensor does not react with any analyzer. DVP peak currents, as shown in Figure 5B, indicate that the curves remain relatively stable in the same range of glucose concentrations compared to the MIP sensor. Additionally, all peak currents generated from the NIP microneedle electrode do not shift to a higher potential as glucose concentrations increase.

4. Conclusions

The MIP glucose sensor based on a microneedle electrode has been successfully developed, utilizing a novel and convenient fabrication process with a bio-based and bio-compatible resin derived from soybean oil. This process enables efficient and rapid production of microneedle patches within 5 minutes, with high potential for scalability to industrial production. Gold electroless plating and the sputtering method were effectively employed to coat a conductive layer, addressing incomplete coverage issues inherent in microneedle-based systems. The microneedle (MNs) sensors exhibit outstanding mechanical characteristics, enabling penetration for the analysis of chemicals in interstitial fluid (ISF). The MIP microneedle sensor measurements demonstrate a linear relationship between ΔI and log(glucose concentration) for DPV, within a range of 50 to 800 mg/dL, indicating the suitability of these sensors for point-of-care testing (POCT). MIP-based biosensors on microneedles present a promising solution to overcome the limitations of enzyme-based sensors, especially concerning temperature effects, and offer non-invasive monitoring.

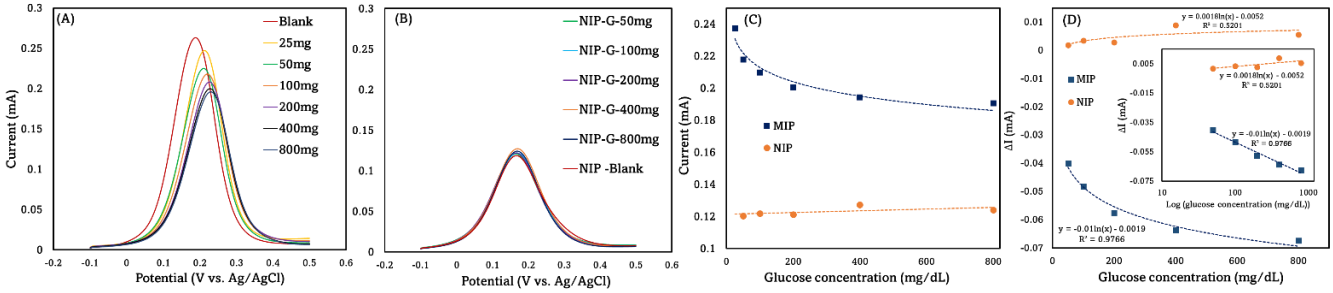

Figure 5. DPV curves of (A) MIP-1 microneedle electrode, (B) NIP at different glucose concentrations. (C) Relationship between changes in the peak current and glucose concentration. (D) A calibration plot of the linear relationship between the change in peak current and the log (glucose concentration).

Acknowledgments

Harit Pitakjakpipop is grateful for the scholarship support from the JAIST-SIIT-NSTDA collaborative program. Support from the Center of Excellence in Functional Advanced Materials Engineering (CoE FAME), SIIT, Thammasat University, is gratefully acknowledged.

References

(1) Olansky, L.; Kennedy, L. Finger-Stick Glucose Monitoring: Issues of Accuracy and Specificity. *Diabetes Care* **2010**, *33* (4), 948–949.

(2) Samant, P. P.; Niedzwiecki, M. M.; Raviele, N.; Tran, V.; Mena-Lapaix, J.; Walker, D. I.; Felner, E. I.; Jones, D. P.; Miller, G. W.; Prausnitz, M. R. Sampling Interstitial Fluid from Human Skin Using a Microneedle Patch. *Sci. Transl. Med.* **2020**, *12* (571). 285.

(3) Pitakjakpipop, H.; Rajan, R.; Tantisantisom, K.; Opaprakasit, P.; Nguyen, D. D.; Ho, V. A.; Matsumura, K.; Khanchaitit, P. Facile Photolithographic Fabrication of Zwitterionic Polymer Microneedles with Protein Aggregation Inhibition for Transdermal Drug Delivery. *Biomacromolecules* **2022**, *23* (1), 365–376.

(4) Ma, S.; Li, J.; Pei, L.; Feng, N.; Zhang, Y. Microneedle-Based Interstitial Fluid Extraction for Drug Analysis: Advances, Challenges, and Prospects. *J. Pharm. Anal.* **2023**, *13* (2), 111–126.

(5) Horiuchi, S.; Nakao, Y. Platinum Colloid Catalyzed Etchingless Gold Electroless Plating with Strong Adhesion to Polymers. *Surf. Coatings Technol.* **2010**, *204* (23), 3811–3817.

Chitosan Blending with Water-Soluble Polymers as Dissolving Microneedles for Controlled Drug Release

Fuad Saleh[1*], Supason Wanichwecharungruang[1]
[1]*Department of Chemistry, Faculty of Science, Chulalongkorn University, Thailand*
*E-mail: fuadsaleh44@yahoo.com

Abstract:

Chitosan has gained significant interest due to its ability to film-forming, biodegradability, and biocompatibility, making it suitable for topical and transdermal drug delivery such as fabricating microneedles. In this study, chitosan microneedles were prepared by incorporating (PVP) and (PVA) in ratios (1:1, 2:1, and 3:1 chitosan: polymers) to control drug release. The mechanical properties were tested using the universal testing machine (UTM), and the skin penetration ability was tested using pig skin (*ex vivo*). The results indicated that the microneedles exhibited sufficient strength to penetrate the outer layer of the porcine skin effectively. The study included incorporating two drugs: 13% w/w of curcumin as a model of hydrophobic drugs, and 32% w/w of butterfly pea extract as a model of hydrophilic drugs. Chitosan blended with PVP demonstrated the ability to finely tune the release profiles of both hydrophobic and hydrophilic drug models, with approximately 60% of hydrophilic and 48% of hydrophobic loaded drugs over two days. In contrast, chitosan blended with PVA did not exhibit a significant difference from the blank microneedles, releasing 49% of the loaded drugs over the same time frame. Chitosan microneedles incorporating PVP are a promising candidate for controlled transdermal drug delivery.

1. Introduction

Dissolving microneedles DMNs are usually made of biodegradable or dissolving polymers and have attracted a lot of curiosity in recent years [1-3]. Nevertheless, these microneedles disintegrate fast when they come into touch with moisture in the skin, which causes speedy drug distribution. Drugs can be effectively delivered into the skin using microneedles consisting of natural polymers such as hyaluronic acid (HA), polyvinyl alcohol (PVA), polyvinyl pyrrolidone (PVP), and maltose [4]. Carboxymethyl cellulose (CMC) [5] and Chitosan are modified natural polymers. Synthetic polymers such as PLGA[6]. Extended drug release may be possible using biodegradable microneedles composed of copolymer poly(lactic-co-glycolic acid) (PLGA) [7]. PLGA is a family of FDA-approved biodegradable polymers that are physically durable and biocompatible and have been researched as a drug delivery vehicle for numerous medicines, proteins, and macromolecules [8]. PLGA can potentially be used in a long-term drug delivery system [9] its degradation rate can vary from weeks to several months to a year [10, 11]. However, PLGA is expensive and dissolves in an organic solvent such as dichloromethan[12]. This solvent is incompatible with silicone mold, making it difficult to utilize as a structural material for DMNs. PLGA has been blended with PVP to fabricate microneedles and tune the drug release for two weeks [13]. To overcome the limitations of PLGA, Chitosan-based delivery methods have benefits over other hydrophobic polymers such as PLGA for the encapsulation of biopharmaceuticals since it does not require organic solvents. It is cost-effective and degrades between weeks to months [14, 15]. Chitosan β-(1→4)-linked D-glucosamine and N-acetyl-D-glucosamine is a family of molecules with variations in their composition, size, and distribution of monomers rather than a single polymer with a well-defined structure [16]. Chitosan's biocompatibility, degradability, and nontoxicity have made it a popular drug delivery material. Chitosan matrix swelling and disintegration can release drugs contained in chitosan carriers, producing sustained-release action[14, 17]. Its safety as dietary supplements or medication carriers has been proven in animal and human models. Chitosan is a biocompatible polymer that is often utilized in delivery methods to help the formulation's wound-healing benefits [18]. The demonstration of material with the desired drug release rate could be achieved through the adjustment of the ratio between chitosan and water-soluble polymers such as PVP and PVA. This study aims to develop DMN patches made of chitosan blended with PVA and PVP for tunable and sustained release of hydrophobic and hydrophilic drugs.

2. Materials and Methods

2.1 Materials

Chitosan (deacetylated 85%), MW 30,000 was purchased from Seafresh Chitosan (lab) Co. Ltd. Thailand; Poly (vinyl alcohol) (PVA), MW 95,000; Polyvinylpyrrolidone (PVP) MW 40,000 were purchased from Sigma Aldrich. Glacial Acetic Acid (A.A) 99% and Sodium Hydroxide of analytical reagent grade were purchased from Emsure Co. Curcumin MW 368.38 was purchased from ACROS Co. Butterfly pea powder HQ was purchased from Tipco, Thailand Biotech Co. Ethanol was purchased from Sigma Aldrich. Polydimethylsiloxane molds (PDMS): (1.6 cm in diameter, containing 277 needles arranged with a tip-to-tip distance of 1150 µm; each needle is nail-shaped with 350×350×360 µm3 (W×L×H) square column and 500 µm high of the square pyramid on the top). The mechanical properties were measured by universal testing machine UTM, Shimadzu EZ-S, Shimadzu Corporation, Tokyo, Japan. The penetration ability was measured by using commercial porcine ear skin.

2.2 Synthesis

For the microneedle matrix, chitosan powder was dissolved in a 0.2 M aqueous solution of acetic acid to obtain a 3% (w/v) chitosan solution. The obtained viscous chitosan solution was then neutralized by adding drops of sodium hydroxide 0.5 M after that dialyzed at room temperature against deionized (DI) water with several water exchanges to remove excess acetic acid and salt (final pH approximately 5). 6% (w/v) of chitosan solution mixed with 9% (w/v) of HA, PAA, PVA, PVP, trehalose, and sucrose Table 1. The mixture was poured into the PDMS and dried overnight. Curcumin was dissolved with ethanol and loaded to the mold to make 13% w/w the maximum capacity of loading. Butterfly pea was dissolved with water and loaded to the mold to make 33% w/w the maximum capacity of loading.

2.3 Characterization

The needles with drugs and without drugs were applied onto the porcine skin to study the penetration efficiency. Mechanical compression tests were performed using a UTM. A microneedle array was placed on a stainless-steel base plate's flat inflexible surface. An axial force was applied by a moving sensor mount, perpendicular to the axis of the microneedle array, at a constant speed of 150 mm/min[19]. *In vitro* drug release has been studied. Briefly, needles with drugs were immersed in 100 ml PBS (pH 7.4) and a water jacket was used to control temperature at 37 ◦C. The drug solution released was acquired at predetermined time intervals (0, 0.25, 0.5, 01, 02, 04, 08, 12, 24, and 48 hours) through the sampling port and then measured using a UV machine. A comparison between the two groups was performed using ANOVA: single factor using statistical software (Graph Pad Prism 9). Data presented as mean ± SD. A difference of $P < 0.05$ was considered statistically significant.

Table 1. The amount of mixing between chitosan: polymers and sugars

Formations	CS: polymers & sugars	mg of materials	
		CS	polymers & sugars
1	1:1	45	45
2	2:1	60	30
3	3:1	67.5	22.5

3. Results

3.1 Fabrication of chitosan- HA, PAA, PVA, PVP, Trehalose and Sucrose

Sugars blended with chitosan showed brittle needles when the chitosan was the major component and sticky when the sugars were the major component. Sugar molecules are known to increase polymers' flexibility and water absorption capacity. This can lead to increased stickiness, especially in humid environments. The stickiness of microneedles could impact their handling and storage. It might also affect their ability to pierce the skin effectively if they adhere to the skin surface. The results showed a precipitate when HA and PAA blended with chitosan due to the difference in pka value at pH 5.0.

Blending chitosan with PVA and PVP showed good results. Increasing chitosan in microneedle formulation likely played a significant role in the transition from hollow to solid microneedles. Chitosan is known for its structural integrity and rigidity. This transition

may have occurred due to chitosan's ability to form a solid matrix when it interacts with the other polymers (PVA and PVP) in the formulations.

3.2 Drug-loading and skin penetration (ex vivo)

Curcumin has been loaded as a hydrophobic drug model. It was loaded to the formulation of chitosan: PVP and pure chitosan with a maximum loading capacity of 13% w/w.

Table 2. The effect of drug on the penetration efficiency

Formulation Wt. CS: wt. polymers	Drug loading and penetration efficiency	
	Curcumin w/w 13 %	Butterfly pea w/w 32%
CS	Curcumin enhanced the penetration	Good penetration
1 CS: 1 PVP	Curcumin enhanced the penetration	Good penetration
2 CS: 1 PVP	Curcumin enhanced the penetration	Good penetration
3 CS: 1 PVP	Curcumin enhanced the penetration	Good penetration
1 CS: 1 PVA	-	Good penetration
2 CS: 1 PVA	-	Good penetration
3 CS: 1 PVA	-	Good penetration

On the other hand, the formulation of chitosan: PVA didn't encapsulate curcumin. Butterfly pea extract has been loaded as a hydrophilic drug model. It was loaded to the formulation of chitosan: PVP, chitosan: PVA, and pure chitosan with a maximum loading capacity of 32% w/w Table 2. Besides mechanical property tests, we tested the insertion ability of the DMNs in porcine skin ex vivo. The needles successfully penetrate the porcine skin with different depths due to the different formulas and ratios.

The results show that the chitosan: PVP and pure chitosan formulations are suitable for the encapsulation of hydrophobic drugs like curcumin. However, chitosan: PVA formulation did not successfully encapsulate curcumin. This means that the combination of chitosan and PVA may not be suitable for encapsulating hydrophobic drugs like curcumin under the conditions or methods used in this study. Chitosan-based formulations can effectively encapsulate hydrophilic drugs. Interestingly, the results reveal that pure chitosan, without the addition of PVP or PVA, was able to encapsulate butterfly pea extract effectively.

The experiment successfully demonstrated that the needles penetrated the porcine skin to different depths. This variability in penetration depth suggests that the composition of the needles, as well as the ratios of the components in the patches, have an impact on how deeply the needles can penetrate the skin. The results indicated that the depth of the whole needles in all the ratios is more than 600 µm which is good enough to penetrate the stratum corneum reaching the epidermis layer. The statistical analysis approved that adding butterfly pea extract as a hydrophilic drug model didn't significantly affect the depth of the needles compared with adding curcumin. DMNs with curcumin penetrated deeper into the porcine skin.

3.3 Penetration efficiency

To overcome the barrier of the skin and deliver the drug efficiently into the skin, the mechanical property and the insertion ability are critical for DMNs. In brief, the DMN sample applied to the porcine ear skin and the needle's higth and depth has been measured to assess the penetration efficiency. As shown in Figure 1, all microneedles penetrate the skin succefuly.This result contributes to the overall understanding of microneedle technology and its potential for various medical and pharmaceutical applications.

3.4 Drug release in vitro

Chitosan sustains the release of butterfly (hydrophilic drug model) where around 44 % w/v has been released after 2 days from pure chitosan. chitosan blended with PVA showed faster drug release with increasing concentrations of PVA in the needles around 49%, 47%, and 46% w/v 1:1.

2:1, 3:1 CS: PVA respectively released after 2 days. the drug release decreased with the concentration of PVA. PVP blended with chitosan showed the fastest drug release 69%, 67%, and 48% w/v, from the ratio CS: PVP 1:1, 2:1, 3:1 respectively Fig. 2a.

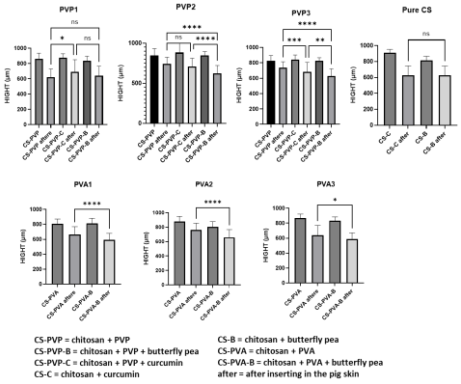

Figure 1. Statistical analysis of the needles' height in the patches and the needles' depth in porcine skin (PVP1 1:1 CS: PVP, PVP2 2:1 CS: PVP, PVP3 3:1 CS: PVP), (PVA1 1:1 CS: PVA, PVA2 2:1 CS: PVA, PVA3 3:1 CS: PVA), and pure CS (only chitosan with drugs, no polymers blended with chitosan). p-value control using ANOVA-single factor data analysis, <0.05 is considered statistically significant.

PVP is known for its solubilizing properties and ability to enhance drug release. The high drug release observed with CS: PVP blends, especially at the 1:1 ratio, indicates a strong influence of PVP on accelerating drug release 26. CS: PVP blends outperform CS: PVA blends in terms of drug release rate. This could be attributed to the distinct properties of PVP, which promotes rapid drug dissolution and diffusion 27. CS: PVP loaded with curcumin showed sustain release 55%, 45%, 39%, and 22% w/v from the ratio CS: PVP 1:1, 2:1, 3:1, and pure CS respectively Fig. 2b.

Conclusion

The incorporation of chitosan into blends with PVA and PVP in varying ratios has proven to be a promising approach for tunable drug release systems. The successful fabrication of composite needles with excellent mechanical strength, as determined by the Universal Testing Machine (UTM). Furthermore, the penetration of these

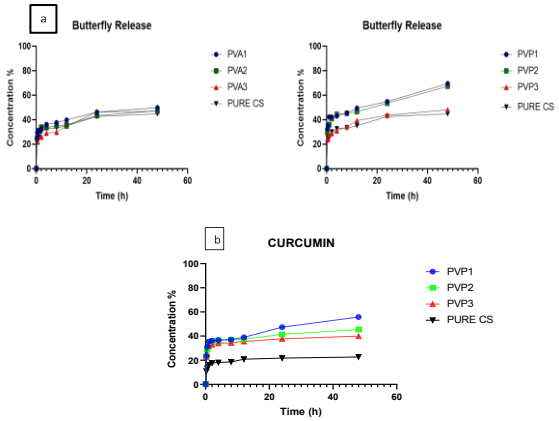

Figure 2. In vitro release profile of a) butterfly pea extract in CS: PVA (PVA1 1:1, PVA2 2:1, PVA3 3:1) and CS: PVP (PVP1 1:1, PVP2 2:1, PVP3 3:1), b) curcumin in CS: PVP (PVP1 1:1, PVP2 2:1, PVP3 3:1) patches

formulations through porcine ear skin demonstrates their potential for intradermal and transdermal drug delivery. The noteworthy finding in this study is the variation in drug release kinetics observed between chitosan-PVA and chitosan-PVP blends. After two days of testing, chitosan blended with PVP exhibited a notably faster drug release rate compared to chitosan-PVA blends. This suggests that the choice of polymer partner plays a crucial role in fine-tuning drug release profiles. These results underscore the importance of carefully selecting and optimizing the polymer blend composition to achieve the desired drug release characteristics. The versatility of chitosan as a biomaterial, when combined with appropriate polymers, opens up exciting possibilities for tailoring drug delivery systems to meet specific therapeutic requirements. Further research in this field could explore the potential applications of these formulations in controlled drug release for various medical scenarios

References

(1) Chu, L. Y.; Prausnitz, M. R. Separable arrowhead microneedles. *Journal of Controlled Release* **2011**, *149* (3), 242-249. DOI: https://doi.org/10.1016/j.jconrel.2010.10.033.
(2) Sullivan, S. P.; Koutsonanos, D. G.; Del Pilar Martin, M.; Lee, J. W.; Zarnitsyn, V.; Choi, S. O.; Murthy, N.; Compans, R. W.; Skountzou, I.;

Prausnitz, M. R. Dissolving polymer microneedle patches for influenza vaccination. *Nat Med* **2010**, *16* (8), 915-920. DOI: 10.1038/nm.2182 From NLM.
(3) Park, J.-H.; Allen, M. G.; Prausnitz, M. R. Biodegradable polymer microneedles: Fabrication, mechanics and transdermal drug delivery. *Journal of Controlled Release* **2005**, *104* (1), 51-66. DOI: https://doi.org/10.1016/j.jconrel.2005.02.002.
(4) Zhang, Y.; Jiang, G.; Yu, W.; Liu, D.; Xu, B. Microneedles fabricated from alginate and maltose for transdermal delivery of insulin on diabetic rats. *Mater Sci Eng C Mater Biol Appl* **2018**, *85*, 18-26. DOI: 10.1016/j.msec.2017.12.006 From NLM.
(5) Silva, A. C. Q.; Pereira, B.; Lameirinhas, N. S.; Costa, P. C.; Almeida, I. F.; Dias-Pereira, P.; Correia-Sá, I.; Oliveira, H.; Silvestre, A. J. D.; Vilela, C.; et al. Dissolvable Carboxymethylcellulose Microneedles for Noninvasive and Rapid Administration of Diclofenac Sodium. *Macromol Biosci* **2023**, *23* (1), e2200323. DOI: 10.1002/mabi.202200323 From NLM.
(6) Malek-Khatabi, A.; Sadat Razavi, M.; Abdollahi, A.; Rahimzadeghan, M.; Moammeri, F.; Sheikhi, M.; Tavakoli, M.; Rad-Malekshahi, M.; Faraji Rad, Z. Recent progress in PLGA-based microneedle-mediated transdermal drug and vaccine delivery. *Biomaterials Science* **2023**, *11* (16), 5390-5409, 10.1039/D3BM00795B. DOI: 10.1039/D3BM00795B.
(7) Panda, A.; Sharma, P. K.; McCann, T.; Bloomekatz, J.; Repka, M. A.; Murthy, S. N. Fabrication and development of controlled release PLGA microneedles for macromolecular delivery using FITC-Dextran as model molecule. *Journal of Drug Delivery Science and Technology* **2022**, *68*, 102712. DOI: https://doi.org/10.1016/j.jddst.2021.102712.
(8) Naves, L.; Dhand, C.; Almeida, L.; Rajamani, L.; Ramakrishna, S.; Soares, G. Poly (lactic-co-glycolic) acid drug delivery systems through transdermal pathway: an overview. *Progress in biomaterials* **2017**, *6*, 1-11.
(9) Makadia, H. K.; Siegel, S. J. Poly lactic-co-glycolic acid (PLGA) as biodegradable controlled drug delivery carrier. *Polymers* **2011**, *3* (3), 1377-1397.
(10) Gentile, P.; Chiono, V.; Carmagnola, I.; Hatton, P. V. An Overview of Poly(lactic-co-glycolic) Acid (PLGA)-Based Biomaterials for Bone Tissue Engineering. *International Journal of Molecular Sciences* **2014**, *15* (3), 3640-3659.
(11) Lu, Y.; Cheng, D.; Niu, B.; Wang, X.; Wu, X.; Wang, A. Properties of Poly (Lactic-co-Glycolic Acid) and Progress of Poly (Lactic-co-Glycolic Acid)-Based Biodegradable Materials in Biomedical Research. *Pharmaceuticals* **2023**, *16* (3), 454.
(12) Martins, C.; Sousa, F.; Araujo, F.; Sarmento, B. Functionalizing PLGA and PLGA derivatives for drug delivery and tissue regeneration applications. *Advanced healthcare materials* **2018**, *7* (1), 1701035.
(13) Rabiei, M.; Kashanian, S.; Bahrami, G.; Derakhshankhah, H.; Barzegari, E.; Samavati, S. S.; McInnes, S. J. P. Dissolving microneedle-assisted long-acting Liraglutide delivery to control type 2 diabetes and obesity. *European Journal of Pharmaceutical Sciences* **2021**, *167*, 106040. DOI: https://doi.org/10.1016/j.ejps.2021.106040.
(14) Chen, M. C.; Ling, M. H.; Lai, K. Y.; Pramudityo, E. Chitosan microneedle patches for sustained transdermal delivery of macromolecules. *Biomacromolecules* **2012**, *13* (12), 4022-4031. DOI: 10.1021/bm301293d From NLM.
(15) Chiu, Y.-H.; Chen, M.-C.; Wan, S.-W. Sodium Hyaluronate/Chitosan Composite Microneedles as a Single-Dose Intradermal Immunization System. *Biomacromolecules* **2018**, *19* (6), 2278-2285. DOI: 10.1021/acs.biomac.8b00441.
(16) Aranaz, I.; Alcántara, A. R.; Civera, M. C.; Arias, C.; Elorza, B.; Heras Caballero, A.; Acosta, N. Chitosan: An Overview of Its Properties and Applications. *Polymers (Basel)* **2021**, *13* (19). DOI: 10.3390/polym13193256 From NLM.
(17) Wang, J. J.; Zeng, Z. W.; Xiao, R. Z.; Xie, T.; Zhou, G. L.; Zhan, X. R.; Wang, S. L. Recent advances of chitosan nanoparticles as drug carriers. *Int J Nanomedicine* **2011**, *6*, 765-774. DOI: 10.2147/ijn.S17296 From NLM.
(18) Feng, P.; Luo, Y.; Ke, C.; Qiu, H.; Wang, W.; Zhu, Y.; Hou, R.; Xu, L.; Wu, S. Chitosan-Based Functional Materials for Skin Wound Repair: Mechanisms and Applications. *Frontiers in Bioengineering and Biotechnology* **2021**, *9*, Review. DOI: 10.3389/fbioe.2021.650598 Scopus.
(19) Lee, J. W.; Park, J. H.; Prausnitz, M. R. Dissolving microneedles for transdermal drug delivery. *Biomaterials* **2008**, *29* (13), 2113-2124. DOI: 10.1016/j.biomaterials.2007.12.048 From NLM.

Chage Transport Properties in Metal Halide Hybrid Perovskites: The Perspective of Large Polarons and Alloy Scatterng

Anusit Thongnum[1]*, Jamaree Amonkosolpan[1], and Songsak Phonghirun[1]

[1]*Department of Physics, Faculty of Science, Srinakharinwirot University, Bangkok 10110, Thailand*
**E-mail: anusit@g.swu.ac.th*

Abstract

Metal halide hybrid perovskites (MHPs) have drawn much attention due to the rapid progress in perovskite solar cells and their intriguing fundamental photophysical properties. Based on an initial power conversion efficiency (PCE) of 3.8%, they demonstrated a certified PCE of 26%. In MHPs, lead-halide and lead mixed-halide perovskites are forefront material systems with tunable electrical and optical properties. Charge-carrier mobility is an important factor that strongly affects the PCE of perovskite solar cells. However, a detailed understanding of the underlying transport mechanisms of these perovskite materials remains incompletely understood. Herein, we derive models of charge transport based on large polarons and alloy scattering to calculate charge-carrier mobilities and elucidate the transport mechanisms. The calculated RT mobility values were in very good agreement with the experimental results measured using an optical pump terahertz probe technique. In lead-halide perovskites, large polaron transport dominated the transport mechanism. Both large polaron transport and alloy scattering were dominant in lead mixed-halide perovskites.

1. Introduction

Metal halide perovskites (MHPs) have been widely investigated due to their potential applications in next generation photovoltaics.[1,2] This interest stems from both their advantageous optical and transport properties, which include high absorption coefficients, high charge-carrier mobilities and relatively long charge-carrier diffusion lengths, as well as high defect tolerance. Lead-halide and lead mixed-halide perovskites with the formula ABX_3 ($A = FA^+$, MA^+, Cs^+; $B = Pb^{2+}$; $X = I^-$, Br^-) are prototypical photoactive materials for perovskite solar cells (PSCs). An initial power conversion efficiency (PCE) of 3.8% has been demonstrated for a single-junction PSC based on $MAPbI_3$.[3] Up until now, a PCE of 26.1% has been certified.[4]

In charge-carrier mobility measurements, a room-temperature (RT) charge-carrier mobility is obtained using an optical pump terahertz probe (OPTP). This spectroscopy technique uses an optical pulse to create both free electrons and holes as well as a terahertz pulse to analyze the transport properties of charge carriers. The experimental results of RT mobility have been measured, such as in lead-halide perovskites,[5-7] $MAPbI_3$ (35 cm^2/Vs), $FAPbI_3$ (27 cm^2/Vs), $FAPbBr_3$ (14 cm^2/Vs), $FA_{0.83}Cs_{0.17}PbI_3$ (40 cm^2/Vs), $FA_{0.83}Cs_{0.17}PbBr_3$ (10 cm^2/Vs), and lead mixed-halide perovskites,[7] $FA_{0.83}Cs_{0.17}Pb(I_{1-x}Br_x)_3$ where x = 0.3 (24 cm^2/Vs), x = 0.4 (19 cm^2/Vs), x = 0.5 (15 cm^2/Vs), x = 0.6 (13 cm^2/Vs), and x = 0.7 (12 cm^2/Vs). However, a detailed explanation of these RT mobilities and underlying transport processes is still incomplete, both in lead-halide and lead mixed-halide perovskites.

In this work, we report an understanding of the transport properties of charge carriers in MHPs. We provide transport models of charge-carrier mobility that account for large polarons and alloy scattering to calculate the RT mobilities. Theoretical results were comparable to the experimental data.[5-7] It was found that these calculated results provided very good agreement with the experimental data measured using OPTP. Large polarons and alloy scattering provide the background transport mechanisms for redesigning strategies to provide efficient PSC absorption material development.

2. Methods and transport models

Based on OPTP, charge-carrier mobility can be determined from the product of the quantum yield of photon-to-charge conversion and sum of both electron and hole mobilities,[8] $\phi \sum \mu$, where $0 \leq \phi \leq 1$ and $\sum \mu = \mu_e + \mu_h$. From a theoretical perspective, carrier mobility is determined using $\mu = e\tau_{tr}/m^*$, where e is the elementary charge, τ_{tr} is the momentum relaxation time, and $m^*$is the effective mass of charge carriers (m_e^* for an electron and m_h^* for a hole). The effective mobility related to multiple scattering mechanisms can be calculated by Matthiessen's rule, $\mu_{tot}^{-1} = \sum_i \mu_i^{-1}$.

A brief review of transport models is presented, including large polarons and alloy scattering, to investigate RT mobility. First, a large polaron (LP) transport consists of a charge-carrier

coupled with a longitudinal optical (LO) phonon, with a polaron binding energy of $E_{\mathrm{P}} = 0.106\alpha^2\hbar\omega_{LO}$ and a polaron radius of $L_{\mathrm{P}} = \sqrt{\hbar/2m^*\omega_{LO}}$, based on a Fröhlich polaron theory. When an electron (or a hole) moves in a lattice, an ionic crystal polarization is created that follows the charge carrier motion, as shown in Figure 1(a). In Figure 1(b), a large polaron is formed, and a dressed particle is produced by a carrier coupled with an LO phonon cloud created from self-induced polarization. The carrier-phonon coupling constant describes the interaction strength between a carrier and LO phonons, $\alpha = \frac{e^2}{\hbar}\sqrt{\frac{m^*}{32\pi^2\varepsilon_0^2\hbar\omega_{LO}}}\left(\frac{1}{\varepsilon_\infty}-\frac{1}{\varepsilon_s}\right)$, where $\hbar\omega_{LO}$ is the effective LO phonon energy, ε_s is the static dielectric constant and ε_∞ is the high-frequency dielectric constant. Thus, the large polaron mobility is given by [9,10]

$$\mu_{\mathrm{LP}} = \frac{e}{2\alpha\omega_{LO}}\frac{1}{m^*(1+\alpha/6)^3}f(\alpha)\left(e^{\hbar\omega_{LO}/k_BT}-1\right). \quad (1)$$

The slowly varying function, $f(\alpha)$, is assumed to be unity.

Second, alloy scattering (AL) is a perturbative process where different atoms are randomly distributed inside the same lattice site. A random distribution of various atoms in lead mixed halides, *i.e.*, Br^- atoms substituted in I^- sites or *vice versa*, produces an alloy scattering potential (U). A simple model of the alloy scattering model is depicted in Figure 2. The alloy scattering strength is influenced by the concentration fraction of the alloying atoms (x), in which charge carriers scatter by randomly positioning various atoms or alloying atoms.[11] The alloy scattering mobility depends on the alloy scattering potential, thermal energy (k_BT), and volume of a unit cell related the lattice constant ($\Omega = a^3/4$). The mobility formula is given by [11]

$$\mu_{\mathrm{AL}} = \frac{16e\pi^{1/2}\hbar^4}{3(2m^*)^{5/2}\Omega U^2 x(x-1)(k_BT)^{1/2}}. \quad (2)$$

3. Results and discussion

In charge-carrier mobility calculations, we first examine the principle constant parameters, *i.e.*, $m_e^*, m_h^*, \varepsilon_\infty, \varepsilon_0, \hbar\omega_{LO}$ and a, for numerical evaluations of Eqs. (1) and (2). Table 1 shows the constant parameters for lead halides and lead mixed halides, respectively. To validate our transport models, theoretical results are compared with RT mobility data measured using OPTP spectroscopy. Nevertheless, to compute the alloy scattering mobility in Eq. (2), it is challenging to measure the alloy scattering potential and it needs to be specified as a fitting parameter. Calculated results for the Fröhlich coupling constant and RT charge-carrier mobility, as well as the experimental results, are presented in Tables 2 and 3 for lead-halide and lead mixed-halide perovskites, respectively.

We use the large polaron mobility in Eq. (1) to describe charge transport in lead-halide perovskite films, $MAPbI_3$, $FAPbI_3$, $FAPbBr_3$, $FA_{0.83}Cs_{0.17}PbI_3$, and $FA_{0.83}Cs_{0.17}PbBr_3$. In Table 2, calculated results of RT mobility are in very good agreement with experimental data. The results suggested that the large polaron transport model explains charge-carrier mobility well in lead halide films. Therefore, the polaronic effect has a major influence on the charge transport properties of MHPs. The calculated polaron binding energies and large polaron radii in MHPs are shown in Table 4. The binding energies of polarons, which range from 7.0 to 22.8 meV, are less than the thermal energy of 26 meV at room temperature (300 K). The large polaron radii between 24 and 40 Å are significantly greater than those of the PbI_3 octahedron (6.2 Å). These results suggest that the large polaronic effect has a band-like transport characteristic, where the carrier mobility decreases with increasing temperature, $\mu_{\mathrm{LP}} \propto T^{-m}$,[5,9] and atomic screening with a high tolerance to defects [5], respectively.

The alloy scattering potential in $FA_{0.83}Cs_{0.17}Pb(I_{1-x}Br_x)_3$ is caused by a random distribution of Br^- atoms in the I^- atom lattice sites. The polaronic effect is simultaneously dominant. Thus, we combine both transport mechanisms based on Matthiessen's rule, $\mu_{\mathrm{tot}} = (\mu_{\mathrm{LP}}^{-1} + \mu_{\mathrm{AL}}^{-1})^{-1}$, to examine charge-carrier mobility. In Table 3, theoretical calculations using the alloy scattering potential of U = 3.0 eV [11] provided good quantitative agreement with the experimental data. It is shown that the scattering from both LO phonons and alloy disorders are dominant scattering mechanisms. The strength of alloy scattering is determined by a concentration fraction factor, $x(x-1)$. This factor yields a minimal mobility value at $x = 0.5$. This indicates a relatively significant alloy interaction at limiting Br compositions with I/Br ratios closer to 1:1. The

mobility of an alloying system is lower than that of a pure compound. For this reason, alloy scattering cannot be ignored when analyzing the properties of charge transport in lead mixed-halide perovskites.

Based on this information, we can describe charge transport dynamics in MHPs. Through photoexcitation, hot carriers are generated (Process-1: carrier generation). These hot carriers rapidly relax to form free charge carriers in a scattering process *via* LO phonon emissions within a cooling time of 100 fs (Process-2: carrier relaxation). Free charge carriers, both electrons and holes, interact with LO phonons generated from self-induced polarization, leading to formation of large polarons within ~2 ps (Process-3: large polaron formation). Large polarons propagate through a material and scatter when they contact scattering sources (Process-4: charge scattering).

4. Conclusion

We examined charge-carrier mobilities in the metal halide hybrid perovskites. The calculated RT mobilities between 11 and 40 cm^2/Vs, revealed relatively high charge-carrier mobilities, which had a significant impact on the PCE of perovskite solar cells. Large polaron transport was the primary transport mechanism in lead-halide perovskites. Large polaron transport and alloy scattering were the two fundamental processes in lead mixed-halide perovskites. This work advances our knowledge of the transport mechanisms in MHPs and paves the way for the development of novel perovskite materials for solar energy conversion.

Acknowledgements

A. Thongnum would like to express gratitude to the National Research Council of Thailand (NRCT) and Srinakharinwirot University for funding under Grant No. NRCT5-RSA63020-02.

References

1. Kim, H. S.; Lee, C. R.; Im, J. H.; Lee, K. B.; Moehl, T.; Marcioro, A.; Moon, S. J.; Hamphry-Baker, R.; Yum, J. H.; Moser, J. E.; Grätzel, M.; Park, N. G., Lead Iodide Perovskite Sensitized All-Solid-State Submicron Thin Film Mesoscopic Solar Cell with Efficiency Exceeding 9%. *Sci. Rep.* **2012,** *2*, 591.
2. Lee, M. M.; Teuscher, J.; Miyasaka, T.; Murakami, T. N.; Snaith, H. J., Efficient Hybrid Solar Cells Based on Meso-Superstructured Organometal Halide Perovskites. *Science* **2012,** *338*, 643.
3. Kojima, A.; Teshima, K.; Shirai, Y.; Miyasaka, T., Organometal Halide Perovskites as Visible-Light Sensitizers for Photovoltaic Cells. *J. Am. Chem. Soc.* **2009,** *131*, 6050.
4. Best Research Cell Efficiencies. https://www.nrel.gov/pv/cell-efficiency.html (accessed November 18, 2023).
5. Milot, R. L.; Eperon, G. E.; Snaith, H. J.; Johnston, M. B.; Herz, L. M., Temperature-Dependent Charge-Carrier Dynamics in $CH_3NH_3PbI_3$ Perovskite Thin Films. *Adv. Func. Mater.* **2015,** *25*, 6218-6227.
6. Rehman, W.; Milot, R. L.; Eperon, G. E.; Wehrenfennig, C.; Boland, J. L.; Snaith, H. J.; Johnston, M. B.; Herz, L. M., Charge-Carrier Dynamics and Mobilities in Formamidinium Lead Mixed-Halide Perovskites. *Adv. Mater.* **2015,** *27*, 7938-7944.
7. Rehman, W.; McMeekin, D. P.; Patel, J. B.; Milot, R. L.; Johnston, M. B.; Snaith, H. J.; Herz, L. M., Photovoltaic Mixed-Cation Lead Mixed-Halide Perovskites: Links Between Crystallinity, Photo-stability and Electronic Properties. *Energy Environ. Sci.* **2017,** *10*, 361-369.
8. Johnston, M. B.; Herz, L. M., Hybrid Perovskites for Photovoltaics: Charge-Carrier Recombination, Diffusion, and Radiative Efficiencies. *Acc. Chem. Res.* **2016,** *49*, 146.
9. Thongnum, A.; Pinsook, U., Polaron Transport in Hybrid $CH_3NH_3PbI_3$ Perovskite Thin Films. *Nanoscale* **2020,** *12*, 14112.
10. Thongnum, A., Description of Electron Mobilities in Epitaxial Lanthanum-doped Barium Stannate Films: Influences of LO Phonons, Threading Dislocation, and Ionized Donor Defects. *J. Appl. Phys.* **2023**, *134*, 085701.
11. Thongnum, A.; Pingaew, R.; Pinsook, U., Impact of the Polar Optical Phonon and Alloy Scattering on the Charge-Carrier Mobilities of $FA_{0.83}Cs_{0.17}Pb(I_{1-x}Br_x)_3$ Hybrid Perovskites. *Phys. Chem. Chem. Phys.* **2021,** *23*, 27320.

Table 1. Constant parameters used in the mobility calculations at 300 K (m_0 is the free electron mass).

Material	m_e^*/m_0	m_h^*/m_0	ε_∞	ε_0	$\hbar\omega_{LO}$ (meV)	a (Å)
Lead halide [9,11]						
$MAPbI_3$	0.21	0.28	5.4	30.4	11.5	
$FAPbI_3$	0.22	0.27	5.5	45.0	11.5	
$FAPbBr_3$	0.35	0.40	4.5	43.0	16.5	
$FA_{0.83}Cs_{0.17}PbI_3$	0.22	0.27	5.5	45.0	15.0	
$FA_{0.83}Cs_{0.17}PbBr_3$	0.35	0.40	4.5	43.0	15.0	
Lead mixed halide [11]						
$FA_{0.83}Cs_{0.17}Pb(I_{0.7}Br_{0.3})_3$	0.22	0.27	5.5	45.0	13.0	6.202
$FA_{0.83}Cs_{0.17}Pb(I_{0.6}Br_{0.4})_3$	0.27	0.35	5.5	45.0	13.0	6.200
$FA_{0.83}Cs_{0.17}Pb(I_{0.5}Br_{0.5})_3$	0.27	0.35	5.5	45.0	13.0	6.144
$FA_{0.83}Cs_{0.17}Pb(I_{0.4}Br_{0.6})_3$	0.35	0.40	5.5	45.0	13.0	6.072
$FA_{0.83}Cs_{0.17}Pb(I_{0.3}Br_{0.7})_3$	0.35	0.40	5.5	45.0	13.0	6.041

Table 2. Calculated coupling constants, RT mobilities, and experimental data in lead halides.[5-7]

Material	α_e	α_h	$\mu_{LP,e}$ (cm^2/Vs)	$\mu_{LP,h}$ (cm^2/Vs)	$\sum\mu$ (cm^2/Vs)	Experiment $\phi\sum\mu$ (cm^2/Vs)
$MAPbI_3$	2.39	2.76	20.5	11.7	32.2	35[5]
$FAPbI_3$	2.57	2.85	17.1	11.4	28.5	27[6]
$FAPbBr_3$	3.37	3.61	7.0	5.3	12.3	14[6]
$FA_{0.83}Cs_{0.17}PbI_3$	2.25	2.49	23.5	15.9	39.4	40[7]
$FA_{0.83}Cs_{0.17}PbBr_3$	3.54	3.78	6.0	4.6	10.6	10[7]

Table 3. Calculated coupling constants, RT mobilities, and experimental data in lead mixed-halides.[7]

Material	α_e	α_h	$(\mu_{LP,e}^{-1}+\mu_{AL,e}^{-1})^{-1}$ (cm^2/Vs)	$(\mu_{LP,h}^{-1}+\mu_{AL,h}^{-1})^{-1}$ (cm^2/Vs)	$\sum\mu$ (cm^2/Vs)	Experiment $\phi\sum\mu$ (cm^2/Vs)
$FA_{0.83}Cs_{0.17}Pb(I_{0.7}Br_{0.3})_3$	2.41	2.68	16.6	10.8	27.4	24[7]
$FA_{0.83}Cs_{0.17}Pb(I_{0.6}Br_{0.4})_3$	2.68	3.05	10.6	6.1	16.7	19[7]
$FA_{0.83}Cs_{0.17}Pb(I_{0.5}Br_{0.5})_3$	2.68	3.05	10.5	6.1	16.6	15[7]
$FA_{0.83}Cs_{0.17}Pb(I_{0.4}Br_{0.6})_3$	3.05	3.26	6.2	4.8	11.0	13[7]
$FA_{0.83}Cs_{0.17}Pb(I_{0.3}Br_{0.7})_3$	3.05	3.26	6.5	4.8	11.3	12[7]

Table 4. Calculated polaron binding energies (E_P) and large polaron radii (L_P) in MHPs.

Material	$E_{P,e}$ (meV)	$E_{P,h}$ (meV)	$L_{P,e}$ (Å)	$L_{P,h}$ (Å)
Lead halide				
$MAPbI_3$	7.0	9.3	40.0	34.0
$FAPbI_3$	8.0	9.9	39.0	35.0
$FAPbBr_3$	19.8	22.8	26.0	24.0
$FA_{0.83}Cs_{0.17}PbI_3$	8.0	9.8	34.0	31.0
$FA_{0.83}Cs_{0.17}PbBr_3$	20.0	22.7	27.0	25.0
Lead mixed halide				
$FA_{0.83}Cs_{0.17}Pb(I_{0.7}Br_{0.3})_3$	8.0	9.9	36.0	33.0
$FA_{0.83}Cs_{0.17}Pb(I_{0.6}Br_{0.4})_3$	10.0	12.8	33.0	29.0
$FA_{0.83}Cs_{0.17}Pb(I_{0.5}Br_{0.5})_3$	10.0	12.8	33.0	29.0
$FA_{0.83}Cs_{0.17}Pb(I_{0.4}Br_{0.6})_3$	12.8	14.6	29.0	27.0
$FA_{0.83}Cs_{0.17}Pb(I_{0.3}Br_{0.7})_3$	12.8	14.6	29.0	27.0

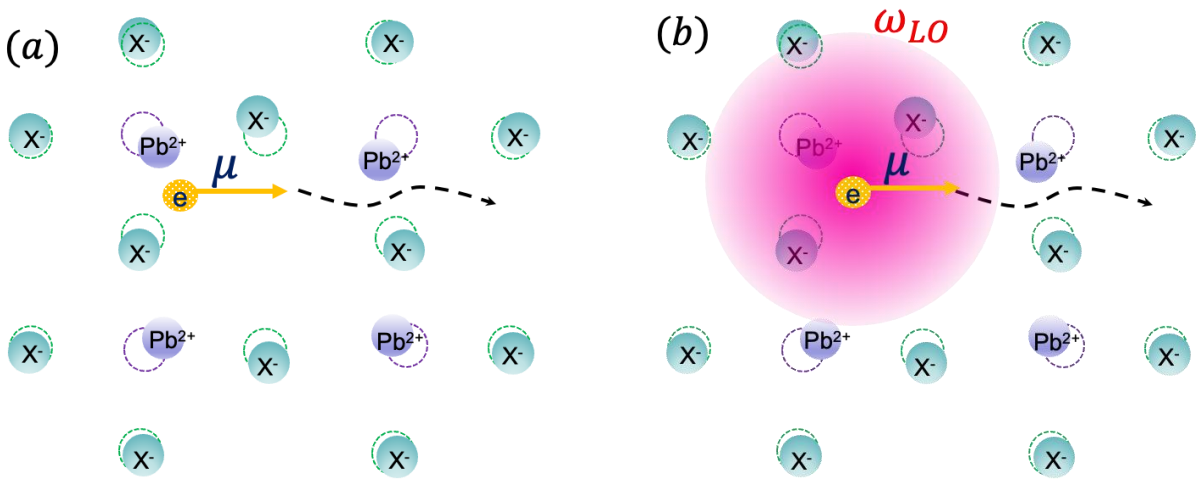

Figure 1. The large polaron transport model. (a) Ionic crystal polarization results from lattice distortion that occurs when an electron travels in a polar lattice and follows its path. (b) A large electron polaron is a dressed particle produced by an electron coupled with an LO phonon cloud created from self-induced polarization (pink circle), and the polaronic effect shows the defect tolerance attained through atomic screening.

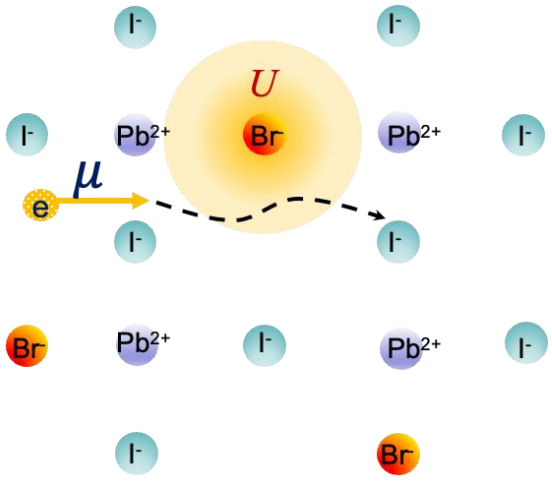

Figure 2. The alloy scattering model. The yellow circle represents the alloy scattering potential (*U*), which is the scattering source resulting from a random distribution of Br^- atoms in the initial I^- sites of lead mixed halides.

Synthesis of Graphene from Agricultural Waste for Electrodes in Capacitive Deionization Applications

Penpicha Poonpat[1], Teerayut Uwanno[1,*], Mayuree Phonyiem Reilly[1], Winadda Wongwiriyapan[1]
[1]*College of Materials Innovation and Technology, King Mongkut's Institute of Technology Ladkrabang*
[*]*E-mail: teerayut.uw@kmitl.ac.th*

Abstract:

In this study, reduced graphene oxide was synthesized from sugarcane bagasse (SB) to use as electrodes in capacitive deionization. SB was converted to biochar by dehydration reaction with concentrated H_2SO_4. Then biochar was converted to graphene oxide (GO) by H_3PO_4-assisted Hummers' method. Finally, GO was reduced by ascorbic acid solution, giving reduced graphene oxide (rGO). Fourier-transform infrared (FTIR) spectrum of biochar compared to SB showed decrease in peak intensity at 1033 cm^{-1} (C-O stretching) and 3350 cm^{-1} (O-H stretching) and increase in peak intensity at 1423 cm^{-1} (C-C stretching) and 1597 cm^{-1} (C=C stretching), suggesting the conversion of lignocellulose into graphitic structure. This agrees with Raman spectra which showed D band at around 1340 cm^{-1} and G band at around 1580 cm^{-1} which belong to graphitic carbon. For GO, FTIR spectrum showed increase in peak intensity at 1032-1080 cm^{-1} (C-O stretching) and 1189 cm^{-1} (C-H wagging), suggesting the oxidation of biochar and the presence of functional groups with O and H. On the other hand, FTIR spectrum for rGO showed the opposite change, suggesting the reduction of GO and partial removal of functional groups with O and H from GO. These suggest that SB was successfully converted to rGO.

1. Introduction

Capacitive deionization (CDI) has received increasing interest as a solution for freshwater shortage because of its low energy requirement and lower cost compared to other methods. In CDI technique, two electrodes are oppositely biased so that Na^+ and Cl^- ions are moved to each electrode by Coulomb force and then absorb at surface of electrodes. Carbon materials are considered as one of the promising candidates for electrodes in CDI because of their large surface area, high conductivity and high chemical stability, but CDI performance may be limited by their hydrophobicity. In this study, reduced graphene oxide (rGO) is focused on because its hydrophilic surface, in addition to large surface area and low electrical resistance. It is expected to give increased salt absorption capacity compared to other type of carbon electrodes.[1-4] Conventionally, rGO is synthesized by reducing graphene oxide (GO) obtained from Hummers' method, using graphite as starting material. In this study we used biochar derived from sugarcane bagasse (SB) through dehydration reaction with concentrated H_2SO_4, as starting material for Hummers' method because this can lower the cost and can offer a possibility for up cycling agricultural waste.

In this study, during biochar synthesis, the weight-to-volume ratio between SB and concentrated H_2SO_4 were varied. The obtained biochar was then oxidized into graphene oxide by improved Hummer's method[5] and then reduced by ascorbic acid solution. The physicochemical properties of the product from each step were investigated by Fourier transform infrared spectroscopy (FTIR) and Raman spectroscopy.

2. Materials and Methods

2.1 Materials

Sugarcane bagasse was obtained from Kaset Phol sugar Ltd., Udon Thani, Thailand. H_2SO_4 96% (Carlo Erba reagents), H_3PO_4 85% (Merck) $KMnO_4$ (Carlo Erba reagents), H_2O_2 40% (Carlo Erba reagents), HCl 37% (Qrec), Ascorbic acid (Carlo Erba reagents) and NH_3 solution 25% (Qrec) were used in biochar, GO and rGO synthesis. N- methyl-pyrrolidone (Qrec), Polyvinylidene fluoride (MTI) were used in CDI electrode fabrication.

2.2 Methods

SB was washed by deionized water (DI water) and dried in sunlight. After that it was

ground into powder and was heated in oven at 80ºC for 12 hours to drive away remaining moisture. Then the powder was sieved through 250 mesh to obtain fine powder.

In dehydration process, 2 g, 2.5 g, 3 g, and 3.5 g of SB were separately mixed with 10 mL of concentrated H_2SO_4 for 10 minutes (Hereafter referred to as B2.0, B2.5, B3.0, B3.5, respectively). After reaction was finished, the obtained biochar was washed by DI water and filtered by vacuum.

For improved Hummers' process, 1 g of biochar was added into a mixture consisting of 54 mL of concentrated H_2SO_4 and 6 mL of H_3PO_4 (80%) in ice bath. Then 3.5 g of $KMnO_4$ was slowly added while stirring. The slurry was then stirred at 35 °C for 3 hours. After that 46 mL of DI water was added and stirred for 15 minutes. Then 100 mL of DI water is added and the reaction was terminated by adding a small amount of H_2O_2. The slurry was mixed with 5% HCl solution and then washed by DI water and filtered by vacuum to obtain the powder (denoted as GO).

For reduction of GO, GO powder was added into NH_3 solution where pH of 10 was maintained. Then 1 g of ascorbic acid was added to reduce GO. Lastly, the product was dried at 50 °C for 24 hours in oven (denoted as rGO).

CDI electrodes were fabricated by mixing commercial rGO with carbon black, N- methyl-pyrrolidone (NMP) and Polyvinylidene fluoride (PVDF). The mixture was then coated on Cu sheet. CDI electrodes were attached to current collector (Ti sheet), as shown figure 1. NaCl solution was fed through peristatic pump and conductivity of solution was measured at out flow. During CDI, applied electrical bias was varied and initial concentration of NaCl solution was 100 mg/L.

2.3 Characterization

SB, biochar from each condition, GO and rGO were characterized by Fourier transform infrared spectroscopy (FTIR) and Raman spectroscopy using 532 nm laser for excitation. In CDI, the concentration of NaCl solution was measured by conductivity meter. Conductivity of NaCl solution with known concentrations was first measured, in order to create detection line, to be used in NaCl concentration monitoring during CDI. Electrosorption capacity for each applied electrical bias was calculated from

$$\frac{C_0 - C_t}{m} V$$

Here, C_0, C_t are initial and final NaCl concentration, respectively. V is volume of solution and m is mass of electrodes.

3. Results and Discussion

3.1 Biochar Synthesis by Dehydration

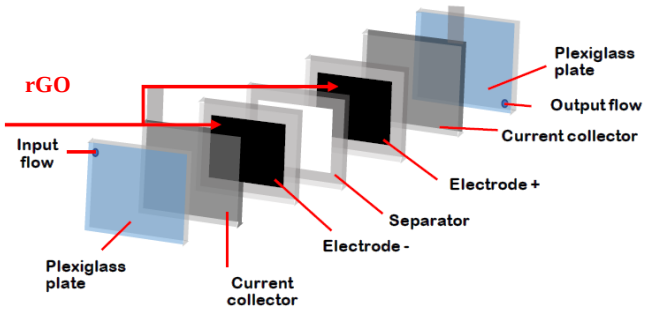

Figure 1 Schematic of CDI cell.

Conditions Sugarcane bagasse (g) : H_2SO_4 (ml)	0s	10s	20s	30s	60s	120s	% yield
2.0:10 (B2.0)		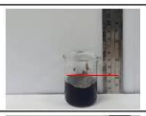		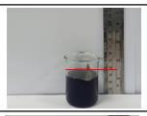	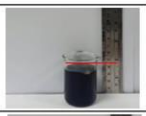	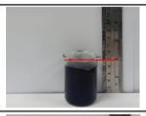	51.1 - 52.1
2.5:10 (B2.5)							53.9 - 54.5
3.0:10 (B3.0)	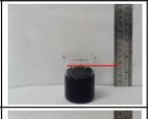						51.6 - 55.4
3.5:10 (B3.5)							55.3 - 55.9

Figure 2 Dehydration reaction of SB and product yield for each SB: H_2SO_4 condition.

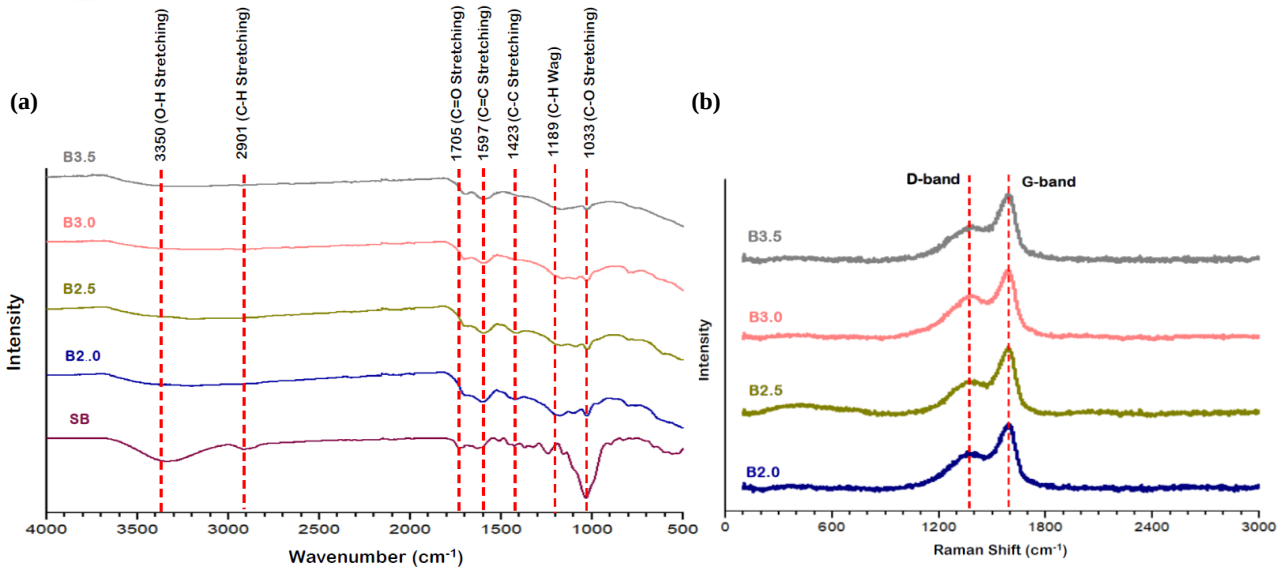

Figure 3 (a) FTIR spectra of SB and biochar from each SB: H_2SO_4 condition. (b) Raman spectra of biochar from each SB: H_2SO_4 condition.

Figure 2 shows the dehydration reaction and product yield which is fraction of weight of obtained biochar compared to weight of sugarcane bagasse used in reaction for each ratio between SB and concentrated H_2SO_4. It can be seen that all conditions underwent complete reaction and B3.5 gave highest product yield for BC. FTIR spectra for SB and biochar obtained from each condition are shown in figure 3 (a). It can be seen that spectra of all biochar showed decrease in peak intensity at 1033 cm^{-1} (C-O stretching) and 3350 cm^{-1} (O-H stretching) and increase in peak intensity at 1423 cm^{-1} (C-C stretching) and 1597 cm^{-1} (C=C stretching), compared to SB, suggesting that lignocellulose was converted into graphitic structure through dehydration reaction with concentrated H_2SO_4. Figure 3 (b) shows Raman spectra for biochar obtained from each condition. All conditions show D band at around 1340 cm^{-1} and G band at around 1580 cm^{-1} which belong to graphitic carbon, in agreement with FTIR spectra. B3.5 shows highest ratio between intensity of G band to D band (I_G/I_D), in addition to highest product yield. Therefore, biochar obtained from this condition was selected as starting material for GO and rGO synthesis.

3.2 GO and rGO synthesis

Figure 4 shows FTIR and Raman spectra of BC, GO and rGO obtained from B3.5 condition. FTIR spectrum of GO shows increase in peak

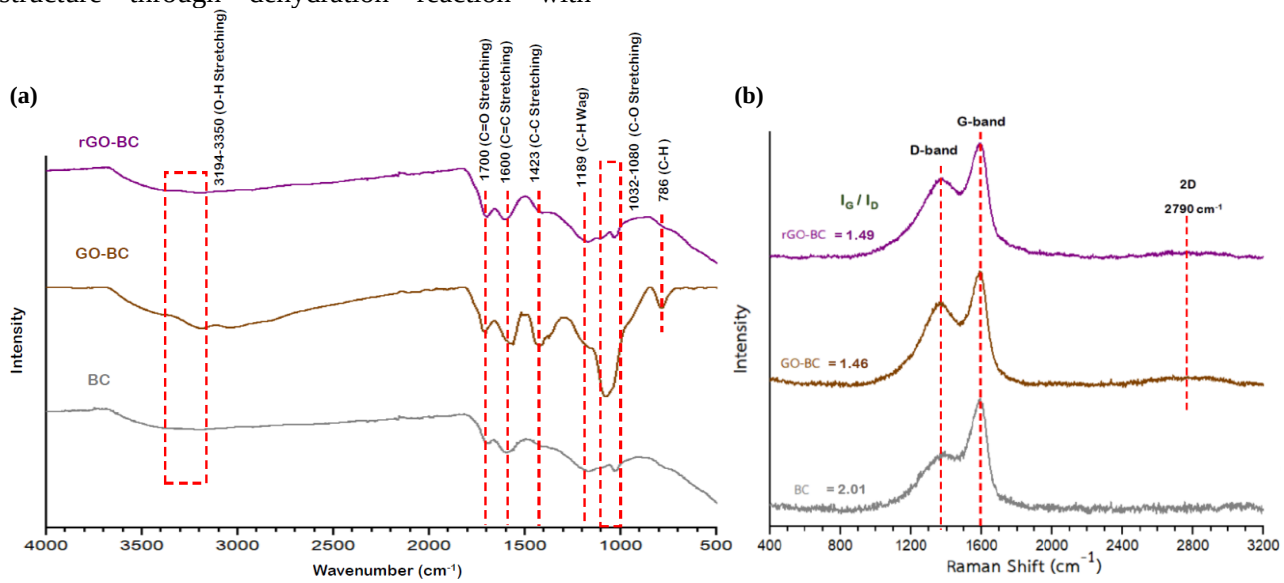

Figure 4 (a) FTIR spectra of BC, GO and rGO. (b) Raman spectra of of BC, GO and rGO

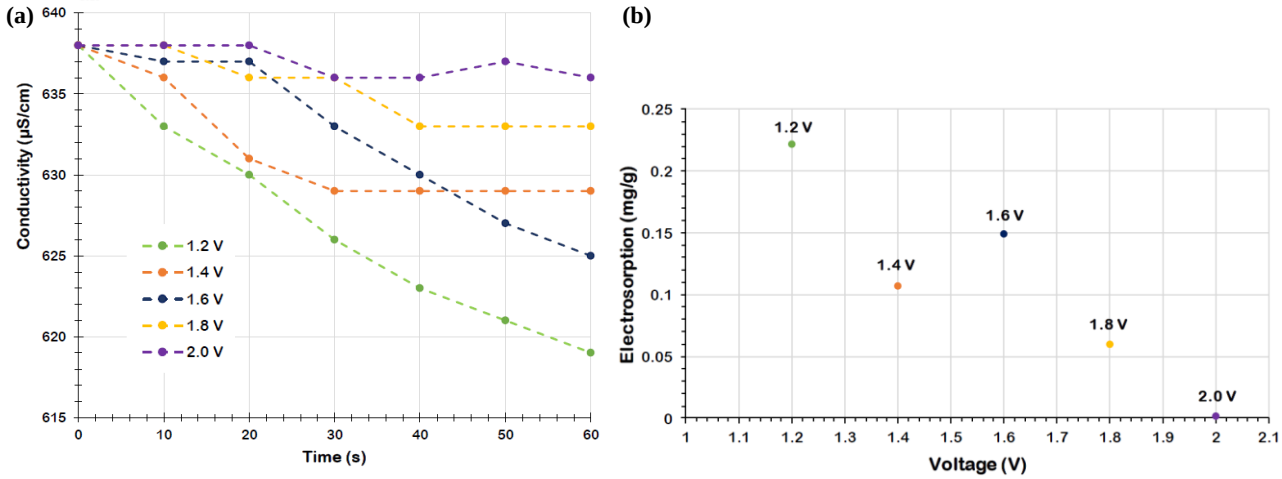

Figure 5 CDI (a) Conductivity of NaCl solution during CDI operation for each applied electrical bias. (b) Electrosorption capacity for each applied electrical bias.

intensity at 1032-1080 cm^{-1} (C-O stretching) and 1189 cm^{-1} (C-H wagging), compared to BC, suggesting the oxidation of BC and the presence of functional groups with O and H. Raman spectrum of GO shows increase in D band intensity compared to G band, resulting in smaller I_G/I_D, suggesting increase in number of defects, which could be the result of oxidation. For rGO, FTIR spectrum shows decrease in peak intensity at 1032-1080 cm^{-1} (C-O stretching) and 1189 cm^{-1} (C-H wagging) compared to GO, suggesting the reduction of GO and partial removal of functional groups with O and H from GO. Raman spectrum of rGO shows no significant change in D band intensity compared to G band. This could be because the removed functional groups with O and H from GO did not recover hexagonal structure of graphene honeycomb, only left defect sites in the structure. Also, in GO and rGO very broad Raman peak around 2790 cm^{-1} was observed. This resembles 2D band of graphene, implying the increase in periodicity of structure.

3.3 Capacitive Deionization

Figure 5 (a) shows change in conductivity during CDI. Bias of 1.2 V showed the largest decrease in conductivity, compared to other larger bias. This could be because of contribution from electrolysis of water or electrochemical reaction with Cu sheet at higher bias voltage, tampering with overall ion concentration. The electrosorption over operation time for 1.2 V was calculated to be 0.22 mg/g. Further improvement in stability over longer operation time is needed.

Conclusion

SB was successfully converted into biochar through dehydration reaction with concentrated H_2SO_4, as seen from FTIR spectra where peak intensity of C-O stretching and O-H stretching was decreased, but peak intensity of C-C stretching and C=C stretching increased. D band and g band of graphitic carbon was observed in Raman spectrum, indicating carbonization of SB. Weight-to-volume ratio between SB and concentrated H_2SO_4 of 3.5 g: 10 mL gave the highest product yield and highest I_G/I_D. GO was successfully synthesized from biochar, as shown by FTIR spectrum where peak intensity of C-O stretching and C-H wagging increased and by Raman spectrum where I_G/I_D decreased. GO was reduced in rGO as shown by FTIR spectrum where peak intensity of C-O stretching and C-H wagging decreased. CDI operation using rGO as electrode was confirmed, with electrical bias of 1.2 V giving highest electrosorption capacity compared to other voltages.

Acknowledgements

This research was partially supported by academic promotion grant 2023 from KRIS (Grant No. 2566-02-09-004), KMITL and Fundamental fund 2024 from TSRI.

References

1. Wang, G.; Qian, B.; Dong, Q.; Yang, J.; Zhao, A.; Qiu, J., Highly Mesoporous Activated Carbon Electrode for Capacitive Deionization. *Sep. Purif. Technol.* **2013,** *103*, 216-221.
2. Wang. Y.; Zhang, L.;Wu, Y.; Xu, S.; Wang, J. Polypyrrole/carbon nanotube composites as cathode material for performance enhancing of

capacitive deionization technology . *Desalination* **2014,** *354*, 62-67.
3. Xu, X.; Liu, Y.; Lu, T.; Sun, Z.; Chua, D. H. C., Pan, L. Rational design and fabrication of graphene/carbon nanotubes hybrid sponge for high-performance capacitive deionization. *J Mater. Chem. A* **2015,** *3*, 13418-13425.
4. Luo, G.; Wang, Y.; Gao, L.; Zhang, D.; Lin, T. Graphene bonded carbon nanofiber aerogels with high capacitive deionization capability. *Electrochemica Acta* **2018,** *260*, 656-663.
5. Marcano, D. C.; Kosynkin, D. V.; Berlin, J. M.; Sinitskii, A.; Sun, Z.; Slesarev, A.; Alemany, L. B.; Lu, W.; Tour, J. M., Improved Synthesis of Graphene Oxide. *ACS Nano* **2010,** *4*, 4806-4814.

Synthesis and Characterization of Mixed-Metal Azolate Frameworks via Post-Synthetic Process

Natchaya Phongsuk[1], Yollada Inchongkol[1], and Sareeya Bureekaew[1*]
[1]*School of Energy Science and Engineering, VidyasirimedhiInstitute of Science and Technology, Rayong 21210, Thailand.*
**Corresponding Author's E-mail: sareeya.b@vistec.ac.th*

Abstract:
A mixed-metal approach is a useful strategy for achieving a variety of desired properties or functionalities in metal-organic frameworks (MOFs) that may not be available in a single-metal system. This method involves incorporating two or more different metal ions into the framework structure. In this study, we synthesized mixed-metal azolate frameworks and conducted a comparative analysis of their properties in relation to those of single-metal MOFs. Mixed-metal Cu/Ni-triazole was obtained through a post-synthetic metal-exchange reaction, preserving the structure and morphology of the original Cu-triazole framework.

1. Introduction

Metal-organic frameworks (MOFs) are a class of crystalline porous materials that constructed from metal ions or cluster coordinated with organic ligand. This material has attracted much attention owing to their high surface area, tunable pore size, and rational design. MOFs are being extensively explored as potential materials for various applications, including gas storage[1] and separation[2], drug delivery[3], chemical sensors[4], and catalysis[5]. Various synthetic approaches have been employed to achieve specific properties for particular applications. One interesting approach is the use of mixed-metal MOFs, which incorporates two or more different metal ions into their structure, providing options for multifunctionality and tailoring material properties to a given application. In many cases, due to the synergistic effects derived from the presence of multiple metals, mixed-metal MOFs demonstrate superior performance across a wide array of applications compared to their single-metal counterparts[6,7]. Mixed-metal MOFs can be obtained through either one-pot synthesis or post-synthesis modifications. In this study, post-synthetic metal exchange process was employed. This method has been often used when the metals possess significantly reactivity in the formation for framework resulting in the difficulty in the direct one-pot synthesis. In metal exchange process, the parent MOF is added to a system with the presence of the second metal solution and then allows the exchange proceed.
$[M_3(trz)(\mu_3\text{-}OH)]X_2{\cdot}6H_2O$ (M= Cu or Ni, X = Cl and trz = triazolate), namely M-trz, represents an intriguing MOF with numerous potential applications[8,9]. The three-dimensional framework of M-trz is constructed by secondary building unit (SBU) of $M_3(trz)_3(\mu_3\text{-}OH)$, formed by three triazole linkers coordinated with three metal ions in a triangular arrangement. These metal ions within the unit are interconnected by an oxygen atom positioned at the center of the triangle, as shown in Figure 1. The framework can be constructed from either Cu or Ni metals, resulting in Cu-trz and Ni-trz, respectively. Even though they share the same structure, their properties are distinctive depending on the metal center. Cu-MOF, facilely obtained by mixing of $CuCl_2$ and trz in DI-water at room temperature, demonstrates poor thermal stability[10]. The framework collapses at approximately 225°C, as indicated by thermogravimetric analysis (TGA) results. On the other hand, Ni-trz displays much higher thermal stability (up to 400 °C). Its robustness is beneficial for various applications, especially catalysis. However, its synthesis involves complex procedures, including the use of hazardous hydrofluoric acid (HF), under high synthetic temperatures (200°C), for 48 hours. This limitation hinders the scale-up process to realize practical applications[11].

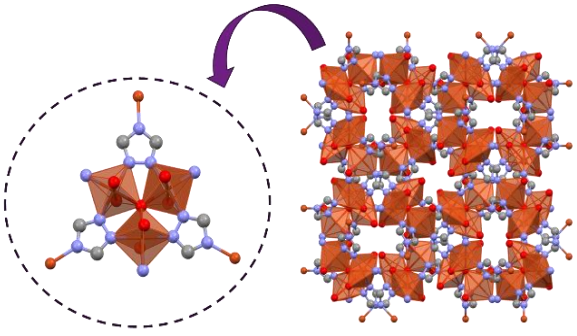

Figure 1. Triangular metal cluster and M-trz framework

In this study, we successfully obtained a mixed metal framework, Cu/Ni-trz, through the metal exchange process. Cu ions in the parent Cu-trz framework were partially replaced by Ni ions using the microwave-assisted hydrothermal method. The structural integrity and morphology of the resulting mixed metal framework were maintained. Additionally, the thermal stability of the framework increased by 15°C after the incorporation of Ni ions in the structure, opening up opportunities for further applications[12, 13].

2. Materials and Methods

2.1 Materials

Copper chloride dihydrate ($CuCl_2 \cdot 2H_2O$, Supelco, ≥ 99.0%), 1,2,4-triazole (TCI, > 99.0%), Nickle chloride hexahydrate ($NiCl_2 \cdot 6H_2O$, Supelco ≥ 98.0%), Nickle sulfate hexahydrate ($NiSO_4 \cdot 6H_2O$, Sigma-Aldrich, ≥ 98.0%), Nickle nitrate hexahydrate ($Ni(NO_3)_2 \cdot 6H_2O$, Sigma-Aldrich, ≥ 97.0%) were used without further purification.

2.2 Synthesis

Preparation of Cu-trz

Cu-trz was synthesized following the previously reported protocol[10]. In general, 1,2,4-triazole (0.14 g, 2 mmol) was dissolved in 10 ml deionized water. Then, the solution was added into 50 ml of $CuCl_2 \cdot 2H_2O$ solution (0.34 g, 2 mmol) at room temperature under stirring 30 m, obtaining the blue powder product.

Preparation of Cu/Ni-trz

Cu/Ni-trz was synthesized by post-synthetic metal exchange process. The powder of synthesized Cu-trz (100 mg) was added to Ni salt solutions (4 mmol in 10 ml). The resulting mixture was heated using microwave radiation (CEM Discovery). Subsequently, the product was washed multiple times with deionized water (DI) and dried at 50°C for 24 hours in a vacuum oven.

The names of each sample indicated in this study correspond to post-synthesis condition. For instance, Cu/$NiCl_2$-trz 200°C 30m refers to Cu-trz with post-synthesis Ni exchange using $NiCl_2$ as a Ni salt at 200°C for 30 min.

2.3 Characterization

Crystalline phase identification was performed using powder X-ray diffractometer (PXRD, Bruker, New D8 advance, Cu Kα, λ = 1.5406 Å). Product morphology and element analysis were examined by a field-emission scanning electron microscope (FE-SEM, JEOL, JSM-7610F) equipped with energy dispersive spectroscopy (EDS, Oxford X-max 150 mm^2) operating in a gentle beam mode (0.5-2.0 kV). Particle sizes of the obtained samples were calculated by ImageJ software. Before measurement, the samples were spluttered with platinum at 10 mA for 60 sec to increase the surface conductivity. Thermogravimetric analysis (TGA) measurements were performed on Rigaku thermal plus evo2 (TG 8121) under nitrogen atmosphere with the flow rate of 200 $cm^3\ min^{-1}$ and the ramping rate of 5°C min^{-1}.

3. Results

3.1 XRD

Figure 2. shows the XRD patterns of as-synthesized Cu-trz and prepared Cu/Ni-trz samples. The peak pattern of Cu-trz is consistency with the simulated pattern according to the repoted data[10], confirming the successful synthesis of Cu-trz parent framework. Also, the XRD patterns of the mixed metal Cu/Ni-trz obtained through various methods match well with the characteristic peaks of Cu-trz, suggesting the stable MOF structure after modification. The incorporation of Ni into the framework does not disrupt the structure of the parent Cu-trz during the metal exchange process.

3.2 SEM and SEM/EDS

The morphologies of all samples were confirmed by SEM imges as shown in Figure 3a-h. As depicted, the Cu-trz displayed a regular hexagonal shape with an average size of approximately 336 ± 40 nm (Figure 3a.). After Ni substitution in the Cu framework, Cu/Ni-trz maintained a regular hexagonal shape with nearly identical particle sizes (Figure 3b-f.), except for Cu/$NiCl_2$-trz 200°C 30m

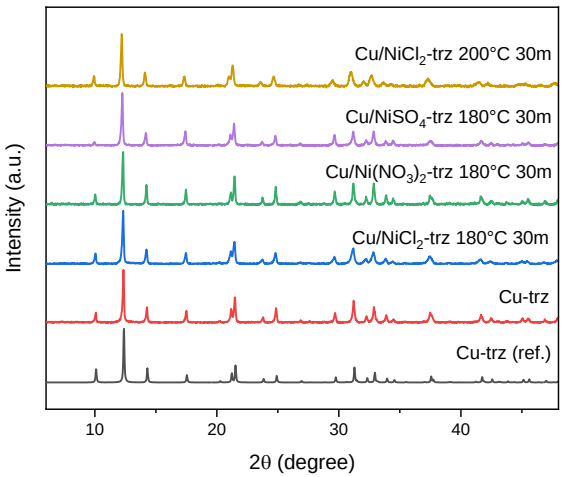

Figure 2. XRD patterns of MOFs.

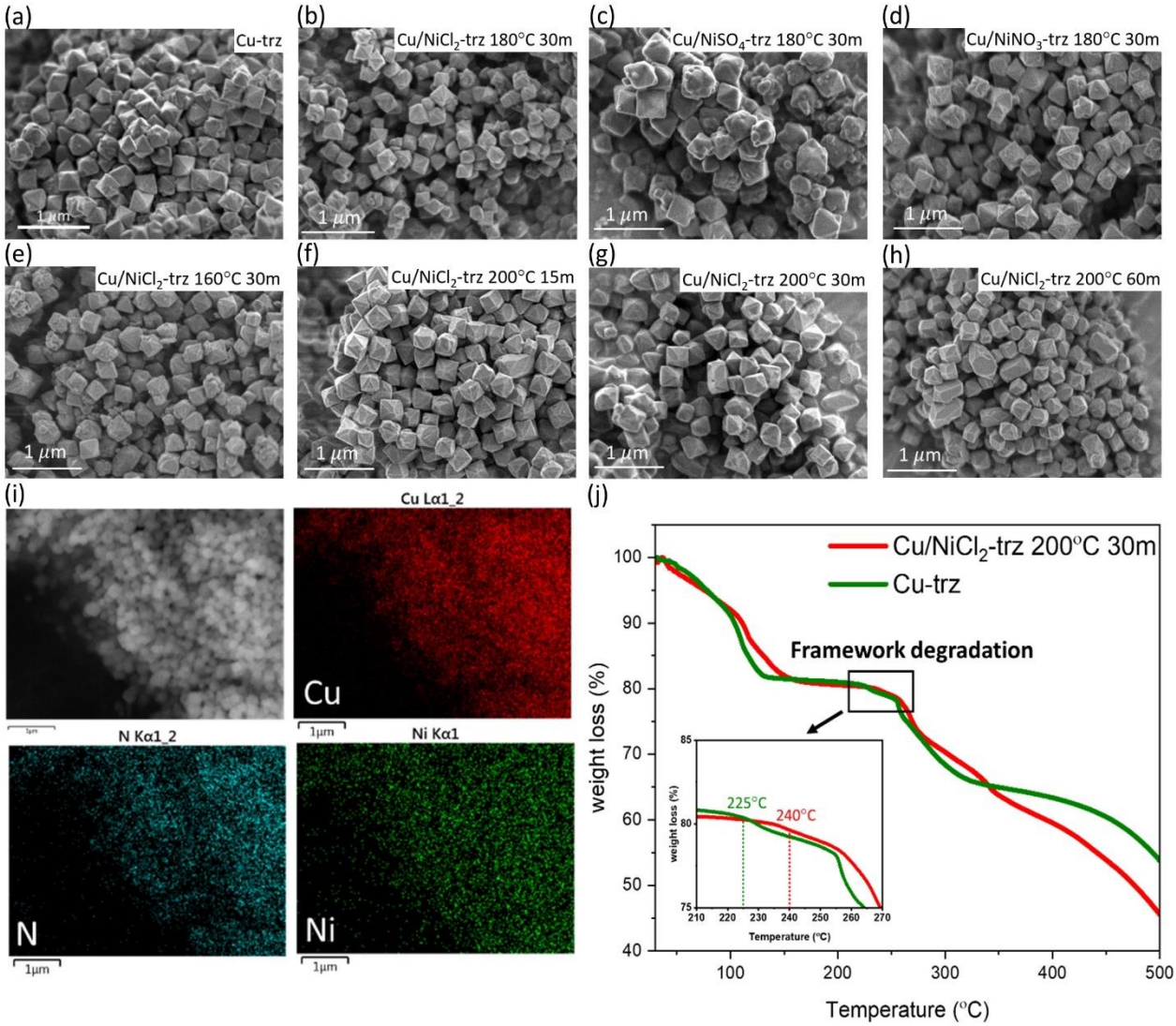

Figure 3. (a-h) SEM images of Cu-trz and Cu/Ni-trz by various metal exchange conditions, (i) SEM/EDS mappings of Cu/$NiCl_2$-trz 200°C 30m, and (j) TGA plots of MOFs at ramping rate of 5 °C min^{-1}

and 60m which showed a decrease in particle size to 258 ± 40 nm (Figure 3g-h.). The decrease of particle size can be ascribed to the dissolution-recrystallization process induced by the elevated reaction temperatures and prolonged reaction time during the process. The Ni and Cu metal contents in each sample were examined by SEM/EDS, and the results are summarized in Table 1. Varying the Ni salts, $NiCl_2$ (17.42 % atomic weight) substituted into the framework more effectively than $NiSO_4$ (11.11 % atomic weight) and $Ni(NO_3)_2$ (7.03 % atomic weight). This difference is probably due to the varying pH of the resulting solution. Consequently, $NiCl_2$ was selected as Ni salt for further optimization of synthetic conditions. The reaction temperature was subsequently adjusted, revealing that higher temperatures resulted in better substitution. Specifically, at 160, 180, and 200°C, the incorporation of Ni into the framework was 12.00, 17.42, and 22.68 % atomic weight, respectively. Finally, the reaction time was optimized using $NiCl_2$ and 200°C conditions. Reaction times of 15, 30 and 60 min produce the mixed metal framework with rather similar Ni contents of 20.58, 22.68, and 23.58 % atomic weight, respectively. It was found that the reaction time does not severely affect the substitution process of Ni. We further analyze the distribution of Ni in the mixed-metal framework. Figure 3i. reaveals the homogeneous distribution of Ni in the framework of Cu/$NiCl_2$-trz 200°C 30m. This suggests the homogeneous substitution of the Ni inside the framework for every mixed-metal samples.

Table 1 The metal content in Cu/Ni-trz MOFs with various parameters of metal exchange process

Parameter	Condition	Ni (% atomic weight)	Cu (% atomic weight)
Ni salts	$NiCl_2 \cdot 6H_2O^a$	17.42	82.58
	$NiSO_4 \cdot 6H_2O^a$	11.11	88.89
	$Ni(NO_3)_2 \cdot 6H_2O^a$	7.03	92.97
Temperature	$160°C^b$	12.00	88.00
	$180°C^b$	17.42	82.58
	$200°C^b$	22.68	77.32
Time	$15m^c$	20.58	79.42
	$30m^c$	22.68	77.32
	$60m^c$	23.58	76.42

Post-synthesis condition, a; 180°C for 30m, b; using $NiCl_2 \cdot 6H_2O$ as Ni salt for 30m, and c; using $NiCl_2 \cdot 6H_2O$ as Ni salt at 200°C

3.3 TGA

The thermal stability of the MOFs was determined through TGA, and the results are depicted in Figure 3j. Cu/$NiCl_2$-trz 200°C 30m was chosen as a representative of the mixed metal structure due to its high content of Ni ions. Below 100°C, a drop in the TGA profiles of both Cu-trz and Cu/Ni-trz was observed, attributed to the loss of water solvent, suggesting the porous structure of both frameworks. The facilely synthesized Cu-trz exhibited framework thermal degradation around 225°C. In contrast, the mixed metal Cu/$NiCl_2$-trz 200°C 30m displayed higher framework thermal stability, collapsing at approximately 240°C – 15°C more stable than Cu-trz. These results indicate that the substitution of Ni in the MOF can improve the thermal stability of a mixed-metal MOF.

Conclusion

This work demonstrates post-synthesis Ni exchange on Cu-trz using the microwave-assisted hydrothermal method. This process resulted in the formation of Cu/Ni-trz, which maintained its crystalline structure and exhibited a uniform distribution of Ni within the Cu/Ni-MOF. Importantly, the incorporation of Ni led to an enhancement in the thermal stability of the mixed-metal MOF. We anticipate that this achievement will pave the way for the utilization of the mixed-metal Cu/Ni-trz MOF in various applications.

Acknowledgements

This work was supported by VISTEC through the program of postdoctoral and PhD fellowships, by the Program Management Unit for Human Resources & Institutional Development, Research and Innovation (Grant No.B05F650042), by the National Research Council of Thailand (NRCT) grant no. N41A640100, and by the Toray Science Foundation (TSF), Japan.

References

1. Makal, T. A.; Li, J.-R.; Lu, W.; Zhou, H.-C., Methane storage in advanced porous materials. *Chemical Society Reviews* **2012,** *41* (23), 7761-7779.
2. Li, J.-R.; Sculley, J.; Zhou, H.-C., Metal–Organic Frameworks for Separations. *Chemical Reviews* **2012,** *112* (2), 869-932.
3. Lawson, H. D.; Walton, S. P.; Chan, C., Metal–Organic Frameworks for Drug Delivery: A Design Perspective. *ACS Applied Materials & Interfaces* **2021,** *13* (6), 7004-7020.
4. Kumar, P.; Deep, A.; Kim, K.-H., Metal organic frameworks for sensing applications. *TrAC Trends in Analytical Chemistry* **2015,** *73*, 39-53.
5. Yang, D.; Gates, B. C., Catalysis by Metal Organic Frameworks: Perspective and Suggestions for Future Research. *ACS Catalysis* **2019,** *9* (3), 1779-1798.
6. Dhakshinamoorthy, A.; Asiri, A. M.; Garcia, H., Mixed-metal or mixed-linker metal organic frameworks as heterogeneous catalysts. *Catalysis Science & Technology* **2016,** *6* (14), 5238-5261.
7. Abednatanzi, S.; Gohari Derakhshandeh, P.; Depauw, H.; Coudert, F.-X.; Vrielinck, H.; Van Der Voort, P.; Leus, K., Mixed-metal

metal–organic frameworks. *Chemical Society Reviews* **2019,** *48* (9), 2535-2565.

8. Ponchai, P.; Adpakpang, K.; Bureekaew, S., Selective cyclohexene oxidation to allylic compounds over a Cu-triazole framework via homolytic activation of hydrogen peroxide. Dalton Transactions 2021, 50 (23), 7917-7921.
9. Wang, J.; Liu, J.; Song, Y.; Geng, S.; Peng, Z.; Yu, J.; Liu, F.; Wang, Y.; Xi, S.; Zhang, Z.; Fan, Z., Simultaneous Defect and Size Control of Metal–Organic Framework Nanostructures for Highly Efficient Carbon Dioxide Electroreduction to Multicarbon Products. ACS Materials Letters 2023, 5 (8), 2121-2130.
10. Yamada, T.; Maruta, G.; Takeda, S., Reversible solid-state structural conversion between a three-dimensional network and a one-dimensional chain of Cu(ii) triazole coordination polymers in acidic/basic-suspensions or vapors. *Chemical Communications* **2011,** *47* (2), 653-655.
11. Ouellette, W.; Prosvirin, A. V.; Valeich, J.; Dunbar, K. R.; Zubieta, J., Hydrothermal Synthesis, Structural Chemistry, and Magnetic Properties of Materials of the MII/Triazolate/Anion Family, Where MII = Mn, Fe, and Ni. *Inorganic Chemistry* **2007,** *46* (22), 9067-9082.
12. Zhu, H.; Xue, W.; Huang, H.; Jiang, Z.; Zheng, M.; Zhong, C., Twisted pore aperture of MOF induced three-dimensional restricted sieving separation for CO_2 and C_2H_2 mixtures. Science Bulletin 2023, 68 (21), 2531-2535.
13. Gopi, S.; Al-Mohaimeed, A. M.; Al-onazi, W. A.; Soliman Elshikh, M.; Yun, K., Metal organic framework-derived Ni-Cu bimetallic electrocatalyst for efficient oxygen evolution reaction. Journal of King Saud University - Science 2021, 33 (3), 101379.

Tailoring Structural and Electrochemical Properties by Metal-Ion Tuning of Ni/V Layered Double Hydroxide

Farman Ali[1], Manopat Depijan[1], Pasit Pakawatpanurut[1,*]

[1] *Department of Chemistry, Center of Sustainable Energy and Green Materials, and Center of Excellence for Innovation in Chemistry, Faculty of Science, Mahidol University, Rama VI Road, Bangkok 10400, Thailand*

*Corresponding Author's E-mail: *pasit.pk@gmail.com*

Abstract:
Recently, transition metals layered double hydroxides (LDHs) have been widely used for energy storage applications because of their two-dimensional layered structure, environmentally friendly nature, cost-effectiveness, and excellent electrochemical performance. However, their property of structural tunability by varying metal ion ratios still needs to be explored to investigate the effect on physicochemical and electrochemical properties. Herein, different molar ratios of Ni:V=5:1, 3:1, 1:1, 1:3, and 1:5 were synthesized using hydrothermal process. Ni:V=1:1 showed the highest areal capacitance of 4451 mF cm^{-2} at current density of 4 mA cm^{-2}. Among the Ni- and V-dominant ratios, Ni:V=5:1 showed the highest areal capacitance of 3317 mF cm^{-2} while Ni:V=1:3 showed areal capacitance of 2034 mF cm^{-2}. The cycling stability test confirmed that Ni:V=3:1 and 1:5 showed high capacitance retention of 102% and 56% after 1000 cycles at current density of 15 mA cm^{-2}. Increasing the Ni ratio in LDH induced higher degree of structural arrangements without hydroxyl group defects resulting in better electrochemical performance in the form of areal capacitance and cycling stability. An increase in V-metal increased the rate performance and showed higher conductivity. Based on the results of varying molar ratios, it was inferred that Ni:V=5:1 and 1:5 were the best-optimized ratios.

1. Introduction

Sustainable, clean, and non-conventional energy storage systems, predominantly batteries and supercapacitors, store energy from renewable energy resources and supply energy to remote areas.[1] For the development of sophisticated and miniaturized supercapacitors and batteries, and to achieve high energy and power densities, the choice of efficient electrode materials has been a topic of interest. Transition metal layered double hydroxides (LDHs) have attained considerable attention for commercial energy storage devices.[2] LDH compounds have the generic formula $[M^{II}_{1-x} M^{III}_{x} (OH)_2]^{x} (A^{n-})_{x/n} \cdot yH_2O]$, where M^{II} is a divalent metal ion (e.g., Fe^{2+}, Ni^{2+}, and Zn^{2+}) and M^{III} is a trivalent metal ion (e.g., V^{3+}, Ga^{3+}, Mn^{3+}, and Al^{3+}). A^{n-} represents interlayer anionic species, such as CO_3^{2-}, SO_4^{2-}, NO_3^{-}, OH^{-}, Cl^{-}, and F^{-}, that exist with neutral H_2O molecules via hydrogen bonding inside the lamellae.[3] LDH materials show a unique brucite-like lamellar structure with high capacitance, large surface area, fast redox reactions during charging and discharging, environmental friendliness, and cost-effectiveness.[4] Some of the works have been reported related to the synthesis of Ni/V LDH and their heterostructures. For instance, Wang's group synthesized petal-like Ni/V-S LDH with Ni as the dominant dopant.[5] Zhang et al. fabricated an in-situ Ni-V LDH/rGO heterostructure with Ni^{2+} as the dominant dopant, finding the optimal Ni:V ratio to be 4:1 for heterostructure synthesis with rGO.[6] Tu et al., fabricated the heterostructure of Ni:V=2:1 with CNTs using the reflux method for advanced asymmetric supercapacitors. Tu et al. reported the synthesis of Ni/V LDH using a hydrothermal process to fabricate heterostructures with V_2CT_x MXene to enhance the electrochemical performance of supercapacitors Tu et al. synthesized Ni:V=2:1 heterostructures with CNTs via the reflux method for advanced asymmetric supercapacitors. Tu et al. also reported on synthesizing Ni/V LDH using a hydrothermal process, creating heterostructures with V_2CT_x MXene to enhance supercapacitor electrochemical performance.[7] Pan's group synthesized a Ni/V LDH heterostructure with ZIF-67 through an in-situ self-assembly process for applications in

photocatalysis and energy storage.[8] Despite successful synthesis of Ni/V LDH with Ni^{2+} as the dominant metal and high specific capacitances in numerous studies, the effect of Ni^{2+} and V^{3+} as dominant dopants and varying metal ion molar ratios on the structural and electrochemical properties of Ni/V LDHs remains unexplored. As a result, the main objective of this study was the structural tuning of Ni/V LDH by varying metal ion ratios for the investigation of molar ratios on their structural and electrochemical properties. Individual metals' unique redox behavior and electronic configurations will influence the physicochemical properties including *d*-spacing, crystal size, and layered morphology. This work provides an insight into the study of effect of Ni and V ratios affecting the structural and electrochemical properties.

To achieve this, a set of samples with molar ratios of was synthesized by a one-step hydrothermal process. Ni-dominant samples showed higher crystallinity compared to V-dominant LDHs owing to the hydroxyl group defects. Electrochemical results from cyclic voltammetry (CV), Galvanostatic charge-discharge (GCD), and electrochemical impedance spectroscopy (EIS) confirmed the effect of tuning of LDHs by metal ions on their electrochemical properties. Among the Ni- and V-dominant ratios, Ni:V=5:1 showed the highest areal capacitance of 3317 mF cm^{-2} while Ni:V=1:3 showed an areal capacitance of 2034 mF cm^{-2}. The cycling stability test confirmed that Ni:V=3:1 and 1:5 showed high capacitance retention of 102% and 56% after 1000 cycles at the current density of 15 mA cm^{-2}.

2. Materials and Methods

2.1 Materials

Nickle chloride ($NiCl_2$, 98%, Sigma-Aldrich), vanadium chloride (VCl_3, 97%, Sigma-Aldrich), potassium hydroxide (KOH, Sigma-Aldrich) pellets, poly(vinylidene fluoride) (PVDF, average MW=534000, Sigma-Aldrich), urea, (99%, Sigma-Aldrich), N-methyl-2-pyrrolidone (NMP, Acros Organics) and conductive carbon (Super P, TIMCAL).

2.2 Synthesis

A one-step hydrothermal process was used to synthesize Ni/V LDH nanosheets by keeping either metal ion as the dominant dopant.[9] In detail, for the molar ratios of Ni:V=5:1, 3:1, 1:1, 1:3, and 1:5, the amount of each ion was taken in such a way that the final molar ion concentration was retained at 2.4 mmol. In a typical process, x mmol of $NiCl_2$, and y mmol of VCl_3 were taken along with 0.25 g of urea in 40 ml of DI water and the reaction mixture was magnetically stirred for 1.0 h. Subsequently, the reaction mixture was transferred to a stainless-steel Teflon-lined autoclave vessel and the hydrothermal reaction was performed under sealed conditions at 120 °C for 12.0 h. After cooling to room temperature, the precipitates were collected and washed thrice and the product was dried in an oven at 70 °C for 12.0 h. The experimental setup is shown in Figure 1.

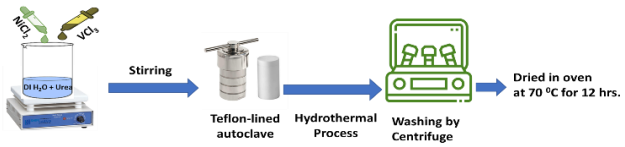

Figure 1. Schematic setup for the synthesis of Ni/V LDHs.

2.3 Characterization

The study of the crystal structure of the as-synthesized Ni/V LDH nanosheets was examined using powder X-ray diffraction (PXRD, D2-Phaser with Cu-Kα radiation, λ=0.154 nm). The surface functionality of the materials was studied using Fourier-transform infrared spectroscopy (FTIR, PerkinElmer 2000). The surface morphologies of the samples were examined using field-emission scanning electron microscopy (FE-SEM, HITACHI, SU-80410).

Electrochemical measurements of all LDH samples were performed using a three-electrode cell configuration in a 6 M KOH electrolyte. The working electrode was fabricated by mixing the active material, PVDF, and Super P conductive carbon in the mass ratio of 8:1:1, respectively. Then, the homogenous slurry was coated on a nickel foam current collector followed by hot pressing and dried in an oven at 80 °C for 12 h. Cyclic voltammetry analysis at a scan rate of 10 mV s^{-1}, galvanostatic charge-discharge (GCD) at different current densities (4 mA cm^{-2}, 6 mA cm^{-2}, 8 mA cm^{-2}, 10 mA cm^{-2}, 15 mA cm^{-2}), and electrochemical impedance spectroscopy (EIS) analysis in the frequency range of 0.01 Hz—100 kHz was performed. The areal capacitance (F cm^{-2}) was calculated according to the following Equation 1.

$$\text{Areal capacitnce} = I\,\Delta t / \Delta V S \qquad (1)$$

where I, $\Delta V \Delta t$, and S are the constant discharge current (A), the potential window (V), the discharge time (s), and the effective area (cm^2), respectively.

3. Results

3.1 Physicochemical Characterization

Figure 2a showed the XRD patterns of the as-synthesized LDH samples with different ratios of Ni:V=5:1, 3:1, 1:1, 1:3, and 1:5. The characteristic peaks located at about 11.5°, 23°, 33.5°, 38.5°, and 60° were most consistent with the distinctive features of carbonate-intercalated layered double hydroxide of Ni and V.[10] XRD pattern of Ni-dominant samples showed high-intensity peaks indicating high crystallinity compared to V-dominant samples. Ni:V=1:1, 3:1, and 5:1 showed large *d*-spacing values including 7.90, 7.82, and 7.74 Å, respectively,

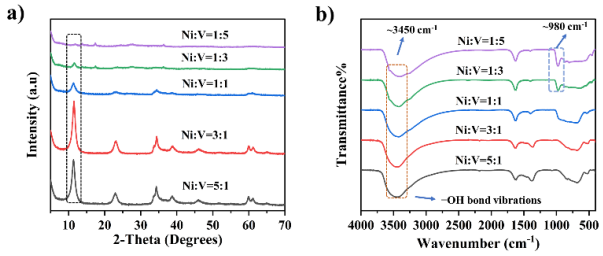

Figure 2. (a) XRD and (b) FTIR spectra of Ni:V=5:1, 3:1, 1:1, 1:3 and 1:5, respectively.

while Ni:V=1:3 and 1:5 showed lower *d*-spacing values of 7.57 and 7.42 Å, respectively as mentioned in Table 1.

Table 1. *d*-spacing and crystallinity values of all samples obtained from XRD data.

Samples	*d*-spacing d_{003} [Å]	Crystallinity [%]
Ni:V=5:1	7.74	67.8
Ni:V=3:1	7.82	73.8
Ni:V=1:1	7.90	60.1
Ni:V=1:3	7.57	59.8
Ni:V=1:5	7.42	39.7

The FTIR spectra in Figure 2b corresponded to Ni:V=5:1, 3:1, 1:1, 1:3, and 1:5 respectively. It can be observed that all the samples yielded similar IR spectra. The broad transmission bands at ~3450 cm^{-1} and 1650 cm^{-1} for all samples corresponded to the stretching vibrations of the –OH group of hydroxides present on the surface and inside the interlayers of compounds.[11] The transmission band at ~1380 cm^{-1} represented the absorption mode of the interlayer CO_3^{2-} ions.[12] However, for Ni:V=1:3 and 1:5 the shoulder bands at ~980 cm^{-1} were associated with the stretching vibrational mode of hydroxyl groups from water molecules coordinated with metal ions (Ni^{2+} and V^{3+}) that cause the defect resulting in low crystallinity of V-based LDHs. In the low-frequency region of 500–800 cm^{-1}, the transmission bands were related to M–O (Ni—O, V—O) bonds stretching vibrations.[13]

FE-SEM images revealed the surface morphology of Ni:V=5:1, 3:1, 1:1, 1:3, and 1:5. The SEM images are shown in Figures 3a, b, and c for Ni:V=5:1, 3:1, and 1:1 depicted the layered nanoflake structures, respectively.

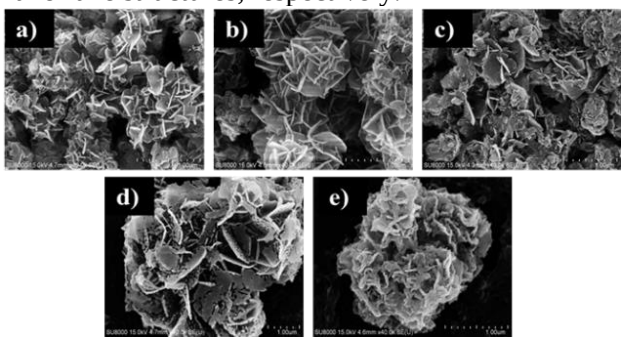

Figure 3. SEM images of (a) Ni:V=5:1 (b) 3:1, (c) 1:1, (d) 1:3, and (e) 1:5.

The SEM images of the Ni:V=1:3 and 1:5 showed accumulated porous and crumpled layered structures with broken edges, as shown in Figures 3d and e, respectively. From the SEM images, the high crystallinity of the Ni-based LDH compounds was more evident than that of the V-dominant compounds, which was also consistent with the XRD results.

3.2 Electrochemical characterization

Cyclic voltammetry (CV) was performed to investigate the electrochemical behavior of Ni:V=5:1, 3:1, 1:1, 1:3, and 1:5 LDH compounds. The CV profile of all samples (as shown in Figure 4a) indicated a redox pair at about 0.36 V and 0.15 V, corresponding to the undergoing redox reactions of Ni and V hydroxides present on the surface of Ni/V LDH. The proposed reversible redox reactions of Ni^{2+}/Ni^{3+}, V^{3+}/V^{4+}, or V^{4+}/V^{5+} are as follows.

$Ni(OH)_2 + OH^{-1} \rightleftharpoons NiOOH + H_2O + e^-$

$V(OH)_3 + OH^{-1} \rightleftharpoons VO(OH)_2 + H_2O + e^-$

$VO(OH)_2 + OH^{-1} \rightleftharpoons VO_2(OH) + H_2O + e^-$

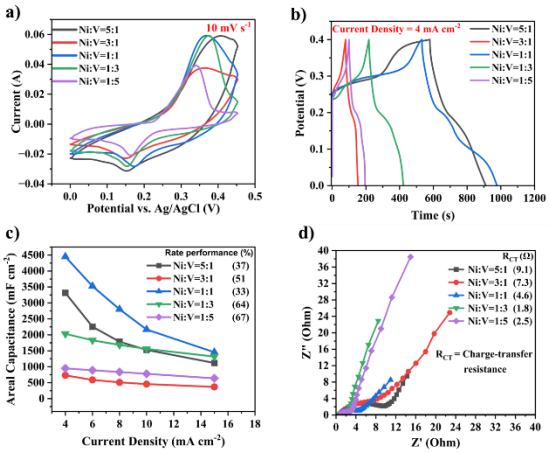

Figure 4. (a) CV and (b) GCD curves of the as-synthesized samples. (c) Capacitance versus current density plot and (d) Nyquist plot before stability test.

The areal capacitance at different current densities and rate performance were obtained from galvanostatic charge-discharge (GCD) analysis (as shown in Figure 4b) performed at different current densities. Ni:V=1:1 exhibited the highest areal capacitance of 4451 mF cm^{-2} at the current density of 4 mA cm^{-2} while for Ni:V=3:1 and 5:1, the areal capacitance values were calculated as 732.5 mF cm^{-2} and 3317 mF cm^{-2}, respectively. On the other hand, the areal capacitance values for Ni:V=1:3 and 1:5 were found to be 2033 mF cm^{-2} and 950.0 mF cm^{-2} respectively. Figure 4c shows areal capacitances versus current. densities of 4 mA cm^{-2}, 6 mA cm^{-2}, 8 mA cm^{-2}, 10 mA cm^{-2}, and 15 mA cm^{-2}. For Ni:V=1:1, the areal capacitance decreased sharply with increase in current densities, whereas for Ni:V=3:1 and 5:1 the decrease in areal capacitance was comparatively slow.

On the other hand, V-dominant samples showed a higher rate performance with the increase in current densities compared to Ni-dominant samples. The rate performance values for all the samples can be seen in Figure 4c. Nyquist plot of all the samples, as given in Figure 4d exhibited that all the samples showed semi-circles in a high-frequency range corresponding to their charge transfer resistance (R_{CT}). Ni:V=1:1, 3:1, and 5:1 showed R_{CT} values of 4.6 Ω, 7.3 Ω, and 9.1 Ω, respectively. Meanwhile, V-dominant samples Ni:V=1:3 and 1:5 exhibited low R_{CT} values of 1.8 Ω and 2.5 Ω, respectively.

Ni:V= 1:1, 1:3, and 1:5 showed poor capacitance retentions of 67%, 43%, and 56%, respectively, while Ni:V=3:1 and 5:1 sample highly retained their capacitances of 102% and 91%, respectively after 1000 cycles as shown in Figure 5a.

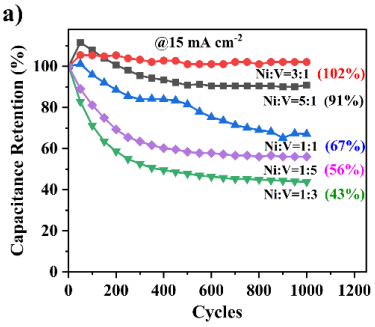

Figure 5. (a) Cycling stability performance of Ni:V=5:1, 3:1, 1:1, 1:3, and 1:5 for 1000 cycles at 15 mA cm^{-2}.

Conclusion

In summary, the structural tuning of Ni/V LDH was done by varying metal ions and LDH samples were successfully synthesized using a facile one-step hydrothermal process. FTIR results showed the presence of hydroxyl groups for V-dominant LDHs that caused low crystallinity as evident from XRD and SEM results. For electrochemical results, Ni:V=1:1 showed the highest areal capacitance of 4451 mF cm^{-2} at the current density of 4 mA cm^{-2}. For the case of Ni dominance, Ni:V=3:1 and 5:1 showed areal capacitance of 732.5 and 3317 mF cm^{-2}, respectively. For V-dominance, Ni:V=1:3 and 1:5 showed areal capacitance of 2034 mF cm^{-2} and 950.0 mF cm^{-2}, respectively. The cycling stability test confirmed that Ni:V=3:1 and 5:1 showed high capacitance retention of 102% and 91% after 1000 cycles at a current density of 15 mA cm^{-2} whereas, Ni:V=1:3 and 1:5 showed lower capacitance retention of 43% and 56%, respectively. Thus, increasing the Ni ratio in LDH induced a higher degree of structural arrangements without hydroxyl group defects resulting in better electrochemical performance in the form of areal capacitance and cycling stability. The increase in V content decreased the capacitance retention but increased the rate of performance and conductivity. Based on the electrochemical properties it was inferenced that Ni:V=5:1, showing high capacitance and cycling stability

performance, and Ni:V=1:5 with higher rate performance, and conductivity were the optimized ratios for further use in various applications. From our standpoint, Ni/V LDH material stands out as an exceptional electrode material, boasting superb structural and electrochemical properties. Nevertheless, to fully comprehend its performance variations across different Ni:V ratios, more in-depth mechanistic studies including comprehensive electronic structure calculations, charge distribution analyses, and spectroscopic investigations are warranted.

Acknowledgments

This work was supported by NSRF via the Program Management Unit for Human Resources and Institutional Development, Research, and Innovation (Grant Numbers B16F640099 and B37G660017), the Centre of Excellence for Innovation in Chemistry (PERCH-CIC), Ministry of Higher Education, Science, Research, and Innovation Thailand.

References

1. Hussain, F.; Rahman, M. Z.; Sivasengaran, A. N.; Hasanuzzaman, M., Energy storage technologies. In *Energy for Sustainable Development*, Elsevier: 2020; pp 125-165.
2. Caravaggio, G. A.; Detellier, C.; Wronski, Z. J. J. o. M. C., Synthesis, stability and electrochemical properties of NiAl and NiV layered double hydroxides. **2001,** *11* (3), 912-921.
3. Zhang, L.; Hui, K. N.; San Hui, K.; Lee, H. J. J. o. P. S., High-performance hybrid supercapacitor with 3D hierarchical porous flower-like layered double hydroxide grown on nickel foam as binder-free electrode. **2016,** *318*, 76-85.
4. Daud, M.; Kamal, M. S.; Shehzad, F.; Al-Harthi, M. A. J. C., Graphene/layered double hydroxides nanocomposites: a review of recent progress in synthesis and applications. **2016,** *104*, 241-252.
5. Liu, G.; Wang, G.; Guo, X.; Hao, X.; Wang, K.; Jin, Z. J. E. T., Facile Sulfuration Route to Enhance the Supercapacitor Performance of 3D Petal-like NiV-Layered Double Hydroxide. **2022,** *10* (11), 2200809.
6. Zhang, Q.; Xu, Y.; Li, C.; Chen, W.; Zhu, W.; Wang, L. J. J. o. A.; Compounds, Staggered nickel–vanadium layered double hydroxide nanosheets on reduced graphene oxide via in-situ growth for enhanced supercapacitor performance. **2023,** *935*, 168048.
7. Tu, Q.; Zhang, J.; Cai, S.; Zhang, K.; Zhan, H.; Huang, S.; Chen, L.; Sun, X. J. A. E. M., One-Step Preparation of NiV-LDH@ CNT Hierarchical Composite for Advanced Asymmetrical Supercapacitor. **2022,** *24* (9), 2101174.
8. Pan, J.; Li, S.; Zhang, L.; Li, F.; Yan, E.; Zhang, D. J. A. A. E. M., Rational Construction of ZnCo-ZIF-Derived ZnS@ CoS@ NiV-LDH/NF Binder-Free Electrodes Via Core–Shell Design for Supercapacitor Applications with Enhanced Rate Capability. **2022,** *5* (6), 6886-6895.
9. Wang, D.; Li, Q.; Han, C.; Lu, Q.; Xing, Z.; Yang, X. J. N. C., Atomic and electronic modulation of self-supported nickel-vanadium layered double hydroxide to accelerate water splitting kinetics. **2019,** *10* (1), 3899.
10. Tyagi, A.; Joshi, M. C.; Shah, A.; Thakur, V. K.; Gupta, R. K. J. A. o., Hydrothermally tailored three-dimensional Ni–V layered double hydroxide nanosheets as high-performance hybrid supercapacitor applications. **2019,** *4* (2), 3257-3267.
11. Hsieh, Z.-L.; Lin, M.-C.; Uan, J.-Y. J. J. o. M. C., Rapid direct growth of Li–Al layered double hydroxide (LDH) film on glass, silicon wafer and carbon cloth and characterization of LDH film on substrates. **2011,** *21* (6), 1880-1889.
12. Tyagi, A.; Joshi, M. C.; Shah, A.; Thakur, V. K.; Gupta, R. K., Hydrothermally Tailored Three-Dimensional Ni-V Layered Double Hydroxide Nanosheets as High-Performance Hybrid Supercapacitor Applications. *ACS Omega* **2019,** *4* (2), 3257-3267.
13. Qiu, Z.; Tai, C.-W.; Niklasson, G. A.; Edvinsson, T. J. E.; Science, E., Direct observation of active catalyst surface phases and the effect of dynamic self-optimization in NiFe-layered double hydroxides for alkaline water splitting. **2019,** *12* (2), 572-581.

The Study of Nanoparticle Composition in Sub-urban area

Yaowatat Boongla[1]*, Phuvasa Chanonmuang[2]
[1]*Sustainable Development Technology, Faculty of Science and Technology, Thammasat University, Rangsit Campus, Pathumtani, 12121, Thailand*
[2]*Expert Centre of Innovative Clean Energy and Environment, Research and Development Group for Sustainable Development, Thailand Institute of Scientific and Technological Research (TISTR), Klongluang, Pathumtani, 12120, Thailand*

**Corresponding Author's E-mail: yaowatat@tu.ac.th*

Abstract:

Thailand and other Asian countries are currently experiencing growing levels of air pollution. Particles or nanoparticles (NPs) in the atmosphere are an air pollutant that have a harmful impact on human health and the environment when exposed to excessive amounts. Lake information is obtained by examining the composition of particles or nanoparticles. Understanding suitable health risk and impact assessment for health risk assessment in acute and chronic effects, as well as including the source of NPs in ambient air, are examples. As a result, this study investigated the chemical composition of NPs ($PM_{0.1}$ and $PM_{0.1\text{-}0.5}$) in rainy season by setting up the NPs sampling for ambient air using cascade air sample for size-classified particle at the rooftop of building of the Robotic Innovation and Automatic Mechanical Center (INNOROBOT), Thailand Institute of Scientific and Technological Research (TISTR), Technotani, Klongluang, Pathumtani province. The samples were collected after 48 hours to determine concentration levels, organic carbon (OC), and elemental carbon (EC) in $PM_{0.1}$, $PM_{0.1\text{-}0.5}$ particle sizes. The average concentration of $PM_{0.1}$ was 9.57 µg/m^3, whereas $PM_{0.1\text{-}0.5}$ was 14.52 µg/m^3. This finding suggested that the average concentration of $PM_{0.1}$ was greater than 50% of the concentration of $PM_{0.1\text{-}0.5}$. When NPs are exposed for an extended period of time, it is probable that they will have a long-term effect on human health. The carbon composition revealed that the average concentration of OC was 0.67 µg/m^3, while the average concentration of EC was 0.36 µg/m^3, implying that OC was more concentrated than EC. As the composition result of NPs in this study, its emission source can be attributed to diesel exhaust and open biomass burning.

Keywords: Nanoparticle, Chemical Composition, Organic Carbon, Elemental Carbon

1. Introduction

Air pollution has been one of Asia's significant environmental issues in recent decades (Boongla et al., 2019; Tial, 2023; Phairuang et al., 2023). Air pollutants, particularly particulate matter (PM), are produced by both man-made and natural sources, including motor vehicles, households, the industrial sector, agricultural residue burning, and forest fires. Several studies have found that PMs have an impact on human health, urban and rural environments and global climate, either directly or indirectly. Recent studies of ambient PM have revealed that finer particles, particularly nanoparticles ($PM_{0.1}$), pose a risk to human health (Phairuang et al., 2022). Inhaled nanoparticles may cause lung inflammation and cardiac issues in the body. Breathing in diesel soot creates a general inflammatory response and changes the mechanism that regulates automatic activities in the cardiovascular system, such as heart rate control, according to human studies (Sonwani et al., 2021). High particle counts, high surface area to mass ratio, oxidative stress potential, high solubility and charge, and facile distal airway penetration characterize combustion particulates containing ultra-fines or $PM_{0.1}$ ($PM_{0.1}$ µm in diameter)(Xuan et al., 2023). South East Asia (SEA) has been a source of PM pollution in the recent decade, affecting countries both inside and outside the region (Boongla et al., 2019). Observations of PM in Thailand and neighboring countries currently is based on the level of coarse and fine particles (Ngoun et al., 2023; Dejchanchaiwong et al., 2020; Choomanee et al., 2020; Hien et al., 2019), and to a lesser extent on sub-micron particles ($PM_{1.0}$) (Tial et al., 2023; Amin et al., 2023; Vejpongsa et al., 2017) that are observed by both mathematical modeling and actual monitoring on the ground. However, data on the status and properties of ambient $PM_{0.1}$, as well as its sources, remains scarce. Furthermore, data on the carbon contents of size-specific particles in the small to nano-size range in Asian

countries and Thailand is currently lacking. Only a few studies on nanoparticles and their carbon components have been conducted in Asian countries and Thailand to better understand the levels of air pollution, origins, and effects of nanoparticles (Phairuang et al., 2022). Carbonaceous aerosols (CA) are produced by biomass, coal, and fossil combustion. Open biomass burning is the leading source of black carbon (BC) and organic carbon (OC) in the atmosphere. The term BC, which is roughly equivalent to elemental carbon (EC), is frequently used in climate models to refer to light-absorbing compounds. At the same time, the term EC is preferred in aerosol chemistry areas. CA levels vary according on the source, such as diesel exhaust, coal combustion, and biomass combustion. Furthermore, the features of ambient $PM_{0.1}$ and meteorological influence as a function of season have not been extensively investigated, particularly in Thailand's sub-urban areas.

Pathumtani province is a big city in Thailand, close to the Bangkok Metropolitan Region (BMR). It had a high population density and automobile density, as well as significant economic activity tied to a wide range of enterprises. Several studies, however, defined Pathumtani province as a BMR suburban. This city is quickly expanding, which, like other suburban regions in developing countries in Asia, may contribute to increased air pollution due to its proximity to air pollution emission sources, the objectives of this study were to (1) quantify nanoparticle concentrations; (2) determine the properties of size-fractionated particles bound EC and OC, as well as their correlation; and (3) identify the potential effect of meteorological and these pollutants in the study site. These linkages could help determine the influence of distribution emission.

2. Materials and Methods

2.1 Sampling site

Atmospheric PM was collected with a $PM_{0.1}$ cascade sampler at the rooftop of building of the Robotic Innovation and Automatic Mechanical Center (INNOROBOT), Thailand Institute of Scientific and Technological Research (TISTR), Technotani, Klongluang, Pathumtani province, located in Klong Ha, Klongluang, Pathumtani (Figure 1). The Robotic Innovation and Automatic Mechanical Center at the TISTR is located at 14.044744º (N) and 100.718820º (E). The site is surrounded by rice paddies and fields in which other crops are grown, and there are also some small and medium-sized factories in the area. the INNOROBOT is located close to the northern entrance to TISTR, as shown on the TISTR map, near Phaholyothin Road, a major thoroughfare, so its air quality would be expected to be affected by road transportation, and particularly by the large number of cars and buses that use this road during the rush hour. The total number of vehicles registered in Pathumtani is 151,159 based on 2017 data (Boongla et al., 2019). Pathumtani province is a suburban area inside the BMR in central Thailand. It has a land area of 1,525.860 km^2 and a population of approximately 1.180247 million as of 2022. It is 27.8 kilometers north of Bangkok's center, and is connected by Paholyothin Road No.1. The yearly average rainfall range is 952-1,125 mm, the average relative humidity (RH) range is 59.0-82.0%, and the average temperature range is 24.0-32.9°C. The coldest month is January, and the hottest month is April (Thailand Meteorological Department, 2019).

2.2 Cascade air sampler for size-classified particles

The ambient aerosol was measured using a cascade air sampler capable of separating particle sizes as small as 100 nm, known as the $PM_{0.1}$ sampler or nanosampler. The casecade impactor is a series of multi-nozzle impactors, used to measure particle mass distribution. Particles were classified into six sizes: <0.1 µm ($PM_{0.1}$), 0.1-0.5 µm ($PM_{0.1-0.5}$), 0.5-1.0 µm ($PM_{0.5-1}$), 1.0-2.5 µm ($PM_{1-2.5}$), 2.5-10 µm ($PM_{2.5-10}$), and > 10 µm ($PM_{>10}$) Phairuang et al. (2022). Each stage was collected using 55-mm quartz fibrous filters (QFF) (Pallflex, 2500 QAT- UP), whereas the IF stage used a stainless-steel filter pack (SUS-316, Fiber Web, Nippon Seisen, fiber diameter = 9.8 m) packed in an initial filter cartridge. An inertial filter with an aerodynamic cutoff diameter of dp50~65 nm. The cascade air sampler was employed at a flowrate of 40 L/min, and 48-hour samples were taken for six consecutive days during the wet season in October 2017. All of the filters were pre-baked for one hour at 350 °C to eliminate any potential contamination before being conditioned in a $PM_{2.5}$ weighing chamber for 48 hours at a relative humidity (RH) of 35±5% and a temperature of 21.5±1.5 °C. In terms of air sampling, the samples were kept at -20

°C in a refrigerator until they were employed in chemical analysis. Blank filters were also utilized to correct for any contamination during filter shipment and sampling. However, during the wet season, the maximum levels of nanoparticles (NPs) are often recorded during the week rather than on weekends.

2.3 Carbonaceous component analysis

The particle-bound carbon components OC and EC were measured using a Laboratory Carbon Aerosol Analyzer using the methodology described by Boongla et al. (2019). Each filter sample had a 1.5 cm^2 (1.5 cm x 1 cm) portion punched out of it before being placed in a carbon analyzer for examination. The punched filter was heated inside the analyzer at 120, 250, 450, and 550 °C to produce four OC fractions (OC1, OC2, OC3, and OC4) in 100% Helium (He), while the three EC fractions (EC1, EC2, and EC3) were heated at a higher temperature, 550, 700, and 800 °C, respectively, in a mixture of 2% O_2 and 98% He. The data were corrected for the charring of organic materials (OPC) using a reflectance laser. OC and EC values are defined as OC1 + OC2 + OC3 + OC4 + OPC and EC1+EC2+EC3-OPC, respectively.

The char-EC/soot-EC ratios were also calculated, where char-EC equals EC1 minus OPC and soot-EC equals EC2 plus EC3 (Boongla et al., 2019). Carbon assessment quality assurance and control were regulated using a reference standard and blank filters. The carbon analysis was calibrated using total carbon (TC) as measured against sucrose ($C_{12}H_{22}O_{11}$) as a reference chemical. Based on the measured travel-blank filters (n = 3), the minimum detection limit (MDL) for OC and EC was determined to be 0.2 g/cm^2 and 0.1 g/cm^2, respectively. The carbon level in the samples was subtracted from the carbon level in the blank filters.

2.4 Meteorological

During the study period, meteorological data was received from the Meteorology Department of Thailand (TMD), Pathumtani Meteorological Station, Pathumtani Province, relative humidity, temperature, pressure, rainfall, wind speed, wind direction, and possible cover are among the meteorological data. The NPs and meteorological correlation was investigated using the Peason correlation analysis in SPSS software (version 28). Furthermore, meteorological conditions have a significant impact on the ambient air quality of metropolitan locations. As a result, the correlations between meteorological and nanoparticle concentrations in Pathumtani, Thailand.

3. Results and Discussion

3. 1 Mass concentration of size-fractionated particles

Table 1 shows the size distributions of mass concentrations for atmospheric particles in TISTR, Klong Ha, Pathumtani of Thailand. The highest mass concentration was $PM_{2.5\text{-}10,}$ followe by $PM_{0.5\text{-}1.0}$, $PM_{>10}$, $PM_{1.0\text{-}2.5}$, $PM_{0.1}$, and $PM_{0.1\text{-}0.5}$, respectively. The average atmospheric $PM_{0.1}$ in TISTR was higher than the corresponding values for Muaro Jambi, Indonesia (9.20 µg/m^3) (Amin et al., 2019), while was lower than Pathumtani, Thailand (13.47 µg/m^3) (Boongla et al., 2021).

3.2 Size distribution of carbon species

Table 2 shows the carbonaceous components in ultrafine particles (OC, EC, Char-EC, and Soot-EC, and TC) at TISTR, Klong Ha, Pathumtani of Thailand from study period, were measured using the thermal/optical transmittance (TOT) method following the NIOSH870 protocol. The average OC, EC, Char-EC, Soot-EC and TC concentrations and their ratios for $PM_{<0.1}$ in this study are showed in Table 2. This study was investigated carbonaceous aerosols including EC and OC in size-fractionated PM down to $PM_{0.1}$ samples, it is found that OC (0.67 µg/m^3) concentrations were higher than EC (0.36 µg/m^3) concentrations in study areas (Table 2). Char-EC was 0.12 µg/m^3, whereas soot-EC was 0.24 µg/m^3 and 1.02 µg/m^3 for TC. OC/EC ratios can be used to identify specific sources of carbonaceous particles. The ratios for diesel exhaust, biomass fires, and coal burning varies. The greater ratios are caused by biomass fires, whereas fossil fuel burning results in lower OC/EC ratios (Phairuang et al., 2022; Boongla et al., 2019). This study found that the OC/EC ratio was 1.95.

3.3 Relationship between carbon species

The average OC, EC, TC, char-EC, soot-EC, OC/EC(-) and char-EC/soot-EC concentrations in study period are displayed in Table 2. The char-EC/soot-EC correlation for the $PM_{<0.1}$ at sub-urban area site was less than 1. It suggest a greater influence of diesel exhaust in this

study site. According to Inerb et al. (2022), the Char-EC/Soot-EC ratio is affected by both direct emission sources and moist deposition. Higher Char-EC/Soot-EC ratios suggest that biomass combustion is dominant, as Char-EC contributes to overall EC content. At the same time, ratios less than 1.0 indicate that soot from diesel exhaust makes a considerable contribution to total EC concentrations (Boongla et al., 2022).

The findings of this work is of great importance to air pollutant control policies in sub-urban areas. This study site's source of NPs can be attributed to vehicle emission.

3.4 Correlations between meteorological conditions and $PM_{0.1}$

To find differences among the mass concentrations of mass fractions, the correlations of meteorological factors such as wind speed (Ws), wind direction (Wd), temperature (T), relative humidity (RH), surface pressure (P), and precipitation event (Pr) or rainfall on the mass concentrations of $PM_{0.1}$ also were examined in this study and presented in Table 3 and 4. In Thailand, $PM_{0.1}$ concentrations were highest in the winter and post-monsoon seasons, followed by summer, and lowest during the monsoon. Our findings of reduced atmospheric particulates concentrations in October are consistent with earlier research (Phairuang et al., 2022; Boongla et al., 2019). The studies focused on the influence of long-range transport of biomass and rice straw burning emissions in Thailand. Wet scavenging of ambient aerosols contributes to frequent precipitation throughout the monsoon season, which lasts from July to October. In addition, $PM_{0.1}$ concentrations were shown to be strongly related to air relative humidity and the number of forest fire hotspots (Sresawasd et al., 2021).

Meteorological conditions in our study revealed that Ws, Wd, and Pr were associated with $PM_{0.1}$, indicating that meteorological conditions influenced $PM_{0.1}$ mass concentration. There is a positive correlation between temperature and $PM_{0.1}$. $PM_{0.1}$ levels increased in tandem with rising temperatures. The negative correlations between relative humidity, pressure, rainfall, wind speed and $PM_{0.1}$ suggest the proportion of the decreasing of $PM_{0.1}$ and the increasing of wind speed. Strong winds generally dilute pollution, therefore, it could eliminate the level of $PM_{0.1}$ in the atmosphere.

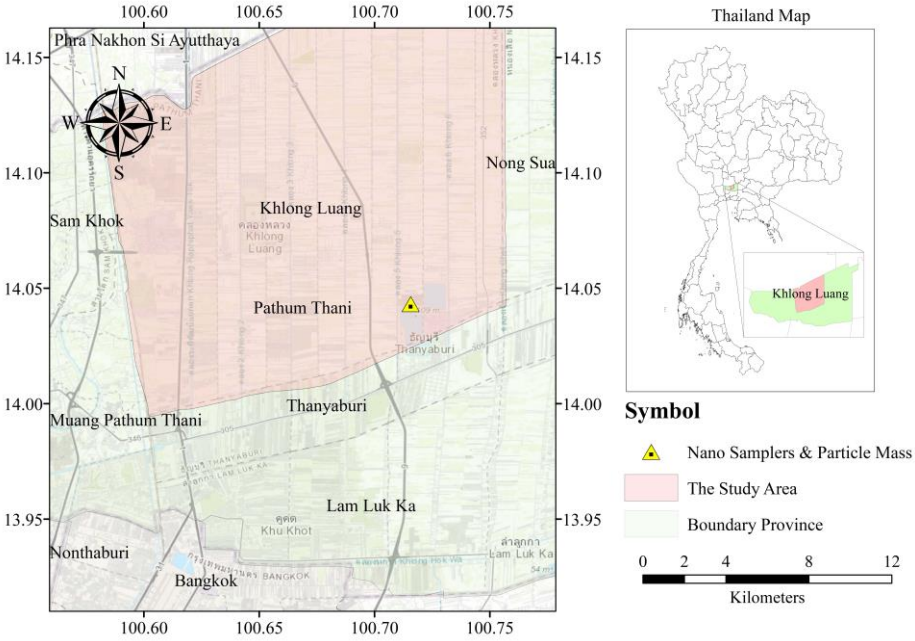

Figure 1. Location of sampling site at the Robotic Innovation and Automatic Mechanical Center, Thailand Institute of Scientific and Technological Research (TISTR), Technotani, Klong Ha, Klongluang, Pathumtani province, Thailand

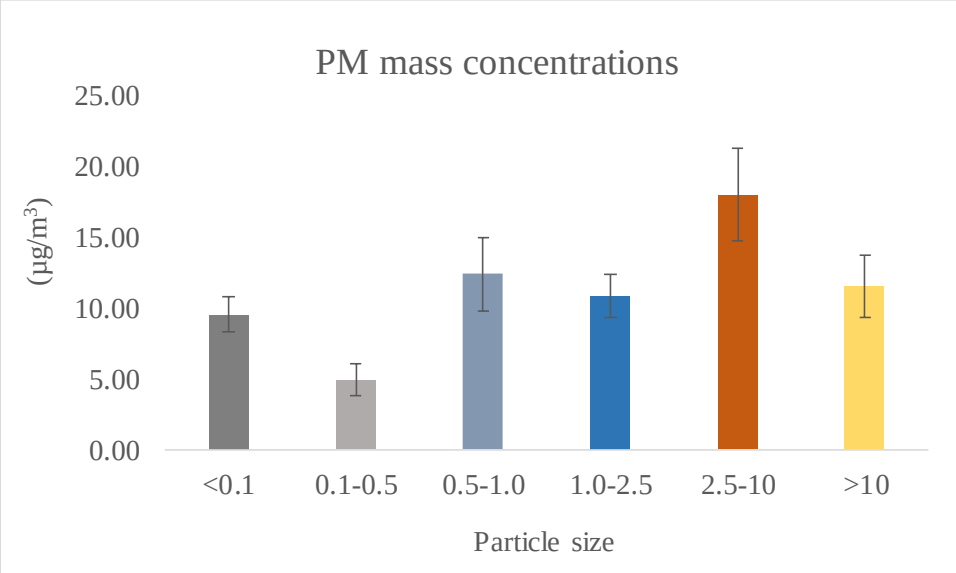

Figure 2. Size-fractionated particles mass concentration in TISTR, Klong Ha, Pathumtani of Thailand.

Table 1 PMs concentration and their ratios during the study period period in TISTR, Klong Ha, Pathumtani of Thailand**.**

Particle size	Mass concentration	Ratio of mass fraction
	(µg/m^3)	(%)
$PM_{0.1}$	9.57 ± 1.22	14.22
$PM_{0.1\text{-}0.5}$	4.94± 1.11	7.34
$PM_{0.5\text{-}1.0}$	12.44± 2.58	18.47
$PM_{1.0\text{-}2.5}$	10.86± 1.56	16.13
$PM_{2.5\text{-}10}$	18.01± 3.27	26.74
$PM_{>10}$	11.51± 2.21	17.10
$PM_{2.5}$	37.81± 3.23	56.16
TSP	67.33± 4.24	100

Table 2 Concentrations of OC, EC, Char-EC, Soot-EC, TC (µg/m^3), OC/EC and Char-EC/Soot-EC ratio in $PM_{0.1}$ at TISTR, Klong Ha, Thailand**.**

Particle size	OC	EC	Char-EC	Soot-EC	TC	OC/EC(-)	Char-EC/Soot-EC
$PM_{0.1}$	0.67± 0.15	0.36± 0.12	0.12± 0.04	0.24± 0.08	1.02± 0.25	1.95± 0.42	0.49± 0.05

Table 3 Meteorological parameters

Samping Date	Temperature (°C)	Relative humidity (%)	Pressure (mmHg)	Rainfall (mm)	Wind speed (knot)	Wind direction (degree)
10/5/2017	27.30	87.00	756.59	-	2.00	70.00
10/7/2017	28.60	85.00	755.74	2.60	3.00	70.00
10/9/2017	29.40	81.00	754.32	-	3.00	320.00
10/16/2017	29.70	73.00	754.60	0.80	4.00	230.00
10/18/2017	28.50	80.00	757.04	-	2.00	10.00
10/20/2017	30.50	76.00	757.75	-	2.00	320.00
Mean	29.00	80.33	755.89	0.57	2.67	-
SD	1.11	5.28	1.49	1.05	0.82	-
Min.	27.30	73.00	754.32	0.00	2.00	-
Max.	30.50	87.00	757.75	2.60	4.00	-

The value in the table are data which provided from Department of Thailand Meteorology.

Table 4 Correlatio between meteorological factors and $PM_{0.1}$.

Particle size	Temperature (°C)	Relative humidity (%)	Pressure (mmHg)	Rainfall (mm)	Wind speed (knot)
$PM_{0.1}$	0.395	-0.463	-0.004	-.820*	-0.092

The number in the table are regression slope; the statistically significant value at $p<0.05$ are bloded; * and ** for the conficent level of 0.01 and 0.05.

Conclusion

In this study, particle-bound carbon consisting of OC and EC in size-classified particles down to the size of nanoparticles (NPs) was examined at sub-urban area of Bangkok, Thailand, during October (wet season) 2017. The carbon species were evaluated by a thermal/optical reflectance method. The average PM concentration in size-specific PMs was found to be high in the sub-urban area. The average concentration of $PM_{0.1}$ in sub-urban area was found to be 9.57 µg/m^3 in the rainy season, whereas $PM_{0.1\text{-}0.5}$ was 14.57 µg/m^3. This finding suggested that the average concentration of $PM_{0.1}$ was greater than 50% of the concentration of $PM_{0.1\text{-}0.5}$. When NPs are exposed for an extended period of time, it is probable that they will have a long-term effect on human health. The $PM_{0.5\text{-}1.0}$ fraction had the highest OC and EC values. The carbon composition revealed that the average concentration of OC was 0.67 µg/m^3, while the average concentration of EC was 0.36 µg/m^3, implying that OC was more concentrated than EC. This study site's source of NPs can be attributed to biomass burning. In the study period (wet season), the correlations between OC and EC, as well as char-EC and soot-EC, were substantial. It implies a common combustion source, such as diesel engines. The weak associations imply that carbonaceous aerosols produced during this period is the result of more complicated sources, notably biomass combustion.

Acknowledgements

The authors would like to thank to members of the Robotic Innovation and Automatic Mechanical Center, Thailand Institute of Scientific and Technological Research (TISTR), Technotani, Klongluang, Pathumtani province for their generous support during sampling and laboratory analysis. Thank you to Prof. Dr. Mitsuhiko Hata and Prof. Dr. Masami Furuuchi Faculty of Geosciences and Civil Engineering, Institute of Science and Engineering, Kanazawa University, Japan for providing nano-air sampler.
The authors are grateful to Assistant Professor Dr. Worradorn Phairuang from Faculty of Geosciences and Civil Engineering, Institute of Science and Engineering, Kanazawa University, Japan for his support during laboratory analysis. Finally, the authors would like to thank Thammasat University for providing a conference funding.

References

1. Boongla, Y.; Chanonmuang, P.; Hata, M.; Furuuchi, M.; Phairuang, W., The characteristics of carbonaceous particles down to the nanoparticle range in Rangsit city in the Bangkok Metropolitan Region, Thailand. *Environmental Pollution.* **2021,** *272*, 1-11.
2. Tial, M K S.; Kyi, N N.; Amin, M.; Hata, M., Furuuchi, M.; Putri, R M.; Paluang, P.; Suriyawong, P.; Phairuang, W., Size-fractionated carbonaceous particles and climate effects in the eastern region of Myanmar. *Particuology*. **2023,** https://doi.org/10.1016/j.partic.2023.11.010
3. Phairuang, W.; Piriyakarnsakul, S.; Inerb, M.; Hongtieab, S.; Thongyen, T.; Chomanee, J.; Boongla, Y.; Suriyawong, P.; Samae, H.; Chanonmuang, P.; Suwattiga, P.; Chetiyanukornkul, T.; Panyametheekul, S.; Amin, M.; Hata, M.; Furuuchi, M., (2023). Ambient Nanoparticles ($PM_{0.1}$) Mapping in Thailand. *Atmosphere*. **2023,** 14(1), *66*. https://doi.org/10.3390/atmos14010066
4. Phairuang, W.; Inerb, M.; Hata, M.; Furuuchi, M., Characteristics of trace elements bound to ambient nanoparticles ($PM_{0.1}$) and a health risk assessment in southern Thailand. Journal of Hazardous Materials. 2022, 425, 127986.https://doi.org/10.1016/j.jhazmat.2021.127986
5. Sonwani, S; Madaan, S.; Arora, J.; Suryanarayan, S.; Rangra, D., Mongia, N.; Vats, T.; Saxena, P., Inhalation exposure to atmospheric nanoparticles and its associated impacts on human health: a review. *Frontiers in Sustainable Cities.* **2021,** *4*, 1-20. https://doi.org/10.3389/frsc.2021.690444
6. Xuan, L; Ju, Z.; Skonieczna, M.; Zhou, P K.; Huang, R., Nanoparticles-induced potential toxicity on human health: Applications, toxicity mechanisms, and evaluation models. MedComm. 2023, 4, 1-39. DOI: 10.1002/mco2.327
7. Ngoun, P.; Aun, S.; Amin, M.; Hang, L.; Hata, M.; Taing, C.; Kong, S.; Or, S.; Um, D.; Furuuchi, M., Monitoring Particulate Matters and Total Suspended Particles Along the Roadside and Public Area in Phnom Penh. *ASEAN International Conference on Energy and Environment*. IOP Conf. Series: Earth and Environmental Science. **2023,** *26(1)*, 438-453.
8. Dejchanchaiwong, R; Tekasakul, P., Effects of coronavirus induced city lockdown on $PM_{2.5}$ and gaseous pollutant concentrations in Bangkok. *Aerosol Air Qual Res*. **2020,** *21(4)*, 1-15. https://doi.org/10.4209/aaqr.200418
9. Choomanee, P.; Bualert, S.; Thongyen, T.; Salao, S.; Szymanski, W.W.; Rungratanaubon, T. Vertical variation of carbonaceous aerosol with in the $PM_{2.5}$ fraction in Bangkok, Thailand. *Aerosol Air Qual. Res*. **2020**, *20*, 43–52.
10. Hien, T T; Chi, N D T.; Nguyen, N T.; Vinh, L X.; Takenaka, N.; Huy, D H., Current status of fine particulate Matter ($PM_{2.5}$) in Vietnam's most populous City, Ho Chi Minh city. *Aerosol Air Qual Res*. **2019,** *19*, 2239-2251. doi: 10.4209/aaqr.2018.12.0471
11. Amin, M.; Prajati, G.; Humairoh, G. P.; Putri, R. M.; Phairuang, W.; Hata, M.; Furuuchi, M., Characterization of size-fractionated carbonaceous particles in the small to nano-size range in Batam city, Indonesia. *Heliyon*. **2023,** *9(5)*. https://doi.org/10.1016/j.heliyon.2023.e15936
12. Vejpongsa, I.; Suvachittanont, S.; Klinklan, N.; Thongyen, T.; Veres, M.; Szymanski, W. W., Deliberation between PM_1 and $PM_{2.5}$ as air quality indicators based on comprehensive characterization of urban aerosols in Bangkok, Thailand. **2017,** *Particuology*. *35*, 1-9. https://doi.org/10.1016/j.partic.2017.05.001
13. Inerb, M.; Phairuang, W.; Paluang, P.; Hata, M.; Furuuchi, M.; Wangpakapattanawong, P. Carbon and Trace Element Compositions of Total Suspended Particles (TSP) and Nanoparticles ($PM_{0.1}$) in Ambient Air of Southern Thailand and Characterization of Their Sources. **2022,** Atmosphere. 13, 626.
14. Sresawasd, C.; Chetiyanukornkul, T.; Suriyawong, P.; Tekasakul, S.; Furuuchi, M.; Hata, M.; Malinee, R.; Tekasakul, P.; Dejchanchaiwong, R. Influence of Meteorological Conditions and Fire Hotspots on PM0.1 in Northern Thailand during Strong Haze Episodes and Carbonaceous Aerosol Characterization. **2021,** Aerosol and Air Quality Serearch. 21 (11), 1-16.

Characterization and Stability Evaluation of Extracted *Mitragyna speciosa* (Kratom) Nanoemulsion

Nutlaphat Wasyot[1], Panalee Plathong[2], Narucha Khrongratsakul[3], Tritraporn Masang[4], Nisalak Trongsiriwat[5]*

[1]*Department of Industrial Chemistry, Faculty of Applied Science, King Mongkut's University of Technology North Bangkok*

**E-mail: nisalak.t@sci.kmutnb.ac.th*

Abstract:

In Thailand, *Mitragyna speciosa* (Kratom) leaves have been used for enhancing work productivity and especially pain relief, due to the opioid agonistic activities of mitragynine, an indole alkaloid only found in kratom leaves. However, its applications in medicinal and pharmaceutical industries are limited due to its poor aqueous solubility and low stability under light and heat. Therefore, Nanoencapsulation technology is utilized to solve these problems by using an oil in water (o/w) nanoemulsion system. In this work, extracted kratom nanoemulsions were formulated using a low energy method at 60-70 ºC. The optimized nanoemulsions consist in form of percent by weight; 2% oil phase, 10-20% surfactant; tween 80, 1% glycerin, and water phase. Prepared nanoemulsions were characterized in terms of appearance, particle size, zeta potential value, polydispersity index (PI), pH value, and their stability. The results showed a decreasing of particle size and PI when the concentrations of tween 80 increased. The particle sizes were about 15-110 nm. Zeta potential values were lower than -30 mV, indicating good stability. In 90 days, larger size of particle in nanoemulsions were observed in longer time storage, high temperature (50 ºC), and basic environment. However, zeta potential values of nanoemulsions were slightly changed under these conditions.

1. Introduction

Kratom (*Mitragyna speciosa*) is a local tree found in Southeast Asia in places such as Malaysia and Thailand. Its leaves are generally smoked, freshly chewed, or brewed as tea[1], and traditionally used as a medicine to enhance work productivity, treat pain relief and diarrhea. There are various pharmacological activities, which have gained attention in recent years. In Thailand, Kratom was removed from the list of prohibited substances under Schedule 5 of the Thai Narcotics Act (No.8) B.E. 2564 in 2021, which could then be legally traded, possessed, and consumed. Its consumptive effects are reported to be dose-dependent, functioning primarily as either a stimulant or sedative. Overdose consumption certainly causes undesirable effects such as sweating, vomiting, loss of appetite, and hepatotoxic, and nephrotoxic effects[2].

Mitragynine is widely known as an indole alkaloid and a major chemical component in kratom leaves, reaching 66%wt of total alkaloids. It is a psychoactive chemical substance that can bind the opioid receptor in the nervous system[3]. The stimulant effects are cocaine-like, causing more alertness and the ability to withstand prolonged sun exposure in doses smaller than 5 g. As an analgesic (morphine-like) and feelings of pleasure and euphoria are some of the sedative effects at higher doses between 5 g and 15 g[4]. Accordingly, Kratom leaves are used as a remedy for alleviating opioid withdrawal symptoms because they are easier than drugs to withdraw from. Moreover, phenolic and flavonoid compounds are found in its leaves as well. They are antioxidants that help neutralize or scavenge free radicals, including reactive oxygen species (ROS) that can be generated during metabolic processes in the body or external environments such as pollution, UV radiation, and certain chemicals. Immoderate ROS induces many diseases and damages the skin. Therefore, consuming antioxidants from natural substances in the pharmaceutical, food, supplements, and cosmetics industries is global-trending. Previously, mitragynine and kratom leaves extract were reported as possible active ingredients for anticancer, anti-inflammatory, antibacterial, antinociceptive, and antioxidant activity[5-10]. These researches indicate the possibility of added commercial value from local plants like the kratom tree. However, the application of extracted kratom is still limited by its poor aqueous solubility and low stability under light and heat.

Nanoemulsion is a type of nanoencapsulation. It consists of two immiscible liquid phases such as oil and water, in which one liquid is dispersed within another by surfactants

forming an isotropic colloidal system. Nanoemulsion can be classified as an oil-in-water (o/w) emulsion, in which the oil phase disperses in the water phase, or when the reverse occurs as a water-in-oil (w/o) emulsion. The size range of 50-200 nm leads to a transparent or translucent appearance and Brownian motion with no gravitational separation through kinetic stability. Additionally, phase separation happens over time due to the thermodynamic instability. In previous works, kratom leaves extracts were encapsulated using lipid nanoparticle systems[11,12]. However, these works were conducted with overly complex procedures and with the relatively high temperatures being the probable cause of the chemicals' decomposition. To encapsulate the kratom leaves extract effectively, it is clear that a simple low-energy method, like nanoemulsion is preferable. Spontaneous or self-emulsification is a commonly used low-energy method, which is dependent on the chemical energy stored in the components of the system to be emulsified without specific devices. The nanoemulsions were created by stirring continuously after the oil and water phases were mixed. This work aims to formulate a stable o/w nanoemulsion for encapsulating kratom leaves extract with simple and low-energy procedures to improve solubility and stability, control the dosage of bioactive compounds, and prolong shelf life.

2. Methods

2.1 Kratom leaves extraction

The maceration method was used in the extraction process. Dried Kratom leaves were ground in powder and soaked in ethanol for 7 days, then the liquid extract was carried out and filtered by vacuum filtration with a 2.5 µm pore size filter paper. A new batch of ethanol was added for the re-soaking process in triplicate. Then, the crude extract was derived by evaporating the liquid extract using a rotary evaporator.

2.2 Preparation of Nanoemulsion

To prepare a crude solution, a crude extract was pre-mixed with jojoba oil and glycerin in a certain amount and stirred on a hotplate magnetic stirrer at 60-70 ºC until a homogeneous solution was obtained. Next, the preparation of nanoemulsion was started by combining the weighed crude solution and surfactants (tween 80 and span 80) in a glass vial as an oil phase. This was followed by stirring the mixture at the same temperature with 700 rpm for 10 minutes. After that deionized (DI) water was dropwise added up to the total amount of 10 grams nanoemulsion and continuously stirred for 5 minutes.

2.3 Characterization and Evaluation

The characterizations of particle size, polydispersity index (PI), and zeta potential value were obtained from the Dynamic light scattering (DLS) technique. The process involves diluting nanoemulsions with DI water 250 times and then analyzing them using the Nanoparticle analyzer (Horiba SZ-100) with a 90º scattering angle at 25±0.5 ºC. The average value is calculated from the measurement 3 times repeatedly.

3. Results

3.1 Optimization of Nanoemulsions

To achieve the desired emulsion characteristics, including droplet size, stability, and appearance. Surfactants are indeed essential ingredients in low-energy methods that play a critical role in reducing the surface tension between immiscible phases, such as oil and water. The choice of surfactant and its concentration is a key factor in spontaneous emulsification, which requires very negative free energy and indicates greater thermodynamic stability. The free energy of emulsion formation is expressed in **Scheme 1**[13]. Accordingly, the increment of dispersion entropy is considered by determining the Hydrophile-Lipophile Balance (HLB) value. The HLB ranges from 8-16 are recommended for oil-in-water (o/w) emulsion. Besides, co-surfactants are used for properly promoting dispersibility and solubility.

Tween 80 (HLB = 15) and span 80 (HLB = 4.3) were initially selected as the surfactant and co-surfactant respectively in formulation 1-4. (**Table 1.**) The different ratios of tween 80 to span 80 were investigated as 80:20, 60:40, 40:60, and 20:80. After 16 days of storage, phase separation was observed in all of the formulations. They were quickly separated and had more turbidity when the ratio of span 80 was increased, demonstrating that the lower HLB value of span 80 and HLB_{mix} value showed less dispersion in the water phase. Therefore, the insufficient dispersion entropy probably affected their instability.

$$\Delta G = \gamma \Delta A - T\Delta S$$

Scheme 1. The free energy equation of emulsion formation. Where γ is the interfacial tension of oil-water interface, ΔA is the change in interfacial area, T is the temperature, and ΔS is the change in dispersion entropy.

In contrast, transparent nanoemulsions were collected when tween 80 was used in formulation 5-10. (**Table 2.**) Its HLB value showed good dispersion in the water phase. After the water phase was added to the oil phase that contains the surfactant, the tween 80 molecules aligned themselves at the oil-water interface with their hydrophilic heads facing outward, raising interfacial turbulence and dispersion entropy. This helped to reduce interfacial tension and nano-droplet size. Subsequently, to minimize the concentration of tween 80 its concentration was decreased from 20% to 10%wt, which could lead to a less transparent appearance and shorter storage stability. In 30 days, the results showed that the lower concentrations of tween 80 affected rapid phase separation. The concentrations in the range of 16-20%wt of tween 80 were effective in preventing phase separation and producing non-separated nanoemulsions due to their being above the critical micelle concentration (CMC). There were similar results in formulation 11-16. Their particle size, polydispersity index (PI), and zeta potential values are shown in **Figure 1.** We observed that particle sizes and zeta potential values were reduced when the concentration of tween 80 was increased. Zeta potential values of all formulations indicated great stability at over -30 mV. The increased concentration range of 16-20%wt did not significantly impact the particle size and zeta potential values. Polydisperse size distribution was obtained from polydispersity index (PI) values, which were higher than 0.05.

In comparison, reducing the concentration of glycerin from 2 to 1%wt in formulation 11-16 made nanoemulsions clearer. Glycerin was used as a co-solvent to diminish the viscosity of the oil phase. Its amphiphilic structure also improved the homogeneity. However, excessive amounts of glycerin feasibly interfered with micelle formation and dispersibility of oil droplets. Consequently, using 16-20%wt of tween 80 and 1%wt of glycerin was suitable for preparing extracted *Mitragyna speciosa* nanoemulsion with high stability.

Formulation[a]	Tween 80: Span 80[b] (%wt)	Appearance	HLB_{mix}
1	16:4	Separation	12.86
2	12:8	Separation	10.72
3	8:12	Separation	8.58
4	4:16	Separation	6.44

[a] Crude solution contained 1%wt crude extract, 1%wt jojoba oil, 2%wt glycerin with 20%wt total surfactant. [b] Surfactant and co-surfactant

Table 1. Effect of tween 80 to span 80 ratios

Formulation[a]	Glycerin (%wt)	Tween 80 (%wt)	Appearance
5	2	20	Non-separation
6	2	18	Non-separation
7	2	16	Non-separation
8	2	14	Separation
9	2	12	Separation
10	2	10	Separation
11	1	20	Non-separation
12	1	18	Non-separation
13	1	16	Non-separation
14	1	14	Separation
15	1	12	Separation
16	1	10	Separation

[a] Crude solution contained 1%wt crude extract, 1%wt jojoba oil, 1%wt glycerin

Table 2. Effect of tween 80 and glycerin concentrations

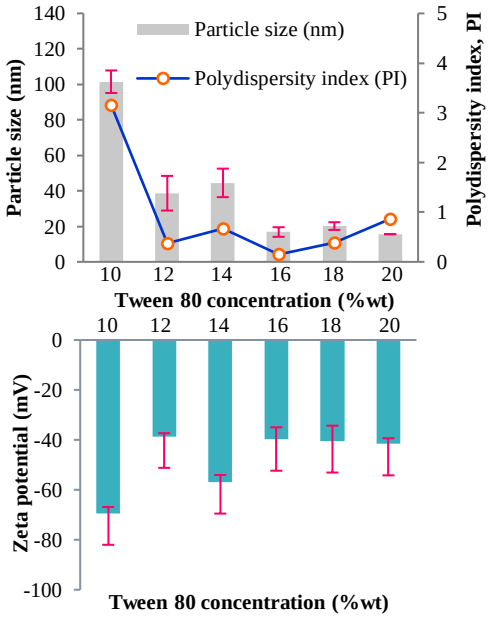

Figure 1. Effect of tween 80 concentration on particle size, polydispersity index, and zeta potential value in formulations 11-16 after preparation for 1 day.

3.2 Stability Evaluation

Nanoemulsions are kinetically stable. Their small particle size can cause disability such as flocculation, coalescence, Ostwald ripening, and creaming. In this experiment, an optimized nanoemulsion was chosen and repeated to evaluate the stability by maintaining a uniform dispersion under different conditions. There were the effects of storage time, temperature, and pH of the environments. The physical changes were detected by the DLS technique.

3.2.1 Effect of Storage Time

The storage time is a critical factor in stability. In particular, nanoemulsions are prepared by the low-energy method, which is merely stabilized by utilizing the internal chemical energy of surfactants. To explore the effect of storage time, the nanoemulsion was stored at room temperature (30 ºC) for 1, 21, and 90 days. The results showed great stability over an extended period of 90 days without phase separation. However, less transparent nanoemulsion was observed with longer time storage. (**Figure 2.**) In 21 days, the particle size was slightly changed compared with the initial nanoemulsion of 15.6±0.10 nm. However, after 90 days of storage, particle size increased significantly. Perhaps Oswald ripening and coalescence were causes of larger particle size and turbidity leading to a wide range of size distribution. However, the negligible change of zeta potential values indicated high stability.

3.2.2 Effect of Temperature

Nanoemulsions are thermodynamically unstable. The temperature was a kind of external heat energy affecting the stability of the nanoemulsion. In this phase, the nanoemulsion was divided into 3 parts and stored at different temperatures (4, 30, and 50 ºC) for 7 days. (**Figure 3.**) The higher temperature rapidly increased particle size and decreased zeta potential value in a short period. Furthermore, it led to a more rapid and energetic movement of oil droplets, and particle aggregation probably happened through collision. Hence, the lower temperature produced a better storage condition for prolonging the nanoemulsion's stability.

3.2.3 Effect of pH value environment

The chemical properties of nanoemulsions, particularly their surface charge and tolerance to electrical charge interruption, are factors that influence their stability. At the beginning, the pH value of the nanoemulsion was measured as 3.85, which placed it in an acidic range. After that, it was divided for examination into various pH value environments (pH 3, 7, and 9). (**Figure 4.**). In pH 3, the particle size was slightly altered when compared with the controlled nanoemulsion and more stabilized than in pH 7, and 9 respectively. This observation suggested nanoemulsion did not tolerate chemical charges environments like protons (H^+) and hydroxide ions (OH^-) because the chemical charges on the particle's surface was disturbed. The electrostatic repulsion of protons possibly occurred which reduced the particle size in the acidic environment, whereas in more basic environments at pH 7 and 9, the opposite electrical charges of the protons and hydroxide ions may have caused the electrostatic attraction generating the larger particle size. In pH 9, the electrostatic repulsion of excessive hydroxide ions feasibly reduced particle sizes. The addition of chemical charges also influenced variance size distribution. Nonetheless, the nanoemulsion kept its good stability, which was observed in the slight change of zeta potential value.

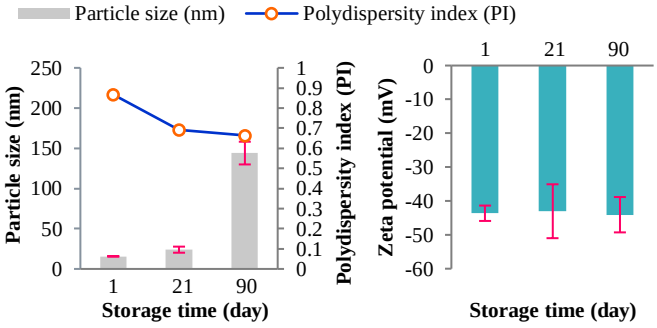

Figure 2. Effect of storage time on particle size, polydispersity index, and zeta potential value.

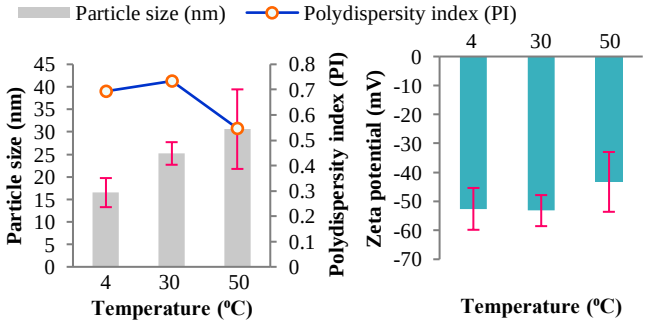

Figure 3. Effect of temperature on particle size, polydispersity index, and zeta potential value.

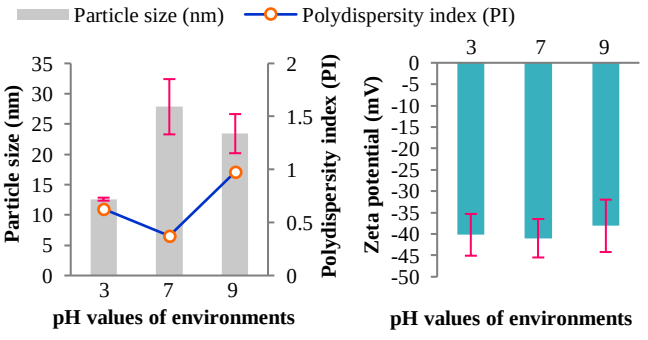

Figure 4. Effect of pH values of environments on particle size, polydispersity index, and zeta potential value.

Conclusion

In conclusion, extracted *Mitragyna speciosa* (Kratom) nanoemulsion can be formulated using spontaneous emulsification with 16-20%wt of tween 80, forming dark green transparent o/w nanoemulsions to enhance the solubility of the bioactive compounds in kratom leaves. Furthermore, the stability evaluation of prepared nanoemulsions under extended storage time, high temperature, and different pH value environments confirm their great stability and shelf life's prolongation for utilization in many industries.

Acknowledgements

This research was supported by the Department of Industrial Chemistry, Faculty of Applied Science, King Mongkut's University of Technology North Bangkok.

References

1. Hassan, Z.; Muzaimi, M.; Navaratnam, V.; Yusoff, N. H. M.; Suhaimi, F. W.; Vadivelu, R.; Vicknasingam, B. K.; Amato, D.; Hörsten, S. V.; Ismail, N. I. W.; Jayabalan, N.; Hazim, A. I.; Mansor, S. M.; Müller, C. P. From Kratom to mitragynine and its derivatives: Physiological and behavioural effects related to use, abuse, and addiction. *Neurosci*. *Biobehav*. *R*. **2013**, *37* (2), 138-151. DOI: 10.1016/j.neubiorev.2012.11.012
2. Drug Enforcement Administration, *Drug Fact Sheet: Kratom.* https://www.getsmartabout drugs.gov (accessed 2022-09-13).
3. Kitajima, M.; Misawa, K.; Kogure, N.; Said, I. M.; Horie, S.; Hatori, Y.; Murayama, T.; Takayama, H. A new indole alkaloid, 7-hydroxyspeciociliatine, from the fruits of Malaysian *Mitragyna speciosa* and its opioid agonistic activity. *J*. *Nat*. *Med*. **2006**, *60*, 28-35. DOI: 10.1007/s11418-005-0001-7
4. Prevete, E.; Kuypers, K. P. C.; Theunissen, E. L.; Corazza, O.; Bersani, G.; Remaekers, J. G. A systematic review of (pre)clinical studies on the therapeutic potential and safety profile of kratom in humans. *Hum*. *Psychopharmacol*. *Clin*. *Exp*. **2022**, *37* (1), 1-33. DOI: 10.1002/hup.2805
5. Goh, T. B.; Yian, K. R.; Mordi, M. N.; Mansor, S. M. Antioxidant value and Antiproliferative Efficacy of Mitragynine and a Silane Reduced Analogue. *Asian*. *Pac*. *J*. *Cancer*. *Prev*. **2014**, *15* (14), 5659-5665.
6. Parthasarathy, S.; Azizi, J. B.; Ramanathan, S.; Ismail, S.; Sasidharan, S.; Said, M. I. M.; Mansor, S. M. Evaluation of Antioxidant and Antibacterial Activities of Aqueous, Methanolic and Alkaloid Extracts from *Mitragyna Speciosa* (Rubiaceae Family) Leaves. *Molecules*. **2009**, *14*, 3964-3974. DOI: 10.3390/molecules14103964
7. Stolt, A. C.; Schröder, H.; Neurath, H.; Grecksch, G.; Höllt, V.; Meyer, M. R.; Maurer, H. H.; Ziebolz, N.; Havemann-Reineck, U.; Becker, A. Behavioral and neurochemical characterization of kratom (*Mitragyna speciosa*) extract. *Psychopharmacol*. **2014**, *231*, 13-25. DOI: 10.1007/s00213-013-3201-y
8. Shaik Mossadeq, W. M.; Sulaiman, M. R.; Tengku Mohamad, T. A.; Chiong, H. S.; Zakaria, Z. A.; Jabit, M. L.; Baharuldin, M. T. H.; Israf, D. A. Anti-Inflammatory and Antinociceptive Effects of *Mitragyna speciosa* Korth Methanolic Extract. *Med*. *Princ*. *Pract*. **2009**, *18*, 378-384. DOI: 10.1159/000226292
9. Yuniarti, R.; Nadia, S.; Alamanda, A.; Zubir, M.; Syahputra, R. A.; Nizam, M. *J*. *Phys*.: *Conf*. *Ser*. **2020**, *1462*, 1-7. DOI: 10.1088/1742-6596/1462/1/012026
10. Chittrakarn, S.; Sawangjaroen, K.; Prasettho, S.; Janchawee, B.; Keawpradub, N. Inhibitory effects of kratom leaf extract (*Mitragyna speciosa* Korth.) on the rat gastrointestinal tract. *J*. *Ethnopharmacol*. **2008**, *116*, 173-178.
11. Azhar, S. N. A. S.; Ashari, S. E. Strategies for the Development of *Mitragyna speciosa* (Kratom) Leaves Extract Loaded with Solid Lipid Nanoparticles. *JMEST*. **2019**, *6* (12), 100-104.
12. Azhar, S. N. A. S.; Ashari, S. E.; Tan, J. K.; Kassim, N. K.; Hassan, M.; Zainuddin, N.; Mohamad, R.; Azmi, I. D. M. Screening and selection of formulation components of nanostructured lipid carriers system for *Mitragyna Speciosa* (Korth). Havil drug delivery. *Ind*. *Crop*. *Prod*. **2023**, *198*. DOI: https://doi.org/10.1016/j.indcrop.2023.116668
13. Li, L.; Zhou, C. H.; Xu, Z.P. Self-Nanoemulsifying Drug-Delivery System and Solidified Self-Nanoemulsifying Drug-Delivery System. In *Nanocarriers for Drug Delivery*. 2019; pp 421–449. DOI: 10.1016/B978-0-12-814033-8.00014-X

Synthesis of Carbon Nanotube through Up-Cycling Hemp Waste by Chemical Vapor Deposition Method

Phuwadon Sa-Ngaimmeejaroen[1], Romnalin Duangkaewsansuk[1], Teerayut Uwanno[1,*] ,Mayuree Phonyiem Reilly [1], Winadda Wongwiriyapan [1]
[1]*College of Materials Innovation and Technology, King Mongkut's Institute of Technology Ladkrabang*
[*]*E-mail: teerayut.uw@kmitl.ac.th*

Abstract:

In this study, hemp hurd waste was up-cycled into carbon nanotubes (CNTs) by chemical vapor deposition (CVD) where carbon bearing gas from pyrolysis of hemp hurds was used as carbon source and stainless-steel mesh (SS-304) was used as catalyst and substrate. The effect of temperature for pyrolysis (T_{pyro}), temperature for CVD (T_{CVD}) and catalyst surface treatment were studied. It was found that multi-walled CNTs with various diameter and crystallinity were observed in various conditions for catalyst treatment, T_{pyro} and T_{CVD}. The results show the effect of T_{pyro}, T_{CVD} and catalyst treatment on the quality and physical properties of the synthesized CNTs, suggesting the possibility of tailoring of physical parameters of CNTs through adjustment of catalyst treatment and growth conditions.

1. Introduction

Carbon nanotubes (CNTs) are currently attracting significant interest due to their various exceptional properties, positioning CNTs as a promising material for the development of future technologies such as small, high-speed transistors, and a wide range of other applications. For mass production of CNTs, chemical vapor deposition (CVD) with carbon-bearing gas as precursor and metal particles as catalyst is widely used.[1] It was also found that CNTs can be synthesized from municipal solid wastes, such as postconsumer polyethylene (PE), polyethylene terephthalate (PET) or waste tires, as well as agricultural wastes, such as sugarcane bagasse, or died distiller grains with solubles.[2,3] In this method, organic wastes are pyrolyzed in a section of tube furnace to generate carbon bearing gases ,which are then passed into the next section of tube furnace to be used as precursor for CVD growth of CNTs where stainless-steel mesh (SS-304) was used as catalyst and substrate. It was also found that catalyst treatment with acid or oxidative thermal treatment can affect the physical properties of grown CNTs. [2-5] In this study, hemp hurds were used as starting material for obtaining carbon-bearing gas for CVD, as it is expected that the amount of industrial hemp wastes will greatly increase because of growing popularity of hemp cultivation in Thailand spurred by recent legalization for commercial use.

In this research, the effect of SS 304 treatment and temperature of pyrolysis and CVD on physical properties of CNTs were studied.

2. Materials and Methods

2.1 Materials

Hemp hurds were obtained from Eastern Spectrum Group Co. Ltd, Thailand. Ethanol (Qrec) HCl 37% (HCl) was used in catalyst treatment process. Stainless steel mesh 304 (SS304, 200 mesh size) was used as catalyst and substrate for growth. N_2 gas (99.999%) was used as carrier gas for pyrolysis and CVD.

2.2 Methods

SS-304 meshes were cut into 5x18 cm size and were sonicated in ethanol or 1 M HCl solution for 10 minutes. HCl-washed mesh was rinsed with, deionized water. Then the meshes were dried by air blow.

Hemp hurds were firstly dried in oven to remove moisture at a temperature of 100 °C for 24 hours. 4 grams of hemp hurds were loaded into an alumina crucible and the crucible was placed inside quartz tube at middle of the first zone of two-zone tube furnace where carrier gas would enter, as shown in Figure 1. The treated mesh was rolled and placed at the middle of the second zone of tube furnace. N_2 gas was flowed at 500 sccm. Both zones were simultaneously heated to designated temperature, shown in Table 1 and were kept constant for 1 hour. Hereafter, each synthesis

condition will be referred to the following format: catalyst treatment (E or H) T_{pyro} – T_{CVD}, for example, ethanol treated catalyst, T_{pyro} = 800 °C, T_{CVD} = 800 ° C is E 800 – 800.

In addition, ethanol-treated and HCl-treated catalysts were heated to 800 °C and 850 °C in N_2 atmosphere for 1 hour, without hemp hurds in first zone of tube furnace, in order to investigate surface morphology of catalysts at each growth temperature.

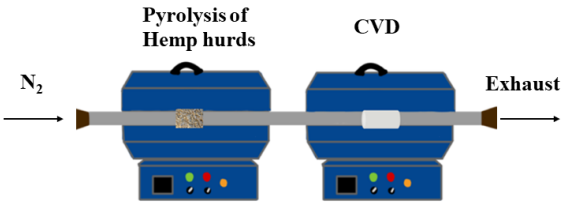

Figure 1 Tube furnace setup.

Table 1 Conditions for temperature of pyrolysis and CVD

Temperature of Pyrolysis (°C)	Temperature of CVD (°C)
750	750
800	800
850	
850	850

2.3 Characterization

Treated catalysts surface morphology was investigated by atomic force microscopy (AFM). The synthesized CNTs were characterized by Field emission Scanning electron microscopy (FE-SEM), transmission electron microscopy (TEM) and Raman spectroscopy using 532 nm laser for excitation.

3. Results

AFM images of differently treated catalyst surface are shown in Figure 2. It was observed that both treatment without heating resulted in similar root mean square (RMS) of surface height, which represents surface roughness (Figure 2 (a), (b)). This could be because the only difference was the removal of surface oxide from SUS 304 catalyst. The average grain size of ethanol-treated and HCl-treated catalyst surface were 114 ± 90 nm and 180 ± 74 nm, respectively. Significant increase in RMS was observed for both treatment when heated to 800 °C, suggesting formation of nanoparticle-like morphologies on surface. Average grain size of ethanol-treated and HCl-treated catalyst surface heated to 800 °C were 303 ± 90 nm and 256 ± 70 nm, respectively, suggesting grain growth. However, at 850 °C RMS decreased, possibly because of increasing effect of diffusion of atoms at higher temperature, resulting in smoother surface. Average grain size of ethanol-treated and HCl-treated catalyst surface heated to 850 °C were 239 ± 74 nm and 257 ± 75 nm, respectively. The increased RMS should give more growth sites for CNTs.

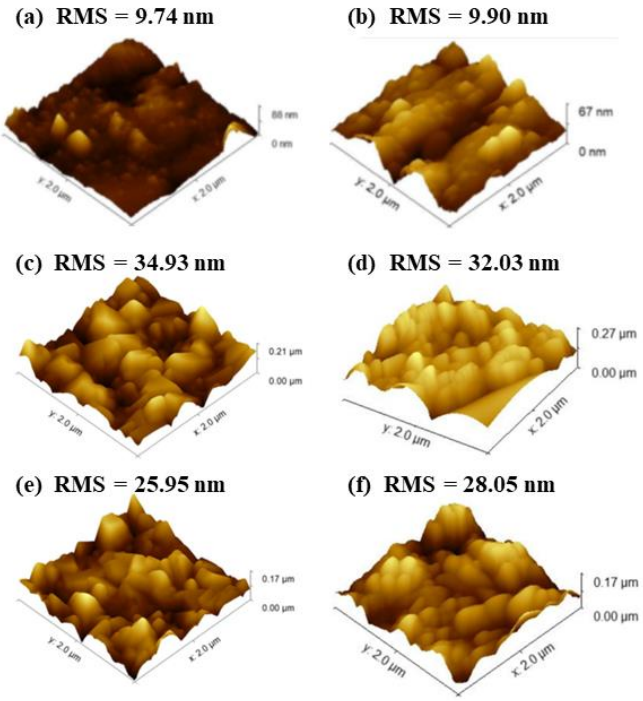

Figure 2 AFM images of catalyst surface.
(a) Ethanol treated. (b) HCl treated. (c) Ethanol treated and heated to 800 °C. (d) Ethanol treated and heated to 850 °C. (e) HCl treated and heated to 800 °C. (f) HCl treated and heated to 850 °C.

SEM images of grown CNTs are shown in Figure 3. It was found that multiwalled-CNTs can be obtained in various conditions. Condition of E 800 – 800 gave quite large amount of CNTs but also the largest average diameter of 318 ± 76 nm. This could be, as suggested by AFM, because of the highest RMS giving largest amount of CNTs but also the largest grain size giving the largest diameter of CNTs for ethanol-washed catalyst heated to 800 °C. For E 850 – 850, smaller amount

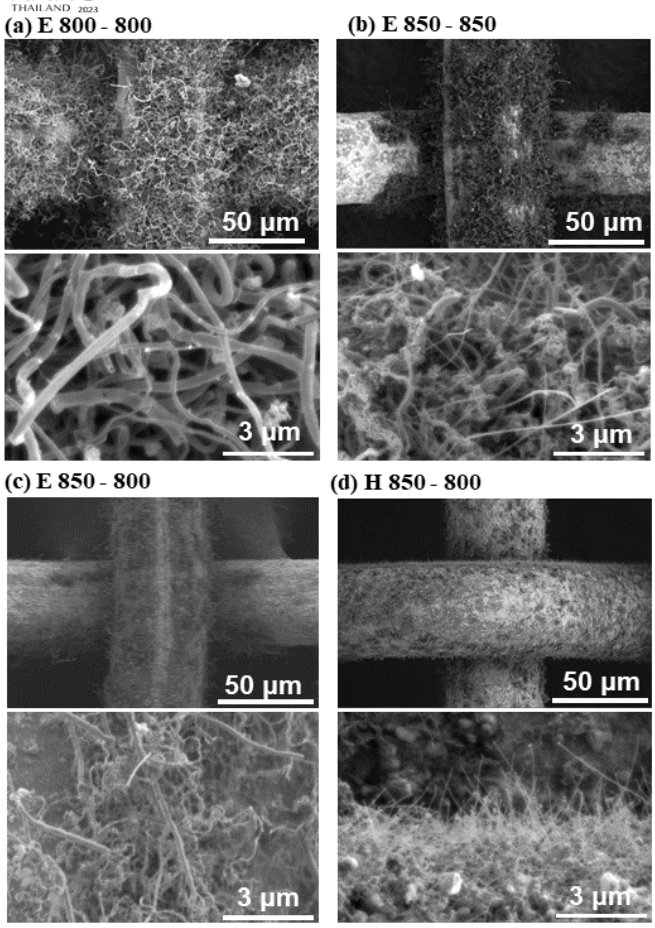

Figure 3 SEM images of as-grown CNTs in selected conditions: (a) E 800 – 800, (b) E 850 – 850, (c) E 850 – 800, (d) H 850 – 850.

of CNTs, tangled with amorphous carbon was observed, with average diameter was 128 ± 49 nm. This also follows the trend from AFM, where smaller RMS and smaller grain size was observed in ethanol-washed catalyst heated to 850 °C. For E 850 – 800, highly tangled and curled CNTs with average diameter of 178 ± 53 nm were observed. This may be because higher T_{pyro} gave larger amount carbon precursor compared to E 800 – 800, enabling more growth in various sites, leaving less space for CNTs to grow into straight tubes. For H 850 – 800, CNTs with average diameter of 32 ± 7.8 nm were observed. This suggests that the effect of catalyst treatment with HCl is not only removing surface oxide but also facilitating formation of growth sites that gives CNTs with smaller diameter.

Figure 4 shows TEM images of CNTs grown in conditions of E 850 – 850, and H 850 – 800, respectively. It can be seen that grown

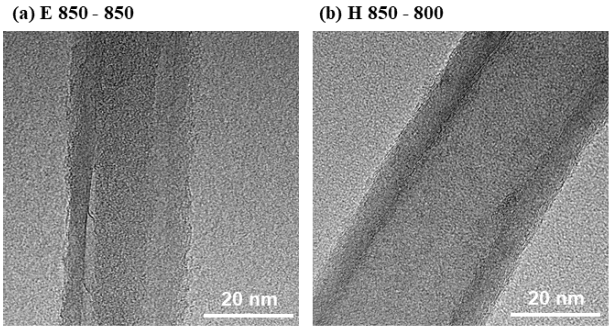

Figure 4 TEM images of as-grown CNTs in selected conditions: (a) E 850 – 850, (b) H 850 – 800.

samples are multiwalled CNTs, as hollowed tubes with layered walls were observed.

Raman spectra of as-grown CNTs are shown in Figure 5. D band and G band of graphitic carbon were observed in all conditions shown. Additionally, 2D band was observed in E 850 – 850 and H 850 – 800, suggesting better crystallinity and periodicity of CNTs over other conditions. G band to D band intensity ratio (I_G/I_D) in E 800 – 800, E 850 – 850, E 850 – 800 and H 850 – 800 were 0.94, 0.77, 1.03 and 0.95, respectively. This contradicts with the presence and intensity of 2D band, as larger D band intensity suggests a greater number of defects, but in this case, Raman spectra were taken from as-grown samples, meaning D band may be from amorphous carbon that were generated outside of CNTs structure during CVD. Therefore, the intensity of D band in this case can be used as indicator of the sum of defects on CNTs and the amount of amorphous carbon mixed within as grown CNTs.

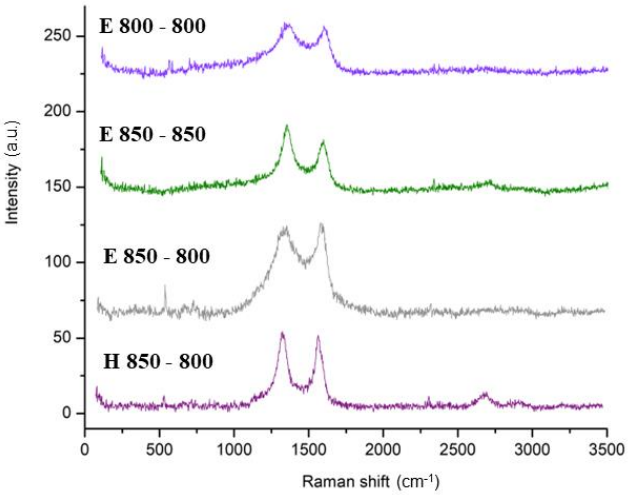

Figure 5 Raman spectra of as-grown CNTs in selected conditions.

Conclusion

CNTs were successfully synthesized from hemp hurds by pyrolyzing hemp hurds and using the generated carbon-bearing gas as precursor in CVD with SS304 mesh as catalyst and substrate. It was shown that catalyst treatment, pyrolysis temperature and CVD temperature resulted in variation of properties of as grown samples such as, diameter, length and crystallinity of CNTs, and also the amount of amorphous carbon in as grown samples. This suggests the possibility of tailoring of physical parameters of CNTs through adjustment of catalyst treatment and growth conditions.

Acknowledgements

This research was partially supported by Fundamental fund 2024 from TSRI.

References

1. Maruyama,T. Current status of single-walled carbon nanotube synthesis from metal catalysts by chemical vapor deposition. *Materials Express* **2018**, *8*, 1-20.
2. Zhuo, C.; Alves, J. O.; Tenorio, J. A. S.; Levendis, Y. A.. Synthesis of Carbon Nanomaterials through Up-Cycling Agricultural and Municipal Solid Wastes. *Ind. Eng. Chem. Res*. **2012**, *51*, 2922-2930.
3. Panahi, A.; Wei, Z.; Song, G.; Levendis, Y. A. Influence of Stainless- Steel Catalyst Substrate Type and Pretreatment on Growing Carbon Nanotubes from Waste Postconsumer Plastics. . *Ind. Eng. Chem. Res*. **2019**, *58*, 3009-3023.
4. Wulan, P. D. K.; Wijardono, S. B. Finding an Optimum Period of Oxidative Heat Treatment on SS 316 Catalyst for Nanocarbon Production from LDPE Plastic Waste. *Int. J. Adv. Sci. Eng. Inf. Technol.* **2017**, *7*, 552-558.
5. Burt, D P.; Whyte, W. m.; Weaver, J. R. M.; Glidle, A.; Edgeworth, J. P.;Macpherson, J. V.; Dobson, P. S. Effects of Metal Underlayer Grain Size on Carbon Nanotube Growth. *J. Phys. Chem. C.* **2009**, *113*, 15113-15139.

Effects of capping agent on tin dioxide nanoparticles synthesized by a simple precipitation method

Chutima Nakmuk[1], Cheewita Suwanchawalit[2], Montri Aiempanakit[1], Chawarat Siriwong[1]*
[1] *Department of Physics, Faculty of Science, Silpakorn University, Nakhon Pathom, Thailand*
[2]*Department of Chemistry, Faculty of Science, Silpakorn University, Nakhon Pathom, Thailand*
**E-mail: first_164@hotmail.com*

Abstract:

In this work, nanoparticles of tin dioxide (SnO_2) were synthesized by a simple precipitation method. Tin (II) chloride dihydrate ($SnCl_2{\cdot}H_2O$) and sodium hydroxide (NaOH) were used as starting material. Lemon-lime vitamin C water was used as a capping agent. The effect of the capping agent on the properties of SnO_2 such as crystal structure, and morphology is investigated. The structural properties of the obtained samples were studied by X-ray diffraction (XRD), field emission scanning electron microscopy (FE-SEM), and transmission electron microscope (TEM). The chemical composition is analyzed by energy dispersive spectroscopy (EDS). Fourier transform infrared spectroscopy (FT-IR) was used to determine the functional groups present in the sample. The XRD results showed that all SnO_2 nanoparticle samples are in a tetragonal structure. There is a significant on the crystal size of the SnO_2 nanoparticles with different capping agents. The FE-SEM images showed all samples consisted of agglomerated spherical grains. The prepared samples had the expected elements, tin, and oxygen confirmed by the EDS analysis. Due to the small particle size and large surface area in contact, it can be used as a gas detector.

Keywords: SnO_2, Nanoparticles, Tin dioxide Nanoparticles, Precipitation method, Capping agent

1. Introduction

SnO_2, a metal oxide semiconductor, has been receiving a lot of attention lately. With an energy gap of 3.6 eV, it is considered a promising material for gas sensors[1-3], solar cells[4-6], photocatalytic[7-8], and lithium-ion batteries[9-10]. SnO_2 can be synthesized using So-gel[11], hydrothermal[12], or simple precipitation[13-16], which is the most efficient, economical, fast, and simple method. The nano-level particle size results are also provided.

Previous research has revealed that the surface area of nanoparticles used as gas detectors on gas sensors should be large, which will increase the rate of gas detection[17]. Honarmand et al., synthesized SnO_2 with $SnO_2{\cdot}2H_2O$ as a precursor and used an extract of jujube fruit as a capping agent, resulting in a tetragonal structure of SnO_2 nanoparticles which has a crystal size of approximately 18 nm[18]. Luque et al., used Citrus×paradisi extract to synthesize SnO_2 by using 1%, 2%, and 4% volume relative to the volume[8] and used orange peel to synthesize SnO_2 using concentrations of orange peel extract 1%, 2%, and 4% volume[19]. Garraf et al., used Lycopersicon esculentum peel extract to synthesize SnO_2 using concentrations of 1%, 2%, and 4%, with volume[20]. All these particles have a smaller particle size when the percentage of capping agent is increased. It can be inferred that the capping agent has an impact on the particle size. Previous researchers used a product that was derived from nature. Makes it impossible to maintain the same concentration. It will be dependent on natural factors. Vitamin C and sweetness from fruit sugar are present in the capping agent used by previous researchers. There is research supporting that glucose can help reduce the size of particles[21]. Consequently, researchers are seeking products that can regulate concentration. Both vitamin C and sugar are present in it.

This study proposes a simple precipitation technique for synthesizing SnO_2 nanoparticles with $SnO_2{\cdot}2H_2O$ as a tin source. Various amounts of vitamin C water (0, 2%, 5%, and 10% volume) are being used. The pH of the solution can be determined by using a NaOH solution. The temperature for annealing was selected at 500°C. The capping agent's effects were observed through the analysis of the nanoparticles.

2. Materials and Methods

The researcher decided to use a vitamin C water brand available on the market. The amount of ingredients in every bottle is reliable and will be advantageous for repeat experiments.

2.1 Materials

In this research, we used tin (II) chloride 2-hydrate ($SnCl{\cdot}2H_2O$), from *KemAus*, Australia, as a precursor of SnO_2 ; sodium hydroxide (NaOH), from Pine Chemical CO., LTD., lemon-lime vitamin C water, from Nong Khai Power Drink Co., Ltd. and deionized water.

2.2 Synthesis

In the experimental method, DI water and vitamin C water (2% volume) are mixed first and stirred for 5 minutes. After that, tin (II) chloride 2-hydrate is added and stirred for 5 minutes. To control the pH of the solution sodium hydroxide of 0.5 M was added. Keep stirring for an additional 3 hours. Then placed in a hot air oven with a temperature of 80°C for 24 hours. Finally, the powder was annealed at 500°C for 3 hours. to produce nanoparticles of tin dioxide. Repeat the process at 5%, 10%, and without vitamin C water. The samples were labeled as SnO_2 (without vitamin C water), 2C-SnO_2 (with 2% vitamin C water), 5C-SnO_2 (with 5% vitamin C water), and 10C-SnO_2 (with 10% vitamin C water), respectively.

2.3 Characterization

The tin dioxide nanoparticles were analyzed to determine the properties of SnO_2, which include crystal structure and morphology. X-ray diffraction (XRD), field emission scanning electron microscopy (FE-SEM), and transmission electron microscopy (TEM) were utilized to study the structural qualities of the obtained samples. energy dispersive spectroscopy (EDS) is used to analyze the chemical composition. The functional groups present in the sample were determined using fourier transform infrared spectroscopy (FT-IR).

3. Results

3.1 X-ray diffraction (XRD)

X-ray diffraction studies of the synthesized SnO_2 nanoparticles (SnO_2, 2C-SnO_2, 5C-SnO_2, and 10C-SnO_2) can be seen in Figure 1. Crystalline planes (110), (101), (200), (211), (220), (002), (310), (112), (301), (202), (321) were found at 2θ values of 26.6°, 34°, 38°, 51.8°, 54.8°, 57.9°, 61.9°, 64.6°, 66°, 71.3°, and 78.7°, respectively, according to the results and files 41–1445 of JCPDS[22]. SnO_2 nanoparticles have a rutile-type tetragonal crystal structure. The purity of the sample is confirmed by the absence of other phases that were not consistent with SnO_2, as observed in all samples.

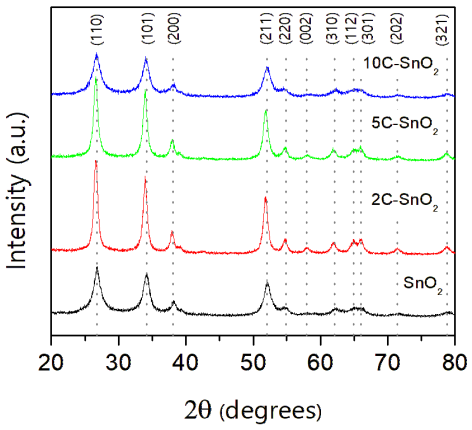

Figure 1. The X-ray diffraction study of SnO_2 nanoparticles.

3.2 Field emission scanning electron microscopy and energy dispersive X-ray spectroscopy (FE-SEM and EDS)

To comprehend and examine the morphology and composition of SnO_2 nanoparticles made by a simple precipitation method with various levels of vitamin C water. Thus, FE-SEM and EDS investigations were conducted, as demonstrated in Figure 2., left, and Table 1. The clustering of small nanoparticles and similar spherical morphology were observed in all samples. As the percent of vitamin C water increases, the intensity of carbon (C) in the EDS also increases, which leads to organic matter remaining in the nanoparticles (Table 1). The carbon in the sample is a result of the capping

agent used in the synthesis. The use of vitamin C water in the simple precipitation synthesis of SnO_2 nanoparticles can create particles at the nanoscale size.

Table 1: Elemental analysis of SnO_2

Sample	Element (Atomic %)		
	C	O	Sn
SnO_2	10.18	57.12	32.70
2C-SnO_2	12.67	57.17	30.16
5C-SnO_2	14.57	55.33	30.10
10C-SnO_2	18.06	57.08	24.86

3.3 Transmission electron microscopy (TEM)

The TEM analysis of SnO_2 nanoparticles in Figure 2., (right) shows the morphology of SnO_2 nanoparticles prepared with different percentages of the extract. All particles are quasi-spheres in shape. The diameter of the SnO_2 sample is the largest, while the diameter of the 10C-SnO_2 sample is the smallest. These pictures show that nanoparticles are aggregated and have a quasi-spherical shape. The particle size is measured using the ImageJ program by performing 100 measurements and obtaining the average size of the samples. The average size for the SnO_2, 2C-SnO_2, 5C-SnO_2, and 10C-SnO_2 is 10.0, 9.9, 8.2, and 7.3 nm, respectively. Therefore, the capping agent affects the size of the SnO_2 nanoparticles. The diameter of the synthesized nanoparticles decreases as the capping agent percentage increases.

3.3 Fourier transform infrared spectroscopy (FT-IR)

The functional molecules in the SnO_2 nanoparticles were analyzed using the FT-IR spectrum between 400-4000 cm^{-1}. Figure 3. displays similar bands, with the 10C-SnO_2 sample having a clearer peak. There were three vibration bands detected in the spectrum, at 2935, 1628, and 495 cm^{-1} respectively. SnO_2 was confirmed present in the sample by the vibration band at 495 cm^{-1}. The vibration band at 1628 cm^{-1} shows a strong stretching of C=C, indicating the presence of carbon from adding vitamin C water. The vibration band at 2935 cm^{-1} indicates the presence of O-H groups.

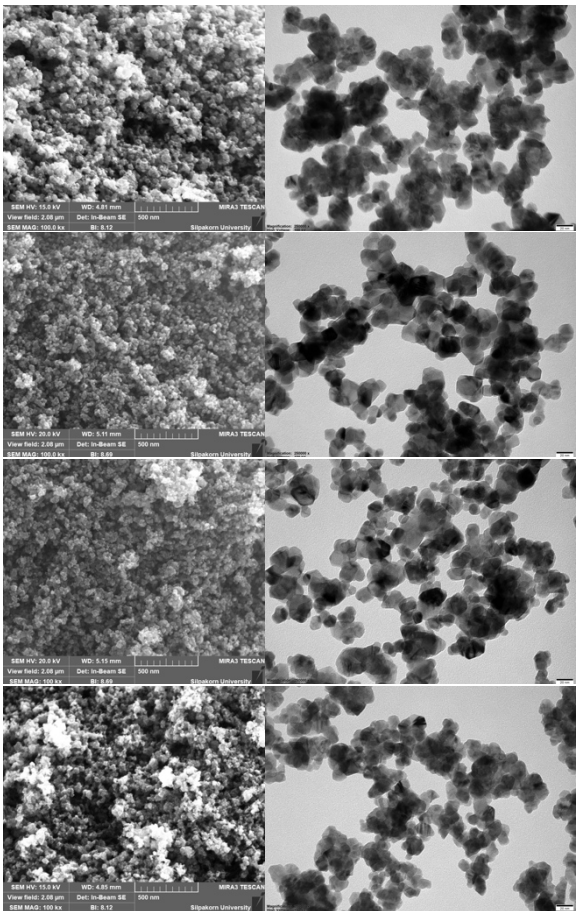

Figure 2. The FE-SEM (left) and TEM (right) study of SnO_2 nanoparticles. (a) SnO_2 (b) 2C-SnO_2 (c) 5C-SnO_2 (d) 10C-SnO_2.

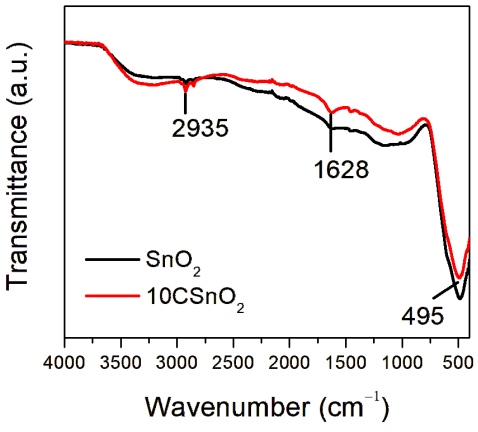

Figure 3. FT-IR spectra of the SnO_2 nanoparticle of SnO_2 (black-line) and 10C-SnO_2 (red-line) sample

Conclusion

SnO_2 nanoparticles were synthesized using a simple method using lemon-lime vitamin C water. The structure, size, and morphology of SnO_2 nanoparticles were investigated by XRD, FE-SEM, TEM, EDS, and FT-IR analysis. The XRD pattern shows the tetragonal structure of SnO_2 nanoparticles. All SnO_2 nanoparticles have spherical morphology as revealed by the FE-SEM image. EDS is used to characterize biosynthesized nanoparticles that contain tin (Sn) and oxygen (O) elements. In the TEM image, the morphology of all SnO_2 nanoparticles is spherical, like the FE-SEM technique. The particle sizes displayed are 10.0, 9.9, 8.2, and 7.3 nm, which are following the amount of vitamin C added. The particles decreased in size when vitamin C water was increased. The success of synthesizing SnO_2 was proved by the FT-IR analysis of SnO_2 nanoparticles. Overall, the easy synthetic process was successful in synthesizing small nanoparticles, and the substance can be tested as a gas detector in future work.

Acknowledgments

The authors express their gratitude to the Department of Physics, Faculty of Science at Silpakorn University in Nakhon Pathom, Thailand for their financial assistance.

References

1. Shen, Y.; Wang, W.; Fan, A.; Wei, D.; Liu, W.; Han, C.; Shen, Y.; Meng, D.; San, X., Highly sensitive hydrogen sensors based on SnO_2 nanomaterials with different morphologies. *International Journal of Hydrogen Energy*, **2015**, 40(45), 15773-15779.
2. Lu, Z.; Zhou, Q.; Xu, L.; Gui, Y.; Zhao, Z.; Tang, C.; Chen, W., Synthesis and characterization of highly sensitive hydrogen (H2) sensing device based on Ag doped SnO_2 nanospheres. *Materials*, **2018**, 11(4), 492.
3. Duoc, V. T.; Hung, C. M.; Nguyen, H.; Van Duy, N.; Van Hieu, N.; Hoa, N. D.; Room temperature highly toxic NO_2 gas sensors based on rootstock/scion nanowires of SnO_2/ZnO, ZnO/SnO_2, SnO_2/SnO_2 and, ZnO/ZnO. *Sensors and Actuators B: Chemical*, **2021**, 348, 130652.
4. Xu, C.; Liu, Z.; Sun, Q.; Lee, E. C., Morphology control of SnO_2 layer by solvent engineering for efficient perovskite solar cells. *Solar Energy*, **2021**, 214, 280-287.
5. Zhang, Z.; Roy, R.; Tang, Y.; Yang, F.; Yang, J.; Hu, Y.; Liu, H., Excellent electron transport via inserted a special electron-withdrawing material on SnO_2 surface for high efficient perovskite solar cells. *Materials Letters*, **2021**, 302, 130425.
6. Ashina, A.; Battula, R. K.; Ramasamy, E.; Chundi, N.; Sakthivel, S.; Veerappan, G., Dip coated SnO_2 film as electron transport layer for low temperature processed planar perovskite solar cells. *Applied Surface Science Advances*, **2021**, 4, 100066.
7. Luque, P. A.; Chinchillas-Chinchillas, M. J.; Nava, O.; Lugo-Medina, E.; Martínez-Rosas, M. E.; Carrillo-Castillo, A.; Vilchis-Nestor, A.R.; Madrigal-Muñoz, L. E.; Garrafa-Gálvez, H. E., Green synthesis of tin dioxide nanoparticles using Camellia sinensis and its application in photocatalytic degradation of textile dyes. *Optik*, **2021**, 229, 166259.
8. Luque, P. A.; Garrafa-Gálvez, H. E.; Nava, O.; Olivas, A.; Martínez-Rosas, M. E.; Vilchis-Nestor, A. R.; Villegas-Fuentes, A.; Chinchillas-Chinchillas, M. J., Efficient sunlight and UV photocatalytic degradation of Methyl Orange, Methylene Blue and Rhodamine B, using Citrus× paradisi synthesized SnO_2 semiconductor nanoparticles. *Ceramics International*, **2021**, 47(17), 23861-23874.
9. Liang, C.; Yang, H.; Yu, K.; Jin, W., Sunflower seed husk-derived submicron carbon spheres and SnO_2 nanoparticles composite used as an anode for high-performance lithium-ion batteries. *Diamond and Related Materials*, **2021**, 116, 108392.
10. Deng, X.; Zhu, M.; Ke, J.; Li, W.; Xiong, D.; Feng, Z.; He, M., SnO_2-ZnO nanoparticles wrapped in graphite nanosheets as a large-capacity, high-rate and long-lifetime anode

for lithium-ion batteries. *Chemical Physics Letters*, **2021**, 769, 138392.

11. Abdelkader, E.; Nadjia, L.; Naceur, B.; Noureddine, B., SnO_2 foam grain-shaped nanoparticles: Synthesis, characterization and UVA light induced photocatalysis. *Journal of Alloys and Compounds*, **2016**, 679, 408-419.
12. Felcia, E. B.; Gnanam, K. D., Synthesis and characterization of SnO_2 nanoparticle by microwave assisted hydrothermal method. *J. Appl. Phys.*, **2017**, 2278, 89-104.
13. Habte, A. G.; Hone, F. G.; Dejene, F. B., Influence of annealing temperature on the structural, morphological and optical properties of SnO_2 nanoparticles. *Physica B: Condensed Matter*, **2020**, 580, 411760.
14. Habte, A. G.; Hone, F. G.; Dejene, F. B., Effect of solution pH on structural, optical and morphological properties of SnO_2 nanoparticles. *Physica B: Condensed Matter*, **2020**, 580, 411832.
15. Kawade, A. N.; Bhujbal, P. K.; Supekar, A. T.; Pathan, H. M.; Sonawane, K. M., Eosin-Y sensitized tin oxide (SnO_2): Fabrication and its analysis. *Optik*, **2020**, 216, 164968.
16. Yang, S. Z.; Huang, Y. F.; Han, X. C.; Han, G. H., Enhancing electrochemical performance of SnO_2 anode with humic acid modification. *Transactions of Nonferrous Metals Society of China*, **2021**, 31(7), 2062-2073.
17. Wang, F.; Hu, K.; Liu, H.; Zhao, Q.; Wang, K.; Zhang, Y., Low temperature and fast response hydrogen gas sensor with Pd coated SnO_2 nanofiber rods. *international journal of hydrogen energy*, **2020**, 45(11), 7234-7242.
18. Honarmand, M.; Golmohammadi, M.; Naeimi, A., Biosynthesis of tin oxide (SnO_2) nanoparticles using jujube fruit for photocatalytic degradation of organic dyes. *Advanced Powder Technology*, **2019**, 30(8), 1551-1557.
19. Luque, P. A.; Nava, O.; Soto-Robles, C. A.; Chinchillas-Chinchillas, M. J.; Garrafa-Galvez, H. E.; Baez-Lopez, Y. A.; Valdez-Núñezc, K.P.; Vilchis-Nestord, A.R.; Castro-Beltrán, A., Improved photocatalytic efficiency of SnO_2 nanoparticles through green synthesis. *Optik*, **2020**, 206, 164299.
20. Garrafa-Galvez, H. E.; Nava, O.; Soto-Robles, C. A.; Vilchis-Nestor, A. R.; Castro-Beltrán, A.; Luque, P. A., Green synthesis of SnO_2 nanoparticle using Lycopersicon esculentum peel extract. *Journal of Molecular Structure*, **2019**, 1197, 354-360.
21. Jeyarani, W. J.; Tenkyong, T.; Bachan, N.; Kumar, D. A.; Shyla, J. M., An investigation on the tuning effect of glucose-capping on the size and bandgap of CuO nanoparticles. *Advanced Powder Technology*, **2016**, 27(2), 338-346.
22. Horti, N. C.; Kamatagi, M. D.; Patil, N. R.; Wari, M. N.; Inamdar, S. R., Photoluminescence properties of SnO_2 nanoparticles: effect of solvents. *Optik*, **2018**, 169, 314-320.

ENHANCING THE TDS REMOVAL IN SEDIMENTATION PROCESS BY GRAPHENE MAGNETIC PROPERTY

Suchanan Thanyaphutthinon[1], Nawatch Surinkul[1,] *, Suwanna Boontanon[1], Tippabust Eksangsri[2]
[1] *Department of Civil and Environmental Engineering, Faculty of Engineering, Mahidol University, Thailand*
[2] *Department of Chemical Engineering, Faculty of Engineering, Thammasat University, Thailand*
* *E-mail: Nawatch.sur@mahidol.ac.th*

Abstract:

Seawater intrusion occurs every year, causes high salinity or high Total Dissolved Solid (TDS) to fresh water. This also affects the water quality especially as the problem occurring in Chao Pa Ya River, Thailand. This problem can be harmful to human health as the use of tap water for drinking water. Reverse Osmosis (RO) process is the usually method to solve this problem. However, cost of investment is quite high including operation and maintenance cost, and can be used only for the period of intrusion. Nowadays, graphene applications are using for water purification as adsorbent. Magnetic property of graphene from Magnetic Graphene Oxide (MGO) is aimed assisting the strong bonding of adsorption process and enhancing rapidly settlement of particles for TDS removal. Synthesis of graphite to graphene by Modified Hammer's method and adding magnetic property with $FeCl_3$•$6H_2O$ and $FeCl_2$•$4H_2O$ solution were applied. Results from adsorption showed that percent removal of TDS in synthesized NaCl water was up to 70% with the equilibrium time at 10 mins. The experiments also revealed that the optimum dosage of MGO adsorbent was 20 mg in synthesized water of 20 mL with the initial NaCl concentration of 1,800 mg/L. Therefore, the settling time between using and not using the magnet were 3 mins and more than 20 mins, respectively. In summary, the application of magnet property of MGO could be the promising technology for treating TDS water.

1. Introduction

Seawater intrusion to the rivers can make the high salinity and high Total Dissolved Solid (TDS) to water resource which later affects to the tap water. Not only natural resource, but also the reuse of water for many times in industries also create the high TDS concentration in water system. High TDS water is harmful to human from drinking activity. Reverse Osmosis (RO)[1] process is an effective process to treat high TDS water for drinking however, the cost and maintenance are quite high and not worth to use for the short period of the year. In industrial effluent standard, TDS concentration is limited to 3,000 mg/l. Pollution Control Department (PCD) considered that TDS in discharged water should not over 5,000 mg/l when discharging into the sea. For drinking water or tap water, TDS should not over than 600 mg/L.[2] Otherwise, it can cause the harmful to human health.

In this study, "graphene" is used to treat water. With a magnetic property, graphene can adsorb dissolved solid and easily be separated from water. Thus, graphene is expected to treat highly TDS water.

2. Materials and methods

2.1 Materials

Graphite powder (< 20µm) was product from Aldrich. $FeCl_3$•$6H_2O$ (97%) and HCl (34.5%) were from Loba Chemie. $FeCl_2$•$4H_2O$, H_2O_2 (30%), Ammonia (28%) were from QRec. $KMnO_4$ and $NaNO_3$ were from Kemaus. H_2SO_4 was from Ajax FineChem.

2.2 Synthesis

2.2.1 Graphene Oxide (GO)

GO was synthesized from graphite powder by using modified Hummer's method. It related to both oxidation and exfoliation of graphite. The processed included: 1) Starting, 5 g of graphite powder and adding 2.5 of $NaNO_3$ into 1000 mL beaker in the container of ice cubes (temperature below 20℃) 2) Adding 200 mL of H_2SO_4 into the mixture and stirring for 1 hr. 3) Followed by slowly adding 30 g of $KMnO_4$ into the mixture and continuously stirring for another 2 hrs at temperature lower than 15°C. 4) Removing ice bath and continuously stirring for 2 hrs at room temperature 5) After that, slowly adding 100 mL of H_2O and heated to 90°C and kept stirring for 1 hr 6) Stirring for 1 hr with slowly additional of 100 mL of H_2O 7) Then, 30 mL of H_2O_2 was added to

stop reaction 8) Later, the final mixture was washed by centrifugation using 5% HCl and distilled water for several times until it formed gel like solution 9) The gel like solution was dried in oven for 24 hrs at 60°C to form GO powder.

2.2.2 Magnetic Graphene Oxide (MGO)

MGO adsorbent was synthesized by adding magnetic property from chemical with iron into the GO solution. The processes included: 1) Dispersing 0.3 g of GO in 150 mL of water by using sonication for 30 min 2) Mixing 0.8157 g of $FeCl_3 \cdot 6H_2O$ and 0.3 g of $FeCl_2 \cdot 4H_2O$ in 25 mL of water. 3) Dropping Fe^{3+} and Fe^{2+} solution to GO solution at room temperature with 200 rpm then dropping 30 mL of 28% ammonia to adjust pH to 10 and continuously stirring. 4) Increasing the temperature of the solution up to 80°C and stirring for 45 min to get the black color solution. Then, centrifuging the black solution to get the precipitation and washing with ethanol for several times 5) Drying process for 24 hrs. to get Fe_3O_4 - GO or Magnetic Graphene Oxide.

2.3 Adsorption experiment

In this study, batch experiments were used for adsorption experiments. The mixing conditions were setup with constant stirring at room temperature. 20 mL of water samples in different TDS concentrations (NaCl with DI water of 600 - 3000 mg/L) with pH 7 were prepared in 50 mL the glass tube. MGO of 10 - 40 mg was added. The tube was stirred at 300 rpm until reaching equilibrium. Later, MGO was separated from samples by using the magnetic bar as illustrated in **Figure 1.**

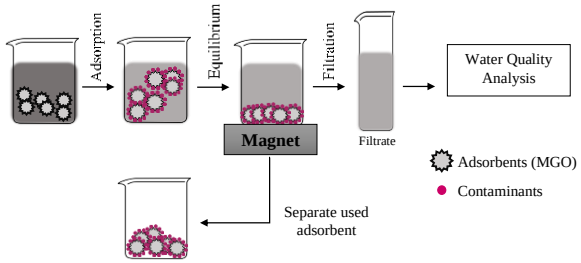

Figure 1. Diagram of batch experiment.

For adsorption isotherm, adsorption process is studied via graphs as adsorption isotherm, the amount of adsorbate (x) adsorbed on surface of adsorbent (m) at constant temperature. The basic equation of adsorption isotherm is Eq. 1. The removal percentage equation is shown in Eq. 2.

$$Q_t = \frac{(C_0 - C_t)}{m} V \quad (1)$$

Where Q_t is the amount of adsorbate per mass unit of adsorbent at time t (mg/g). C_0 is the initial concentration of adsorbate (mg/L). C_t is the residual concentration of adsorbate (mg/L). V is volume of the solution (L) and m is mass of adsorbent (g).

$$R\ (\%) = \frac{C_0 - C_t}{C_0} \times 100 \quad (2)$$

It is important to establish the most appropriate correlation for the equilibrium curves to optimize the adsorption processes.

2.3 Characterization

Phase components of GO and MGO were characterized by the X-ray diffraction (XRD; BRUKER model D2 phaser and the X-ray fluorescence analyzer (XRF; Olympus Vanta M Series Handheld analyzer).

Iris Binocular Zoom Stereo microscope model SZM45-B8L was used for characteristic outside of GO and MGO.

3. Results

The MGO is the one of the possible adsorbents for salinity or TDS removal in water. Many industrials normally used RO process for treating high TDS water. However, using the mechanical process and seasonal treatment may not suitable for setup. The application of MGO could be easier to do and the separation from treated water by using magnetic bar can be the advancement. Later, it can be regenerated for reuse as adsorbent again.

3.1 Characterization of GO and MGO

The XRD spectrum of GO and MGO are shown in **Figure 2.** with 2θ range from 5°-80°, increment is 0.02, voltage is 30 kV and Copper wavelength is 1.54184. The pattern of diffractogram presence diffraction peaks at 10.27° corresponding to (001) the XRD of GO[8,9] that report XRD of GO is around 10-13. The graphite was observed at peak of 25.55°, it means that some graphite remained after synthesized GO. However, the oxidation of graphite to GO is completed because XRD pattern indicated oxygen functional group.

Comparison between pattern of GO and MGO peaks are different. For MGO, in **Figure 3.** shows component in MGO which displayed a series of

diffraction peaks at 2θ = 30.33º, 35.52º, 42.75º, 52.82º, 56.11º, and 61.85º, corresponding to the reflections (220), (311), (400), (422), (511), and (440) crystal planes of the cube inverse spinel structure of Fe_3O_4. For Fe_2O_3 phase, XRD display diffraction peaks at 2θ = 24.12º, 33.86º, 36.25º, 40.85º, 49.36º, 53.96º 57.41º, 62.62º, and 63.85º, corresponding to the reflections (012), (104), (110), (113), (024), (116), (018), (214), and (300)[10].

XRF results of GO and MGO are summarized in **Table 1.** It shows quantity of Fe_2O_3 in GO and MGO. After synthesized graphite to GO, Fe in GO is less than 1% because GO was impurified magnetic property by HCl. For MGO, Fe is around 35% that prove MGO have Fe as the component or have magnetic property.

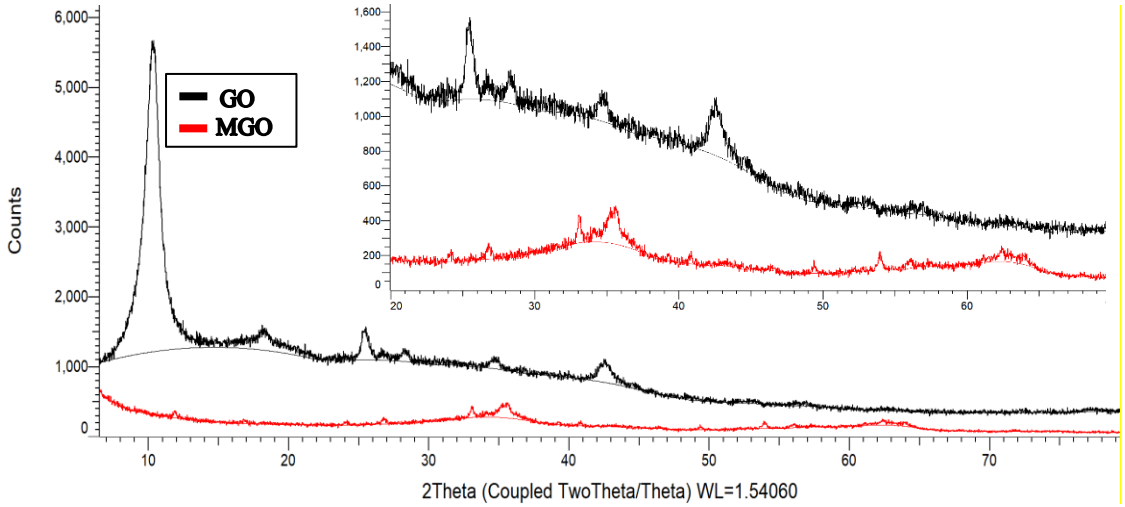

Figure 2 X-ray diffraction pattern compare between of GO and MGO nanocomposite.

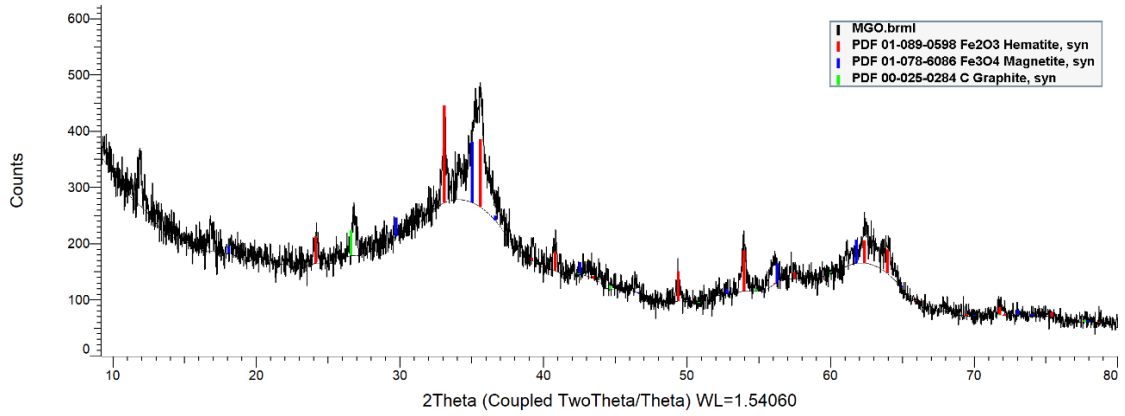

Figure 3 XRD pattern obtained for MGO

Table 1 XRF results of GO and MGO

	GO		MGO	
	ppm	%	ppm	%
Fe	2346	<1	356607	35.66
	2388	<1	366988	36.70
	2406	<1	347497	34.75
	2380	<1	357030	35.70
Avg	**2380**	**<1**	**357030**	**35.70**

The characteristic outside of GO and MGO are determined by stereo microscope and present in **Figure 4.** Comparison between GO and MGO, GO powder is dark brown and surface is quite rugged. For MGO powder, particle is black and slicker than GO. Moreover, MGO powder has light orange particle that is Fe_2O_3 and Fe_3O_4.

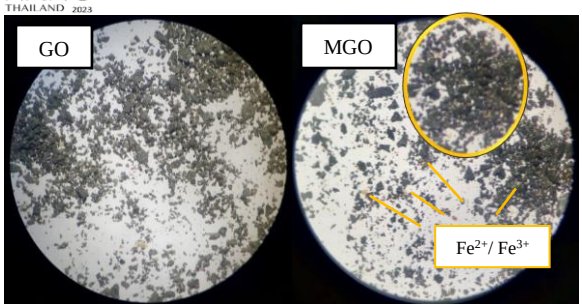

Figure 4. Stereo microscope images of GO and MGO

3.2 Effect of MGO doses and contact times

In this study, adsorbent dosages were tested at 10, 20, 30 and 40 mg of MGO with initial TDS concentration of 1800 mg/L at pH 7. The experiments were conducted at the room temperature with the contact time of 5 – 30 mins. There were 3 replicates for each test. Results between percent removals and times are plot as shown in graphs in **Figure 5.** The percentage removals were increased and reached equilibrium at about 10 mins in every conditions. The highest percentage removal of 66.94% was occurred with the MGO of 40 mg. It is found that increasing of MGO dosages could increase the percent removal[11,12] This is probably due to the increasing of surface area of MGO and having availability more unoccupied surface to adsorb NaCl in water.

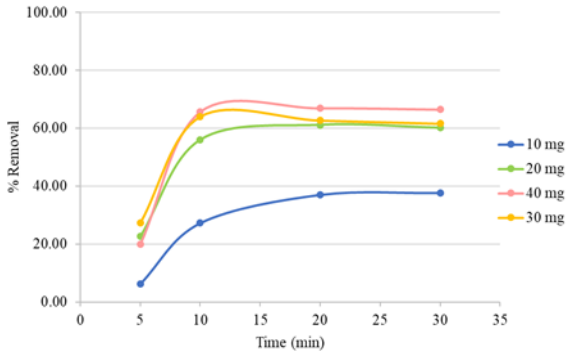

Figure 5. Removal Percentage in various MGO dosage at TDS initial concentration 1800 mg/L.

However, the percent removal, 64%, of NaCl in MGO of 30 mg test did not different to the MGO of 40 mg test, because surface of MGO is covered with adsorbate. The adsorption capacity remains almost stable because no more sodium ions can be added to surface of MGO[13].Therefore, the 30 mg of MGO was selected as suitable adsorbent for next experiments.

3.3 Effect of TDS initial concentration

The water samples were prepared as initial TDS concentrations in the range between 600 mg/L to 3000 mg/L. The experiments were tested at pH 7 with the doses of MGO of 20 and 30 mg. The contact times for adsorption were between 5 to 20 mins. The results are reported as percent removal and time as shown in **Figure 6.** The percent removals were increased when increasing contact times. These were similar results to the previous studies. However, the equilibrium was reached at 10 mins in each experiment. It can be explained that the capacity of surface area of MGO can be saturated after 10 min. It causes no vacant area to adsorb NaCl.[14] It is remarkable that the percent removal of NaCl of 600 mg/L is higher than 80%.

Likewise, increasing dose of MGO from 20 to 30 mg could increase the percent removals from 60.3% to 85.3% at initial concentration of 600 with 10 mins contact time.

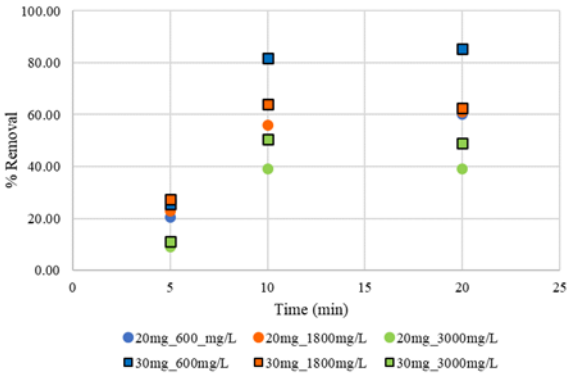

Figure 6. Percent removals of NaCl at various MGO dosages and initial TDS concentrations.

Moreover, **Figure 6** shows percent removals according to varied initial concentrations ranging from 600, 1800 and 3000 mg/L. It was found that at contact time of 20 min with using MGO of 30 mg, increasing NaCl concentrations the percent removals were decreased from 85.3% to 49% at TDS initial concentrations of 600 mg/L to 3000 mg/L, respectively. Therefore, increasing of initial concentration with constant dose of MGO can decrease the percent removals. It is because of MGO surface is full with NaCl then the residue is remained.[11] At the higher initial concentration, the low ratio of NaCl molecule to the available surface area of MGO gave the decreasing of adsorption capacity.[12]. Furthermore, this result could also be attributed to the increased driving force of the concentration gradient, as the rising NaCl

concentration accelerates the diffusion of molecules onto the adsorbent[11].

Moreover, the comparison between doses of MGO and initial concentrations are illustrated in the **Figure 7.**

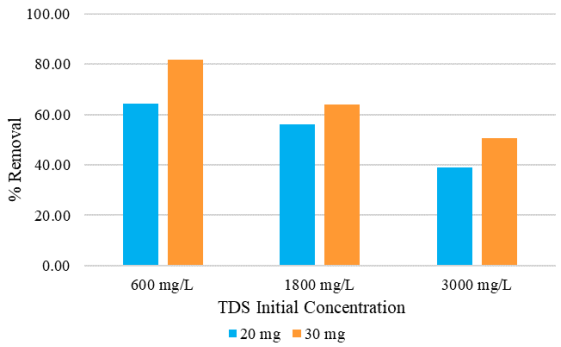

Figure 7. Effect of MGO dosage with TDS initial concentration (pH = 7 and contact time = 10 min).

Figure 7 also informed that, high number of doses gave the higher percent removal in every initial concentration. Considering the effective parameters for adsorption, Q_t values were calculated and presented in **Figure 8.**

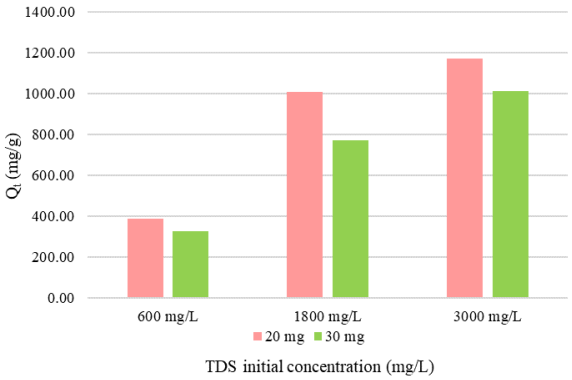

Figure 8. Adsorption capacity in various MGO dosage and TDS initial concentration (pH 7 and contact time = 10 mins).

Dosage of 20 mg gave high number of Q_t of 385, 1008 and 1172 mg/ g at the concentration of NaCl of 600,1800 and 3000 mg/l, respectively. This could be informed that the maximum adsorption rate was 1172 mg/g. Then, the selected optimum dose was 20 mg of absorbent per 20 ml of adsorbate with 10 mins contact time.[12]

3.4 Settling time

After adsorption experiment, MGO was separated from water samples as illustrated in **Figure 9**. It can be observed that the settling times were 15 sec. and 3 mins when using magnetic bar. All of MGO particles was settled down to the bottom of the tube which could be easily separated from water samples.

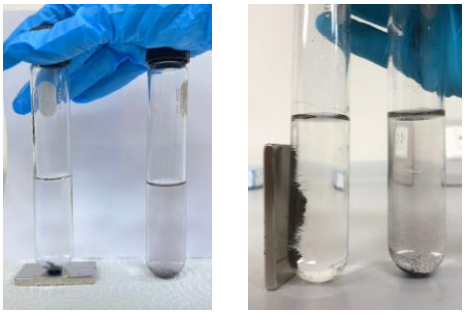

Figure 9. Settling experiments of MGO with and without using magnet

On the other hand, the settling time was more than 20 mins in case not using magnet for separation. MGO particles still diffused in the tube and slowly settled down to the bottom. This property could be the benefit for the sedimentation process in terms of short detention time and small tank of sedimentation.[15]

Conclusion

Nowadays, graphene applications are using for water purification. Magnetic property of MGO is also very useful for the settlement process. Particles can be separated faster with the MGO and the magnet application. It is revealed that the percent removal for the initial TDS concentration 1800 mg/L was up to 70% using MGO of 20 mg with 10 mins (At equilibrium). The settling time of MGO particles with using the magnet was about 3 mins and faster than not using magnet. MGO could the promising absorbent for the TDS removal in the salinity water. However, how to lower the cost of MGO synthesis is needed for further study.

Acknowledgements

This work was financially supported by Graduate Studies of Mahidol University Alumni Association and Graduate Studies of Mahidol University.

References

1. Anurak, W., 2017. What is R.O. (Reverse Omosis), 2018. O.K. filter. https://www.ok-filter.com/article/2-r-o-reverse-osmosis (accessed 2020-07-23).
2. World Health Organization (WHO), Guidelines for drinking-water quality. *A global overview of national regulations and standards for drinking-water quality*, 4th ed.; 2018.
3. Centers for Disease Control and Prevention., 2015. Drinking Water Treatment. Disease Control and Prevention. https://www.cdc.gov/healthywater/drinking/public/water_treatment.html
4. Napat, L.; Natpichan, P.; Kittapas, C.; Thirawit, S.; Prowpatchara, C.; Panpailin, S.; Pattaraporn, K.L.; Sira, S., One-Step Hydrothermal Synthesis of Precious Metal-Dope Titanium Dioxide−Graphene Oxide Composites for Photocatalytic Conversion of CO2 to Ethanol. *ACS Omega*. **2021**, *6*, 35769−35779.
5. Ya, P.; Yaoyu, Z.; Kun, L.; Zhu, Z.; Ran, Y.; Xue, L.; Min, L., Activation of persulfate by stability-enhanced magnetic graphene oxide for the removal of 2,4-dichlophenol. *Science of the Total Environment*. **2020**, *707*, 135656.
6. Dan, H.; Baile, X.; Jizi, W.; Philip, C.; Jianming, X., Adsorption and desorption of phenanthrene by magnetic graphene nanomaterials from water: Roles of pH, heavy metal ions and natural organic matter. *Chemical Engineering Journal*. **2019**, *368*, 390-399.
7. Hidayati, N.; Hashimah, N.; Zaman, M.; Fitrah, N.; Raikhan, N.; Jye, W., 4 Adsorption kinetics of methylene blue dyes onto magnetic graphene oxide. *Journal of Engineering Chemical Engineering*. **2018**, *6*, 2803-2811.
8. Mudita, N.; Rita, K., Facile synthesis of mesoporous magnesiumoxide–graphene oxide composite for efficient and highlyselective adsorption of hazardous anionic dyes. *Spring Nature*. **2020**, *46*, 2497-2521.
9. Prashant, M.K.; Avinash, R.K.; Nandkumar, T.M.; Sachin, R.R.; Sandesh, R.J.; Shivaji, V.B., Graphene Oxide Assisted Synthesis of Magnesium Oxide Nanorods. *ES Materials and Manufacturing*. **2021**, *12*, 63-71.
10. Suresh, S.; Karthikeyan, S.; Jayamoorthy, K., Effect of bulk and nano-Fe_2O_3 particles on peanut plant leaves studied by Fourier transform infrared spectral studies. *Journal of Advanced Research*. **2016**, *7*, 739-747.
11. Othman, N.H.; Alias, N.H.; Shahruddin, M.Z.; Baker, N.F.A.; Him, N.R.N.; Lau, W.J., Adsorption kinetics of methylene blue dyes onto magnetic graphene oxide. *Journal of Environment Chemical Engineering*. **2018**, *6*, 2803-2811.
12. Bharath, G.; Emad, A.; Ponpandian, N.; Moonis, K.; Masoon, S.; Faheem, A.; Edreese, H., Development of adsorption and electrosorption techniques for removal of organic and inorganic pollutions from wastewater using novel magnetite/porous graphene-based nanocomposites. *Separation and Purification Technology*. **2017**, *188*, 206-218.
13. Wondimu, M.; Girma, G., Adsorption of sodium from saline water with natural and acid activated Ethiopian bentonite. *Result in Engineering*. **2022**, *14*, 100440.
14. Zeinab, F.A.; Elsayed, G.Z.; Shimaa, M.E., Green Hydrogel-Biochar Composite for Enhanced Adsorption of Uranium. *ACS OMEGA*. **2021**, *6*, 34193-34205.
15. Bin, Y.; Yihua, W.; Qinglan, L.; Yang, L.; Suyan, Q.; Zeming, S., Polyvinylpyrrolidone functionalized magnetic graphene - based composites for highly efficient removal of lead from wastewater. *Colloids and Surface A*. **2019**, *582*, 123927.

Study of perovskite Mn_3O_4/$NiMnO_3$ nanomaterial for supercapacitor applications

Thitirat Kansaard[1], Thareerat Singha[1], Surangkana Wannapop[1], Asanee Somdee[1]*
[1]*Faculty of science, Energy, and Environment, King Mongkut's University of Technology North Bangkok, Rayong Campus, Rayong 21120, Thailand.*
**E-mail: asanee.s@sciee.kmutnb.ac.th*

Abstract:

In this research, pure $NiMnO_3$ and Mn_3O_4/$NiMnO_3$ nanostructures have been synthesized by hydrothermal method and then fabricated as supercapacitors. All materials were characterized by X-ray diffraction, scanning electron microscopy, and Transmission electron microscopy. All electrochemical performances of these nanostructures were investigated by Cyclic Voltammetry, Galvanostatic Charge-Discharge, and Electrochemical Impedance Spectroscopy. Results showed that the $NiMnO_3$ (NMO) has a specific capacitance of 262.15 Fg^{-1}. In comparison, the highest enhancement by Mn_3O_4 to the $NiMnO_3$ is 574.85 Fg^{-1} at the scan rate of 5 mVs^{-1}. In our preliminary study, the $NiMnO_3$ (NMO) and enhanced Mn_3O_4/$NiMnO_3$ (M-NMO) electrodes have studied in 1 M KOH electrolyte.

Keywords: Supercapacitor, Perovskite, $NiMnO_3$, nanomaterials, Energy storage

Figure 1. Schematic diagram shows the NMO and M-NMO synthesis.

1. Introduction

Searching for renewable energy resources with less effect on the environment has become an interesting topic of research today. Using the fossils has caused warming.[1] Up to date, there are many renewable soruces, such as solar energy, wind, biomass, etc.[2], that have been compensated for the burning of fossil. On the other hand, some technologies, such as solar energy, can store photons in electrical energy with high demand, which requires an energy storage system in some cases.

The most well know energy system of energy storage system is the battery. However, the resources to fabricate the battery, e.g., Lithium ion battery[3], require an expensive raw material and is difficult to handle with the lithium source. On the other hand, the electrical double layer supercapacitor is one of the promising candidates for an energy storage device instead of a battery. Comparing between a battery and a supercapacitor, the advantage of a battery over a supercapacitor is the energy density. However, the supercapacitor has more benefits than the battery in the power density.[4]

Recently, various perovskite oxide materials, which formula ABO_3[5], such as $NiMnO_3$[6,7,8,9], $BiFeO_3$[10], $NiTiO_3$[11], $SrTiO_3$[12] and etc., have been applied as the supercapacitor.

In this work, The $NiMnO_3$ (NMO) and Mn_3O_4/$NiMnO_3$ (M-NMO) nanostructures were explored. The materials were synthesized by the hydrothermal method and then were characterized by various techniques, as follows. The crystal

structures of the material were investigated by X-ray diffraction (XRD). Surface morphology was studied using scanning electron microscopy (SEM) and transmitted electron microscopy (TEM). Finally, the electrochemical properties of supercapacitors of these materials were explored by the potentiostat with various techniques. The CyclicVotrammetry (CV) and Galvanostatic charging and discharging (GCD) were studied to estimate the specific capacitance of the materials. The electrochemical impedance (EIS) was used to investigate the internal resistance of the material.

2. Materials and Methods

2.1 Materials

Analytical grade chemicals, such as Nickel(II) acetate hydrate ($Ni(CH_3COO)_2{\cdot}xH_2O$, 99%, Alfa Aesar), Manganese(II) acetate tetrahydrate ($(CH_3COO)_2Mn{\cdot}4H_2O$, 99%, VR Bioscience), potassium hydroxide (KOH), sodium hydroxide (NaOH)

2.2 Synthesis

$NiMnO_3$ (NMO) was synthesized by the hydrothermal method. In brief, 5 mmol of $Ni(CH_3COO_2{\cdot}H_2O)$ and 5 mmol of $Mn(CH_3COO)_2{\cdot}4H_2O$ were dissolved in deionized water (DI) 60 mL. The mixed Ni and Mn sources were stirred until the clear solution was obtained. Then, 3 M NaOH solution was added. The brown sediment has been obtained. The mixed precursor was transferred to the hydrothermal reactors and autoclaved at 160 °C for 10 hours. After the reaction was finished, the products were collected by the filter and washed by DI several times. Finally, the product was calcined at 550 °C for 2 hours in an air atmosphere.

The nanocomposites of Mn_3O_4/NMO (M-NMO) have been synthesized similarly to the previous NMO synthesis. However, the ratio of Ni and Mn ions was different. In this work, the ratio between Ni : Mn ions were 1:1, 1:1.5, 1:2 and 1:2.5.

2.3 Characterization

X-ray diffraction pattern (XRD) of the M-NMO was performed. The morphology of the samples was analyzed through scanning electron microscopy (SEM) and transmitted electron microscopy (TEM).

2.4 Electrode fabrication for electrochemical study

The NMO and M-NMO gel has been coated on the nickel foam electrode where the gel was composed of raw supercapacitor material, carbon black, and Polyvinylidene fluoride (PVDF) 8:1:1 ratio where the N-Methyl-2-pyrrolidone (NMP) was a solvent as a mixing agent. The NMO and M-NMO gels were coated in the nickel form, and the coating area was fixed to approximately 1 cm^2. Then, the electrode was dried by vacuum oven at 60 °C for 24 hours.

Electrochemical properties of NMO and M-NMO electrodes were characterized by using 3 electrodes method. The materials electrodes were set as a working electrode, Pt wire was set as the reference electrode, and the Ag/AgCl was used as a reference electrode. All electrochemical properties were determined using 1 M KOH as an electrolyte. The CV, GCD, and EIS have been studied by Potentiostat (Zahner Zennium pro).

3. Results

3.1 Characterization.

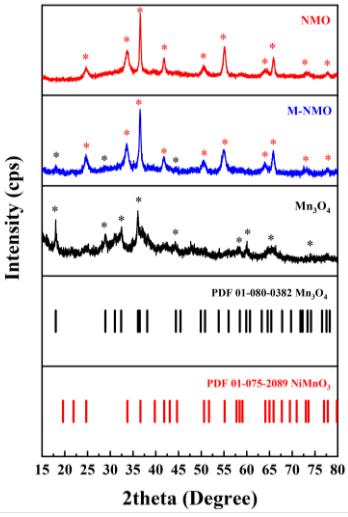

Figure 2. XRD patterns of NMO, M-NMO, and Mn_3O_4

Figure 2. shows the X-ray diffraction of NMO, M-NMO, and Mn_3O_4 nanomaterials. In the first graph, the diffraction peaks found at 24.7°, 33.8°, 36.6°, 41.8°, 50.6°, 55.1°, 64.1°, 65.9°, 73°

and 77.8° were matched well to the $NiMnO_3$ (NMO) crystallographic database (PDF: 01-075-2089) where were corresponding to (012), (104), (110), (11-3), (024), (11-6), (12-4), (300), (1010), and (220) Miller indices plane, respectively. In the second graph, the immerged peaks located at 18°, 28.9°, and 44.4° were assigned to the Mn_3O_4 phase (PDF: 01-080-0382). This result of the mixing phase is evidence of the successful synthesis of M-NMO nanocomposite. In addition, pure Mn3O4 was synthesized for the purpose of comparing capacitance with NMO and M-NMO.

Figure 3. shows the SEM images of Mn_3O_4 and M-NMO nanocomposite materials. Comparing the pure and the composite phases, the morphology of these two materials was similar. One noticeable feature in Figure 3b is that a rough surface was observed. We expected that the Mn_3O_4 should be located at the surface of NMO. Therefore, the result of M-NMO was, in addition, investigated by TEM.

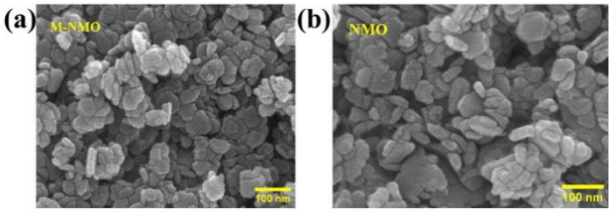

Figure 3. SEM image of (a) M-NMO and (b) NMO nanomaterials.

Figure 4. shows the TEM image of the M-NMO nanocomposite. Figure 4a. shows the sample overview, and Figure 4b. shows the high-resolution TEM images. In Figure 4b, it was found that there are two phases, which belong to the NMO and Mn_3O_4 phases. The d-spacing of 0.27 and 0.25 nm were assigned to the (104) and (110) planes of NMO. In addition, the d-spacing of 0.5 nm was found and was assigned to the (101) plane of Mn_3O_4. This presence of both d-spacing of NMO and Mn3O4 was supported by the XRD results that the Mn_3O_4 was well formed on the NMO surface.

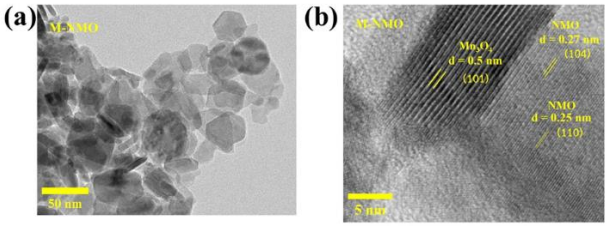

Figure 4. TEM images of (a) overview and (b) high-resolution of M-NMO nanocomposite.

3.2 Supercapacitor performance

Figure 5. shows the CV of pure Mn_3O_4, M-NMO, and pure NMO electrodes and comparative CV plots of these electrodes at scan rate 5 mVs^{-1}. As a result, the electrochemical study of M-NMO nanocomposite showed the most outstanding performance on CV. When comparing M-NMO to others, the area of the CV of M-NMO is larger than that of others, Mn_3O_4 or pure NMO. This work summarizes the specific capacitance of pure Mn_3O_4, M-NMO, and pure NMO electrodes in **Table 1**.

Table 1. Summarization of specific capacitance of NMO, M-NMO, and Mn_3O_4 at scan rate 5 mVs^{-1}

Electrode materials	Capacitance (Fg^{-1})
M-NMO (1:2)	574.85
M-NMO (1:1.5)	220.60
M-NMO (1:2.5)	277.25
NMO	262.15
Mn_3O_4	192.59

As shown in **Table 1**, the highest specific capacitance was M-NMO (1:2), which was 574.85 Fg^{-1}. Compared to the Mn_3O_4, the specific capacitance values of all nanocomposites were more significant than the pure materials. It was noticeable that mixing more Mn_3O_4 to the NMO decreased the specific capacitance.

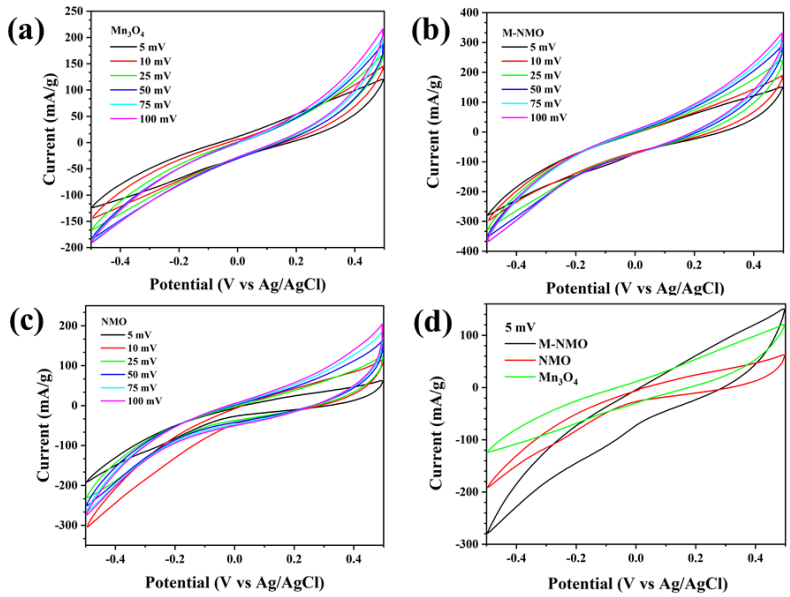

Figure 5. Cyclic Voltammetry (CV) of (a) pure Mn_3O_4, (b) M-NMO, (c) pure NMO electrodes, and (d) Comparative CV plots of the pure Mn_3O_4, M-NMO, and pure NMO electrodes at scan rate 5 mVs^{-1}

Figure 6. shows the GCD of Mn_3O_4, M-NMO, and NMO electrodes. For the case of Mn_3O_4, the total time of charging and discharge at 5 mAg^{-1} was about 37 s, while the NMO was 46 s. The mixing of Mn_3O_4 and NMO showed better charge storage than the sole materials. In the case of M-NMO (1:2), the total time of charging and discharge at 5 mAg^{-1} was about 170 s, which is much more than the 4-5 times of pure NMO and Mn_3O_4 materials. Figure 6d. compared all electrodes at charging and discharging of 5 mAg^{-1}, which clearly showed the improvement of Mn_3O_4 on the NMO supercapacitors.

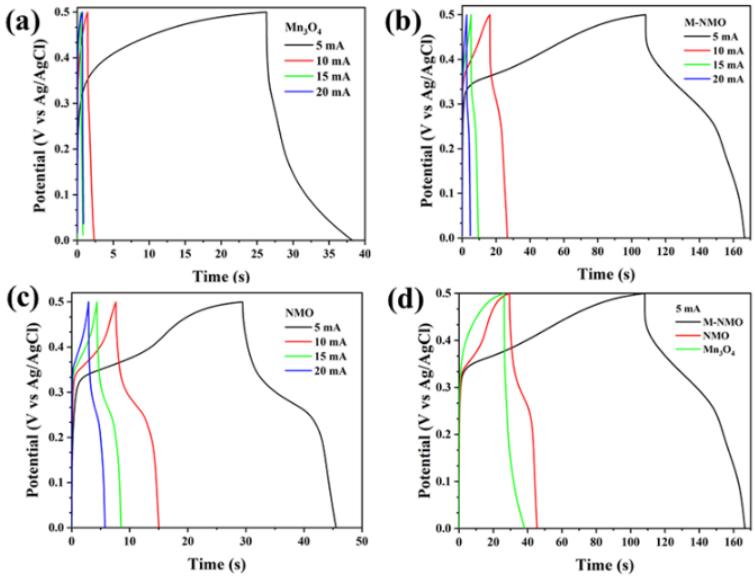

Figure 6. Galvanostatic charging and discharging (GCD) of (a) Mn_3O_4, (b) M-NMO, (c) NMO at current density 5, 10, 15, and 20 mAg^{-1}, and (d) Comparative GCD plots of the 3 working electrode at current density 5 mAg^{-1}.

Conclusion

This work explored the NMO, perovskite nanomaterials for application as supercapacitor electrode materials. The specific capacitance of NMO was 262.15 Fg^{-1} at a scan rate of 5 mVs^{-1}. After being enhanced by Mn_3O_4 (M-NMO), the specific capacitance was 574.85 Fg-1 at 1:2 Ni:Mn ratio of precursor. Our preliminary research will continue to study the effect of Mn_3O_4 to influence the improvement of NMO-based materials.

Acknowledgements

This research was funded by King Mongkut's University of Technology North Bangkok, Contract no. KMUTNB-67-KNOW-20.

References

1. Noah, S. D.; Marshall, B., Global warming has increased global economic inequality. *PNAS*. **2019**, 116, *20*, 9808–9813.
2. Patrick, M.; Damon, H., What is the global potential for renewable energy. *Renewable and Sustainable Energy Reviews*. **2012**, *16*, 244–252.
3. Elham, K. H.; Ata, K.; Mahmoud, H. S.; Abolghasem, A., Electrode Materials for Lithium Ion Batteries: A Review. *Journal of Ultrafine Grained and Nanostructured Materials*. **2018**, *51*, 1, 1-12.
4. Zaharaddeen, S. I.; Subramani, C.; Dash, S.S., A Brief Review on Electrode Materials for Supercapacitor. *Int. J. Electrochem. Sci.* **2016**, *11*, 10628 – 10643.
5. Yang, C.; Jie, L.; Xue, L.; Luchao, Y.; Qian, L.; Siyu, L.; Abdullah, M. A.; Jianming, H.; Yonglan, L.; Xuping, S., Recent advances in perovskite oxides as electrode materials for supercapacitors. *Chem. Commun.* **2021**, *57*, 2343-2355.
6. Ya, C.; LiTao, C.; Pinf, L.; JieHao, G.; Yong, L., Preparation and electrochemical properties of $NiMnO_3$@NiO nanosheets for pseudocapacitors. *Journal of Alloys and Compounds*. **2020**, *832*, 154936.
7. Dhas, S.D.; Maldar, P.S.; Patil, M.D.; Hubali, K.M.; Shembade, U.V.; Abitkar, S.B.; Waikar, M.R.; Sonkawade, R.G.; Agawane, G.L.; Moholkar, A.V., Hydrothermal synthesis of mesoporous $NiMnO_3$ nanostructures for supercapacitor application: Effect of electrolyte. *Journal of Energy Storage*. **2021**, *35*, 102277.
8. Hyo-Young, K.; Jeeyoung, S.; Il-Chan, J.; Young-Wan, J., Hydrothermal Synthesis of Three-Dimensional Perovskite $NiMnO_3$ Oxide and Application in Supercapacitor Electrode. *Energies*. **2020**, *13*, 36, 1-11.
9. Shaoming, Q.; Naibao, H.; Yin, S.; Junjie, Z.; Yuanyuan, Z.; Zhengyuan, G., Microwave-assisted synthesis of novel 3D flower-like $NiMnO_3$ nanoballs as electrode material for high-performance supercapacitors. *Journal of Alloys and Compounds*. **2019**, *775*, 1109-1116.
10. Arpan, K. N.; Thamizharasan, G., Phase- and Crystal Structure-Controlled Synthesis of Bi_2O_3, Fe_2O_3, and $BiFeO_3$ Nanomaterials for Energy Storage Devices. *ACS Appl. Nano Mater.* **2022**, *5*, 14663-14676.
11. Debabrata, N.; Harikrishnan, P.; Sabarish, R.; Aswathy, J.; Nuntawat, K.; Suchart, S., Solvothermal synthesis of nickel titanate nanosphere: crystal structure determination and high-rate supercapacitor performance. *Chemical Papers*. **2023**, *77*, 385–397.
12. Prabodh, C. P.; Shah, A.; Singh, L. R.; Mrityunjoy, M.; Dev, K. M., Mn-Doped $SrTiO_3$ and $SrTiO_3$-Fe_2O_3 Composite Perovskites: Photocatalytic Dye Degradation and Supercapacitor Application. *SSRN*. **2023**, 1–20.